POLYPUBLIE
Polytechnique Montréal

POLYTECHNIQUE MONTRÉAL
UNIVERSITÉ D'INGÉNIERIE

Titre: Title:	Neonatal Resting-State Functional Magnetic Resonance Imaging: Optimization of Data Acquisition and Democratization of Data Preprocessing
Auteur: Author:	Vicente Enguix Chiral
Date:	2022
Type:	Mémoire ou thèse / Dissertation or Thesis
Référence: Citation:	Enguix Chiral, V. (2022). Neonatal Resting-State Functional Magnetic Resonance Imaging: Optimization of Data Acquisition and Democratization of Data Preprocessing [Thèse de doctorat, Polytechnique Montréal]. PolyPublie. https://publications.polymtl.ca/10716/

Document en libre accès dans PolyPublie
Open Access document in PolyPublie

URL de PolyPublie: PolyPublie URL:	https://publications.polymtl.ca/10716/
Directeurs de recherche: Advisors:	Julien Cohen-Adad, & Gregory Lodygensky
Programme: Program:	Génie biomédical

Ce fichier a été téléchargé à partir de PolyPublie, le dépôt institutionnel de Polytechnique Montréal
This file has been downloaded from PolyPublie, the institutional repository of Polytechnique Montréal

https://publications.polymtl.ca

POLYTECHNIQUE MONTRÉAL

affiliée à l'Université de Montréal

Neonatal resting-state functional magnetic resonance imaging: optimization of data acquisition and democratization of data preprocessing

VICENTE ENGUIX CHIRAL

Institut de génie biomédical

Thèse présentée en vue de l'obtention du diplôme de *Philosophiae Doctor*

Génie biomédical

Décembre 2022

© Vicente Enguix Chiral, 2022.

POLYTECHNIQUE MONTRÉAL

affiliée à l'Université de Montréal

Cette thèse intitulée :

Neonatal resting-state functional magnetic resonance imaging: optimization of data acquisition and democratization of data preprocessing

présentée par **Vicente ENGUIX CHIRAL**
en vue de l'obtention du diplôme de *Philosophiae Doctor*
a été dûment acceptée par le jury d'examen constitué de :

Frédéric LESAGE, président
Julien COHEN-ADAD, membre et directeur de recherche
Gregory LODYGENSKY, membre et codirecteur de recherche
Benjamin DE LEENER, membre
Alexander G. WEIL, membre externe

DEDICATION

To Rosario.

ACKNOWLEDGEMENTS

I want to thank everyone who helped me and contributed to making this project possible. To Frédéric Lesage, Benjamin de Leener, and Alexander Weil for accepting to be a part of my thesis committee. To Julien Cohen-Adad, my supervisor and a researcher I admire, for being there in the critical moments. To Gregory Lodygensky, my co-supervisor, for sharing his love for science and medicine with me and letting me work in his lab at the CHU Sainte-Justine.

To Christopher Smyser, Jeffrey Neil, and Jeanette Kenley, from the Washington University School of Medicine in Saint Louis. They are a world-leading lab in the field and I'm grateful for their collaboration and valuable feedback about my pipeline.

To my colleagues from the CHU Sainte-Justine. Irene Londoño, for our great discussions. David Luck, for his help with manuscripts and sense of humor. To Yang Ding, for the sushi and motivation. To Farzad, Erjun, Wyston, Prabhas, Tiffany, Nadine, Vitor, Angela, Julie, Alexandre and Michele for making the days feel shorter.

I gratefully acknowledge the Quebec Bio-imaging Network for providing me with financial support and for their confidence in my project.

To my figure skating and road cycling friends, especially Steve, for making it easier these years.

I want to express my immense gratitude to my sister and parents, who have always supported and encouraged me to pursue my dream of doing a PhD. Finally, I would like to thank my lovely wife, Sara, who crossed the ocean to live this journey together.

RÉSUMÉ

L'extrême prématurité et les cardiopathies congénitales sont associées à un risque élevé de lésions cérébrales induisant des troubles neurocognitifs sévères. Jusqu'à récemment, l'examen de ces lésions reposait sur des techniques neuroanatomiques, offrant peu d'informations quant à leurs conséquences sur le plan fonctionnel. En ce sens, l'analyse des réseaux neuronaux en état de repos par IRM fonctionnelle constitue une approche prometteuse pour mieux comprendre l'effet de ces lésions. De plus ils commencent à apparaître dès le troisième trimestre de gestation, avec de fortes perturbations lors d'une naissance prématurée. Sur le plan clinique, l'impact des atteintes cérébrales sur les différents réseaux en état de repos, offrirait des avancées en termes de pronostic puisque ces atteintes, quoique présentes dans les premiers mois de vie, n'ont une expression clinique que plusieurs années après la naissance. Malgré les possibilités offertes par IRM fonctionnel en état de repos, son application pose divers défis méthodologiques. La qualité des images peut être altérée par le mouvement de la tête, pouvant conduire à des données inutilisables, et que l'on découvre à posteriori pendant les étapes de traitement d'images, car une inspection visuelle des données est impossible due au grand volume de données acquises. De plus, le traitement des données RS néonatales est très complexe. Des outils permettant le preprocessing des données existent chez l'adulte, mais ceci est difficilement applicable au nouveau-né à cause de l'inversion du contraste matière blanche/grise dû au processus de myélinisation ou de la constante croissance.

Pour pallier à ces limitations, il est nécessaire d'acquérir des images d'excellente qualité ainsi que le développement d'outils adaptés aux besoins des images des nouveau-nés. Car, pour réussir le pretraitement des données IRM fonctionnel en état de repos néonatales, chaque bébé doit être traité de façon individuelle et avec beaucoup d'attention. Ce projet porte donc sur le développement d'un protocole optimisé pour le nouveau-né ainsi que l'évaluation du mouvement de la tête en temps réel (pendant que le bébé est encore dans l'IRM) afin de décider si les données acquises passent les critères de qualité ou si des données additionnelles doivent être collectées avant de sortir le bébé de l'IRM. Ceci permet d'acquérir des données de qualité, réduisant ainsi le nombre de sujets rejetés dans une étude. Enfin, afin de permettre aux différents centres de traiter leurs données de façon rapide et efficace, nous avons développé un outil open-source appelé NeoRS, permettant le

pretraitement individuel des données néonatales. NeoRS répond aux spécificités du pretraitement des images néonatales en accordant une attention particulière au recalage, y compris à l'atlas néonatal, ainsi qu'aux paramètres tels que les différences de contraste dues à la myélinisation et de taille de la tête. Nous espérons que NeoRS permettra à un plus grand nombre de centres de pretraiter leurs ensembles de données, contribuant ainsi à produire un plus grand nombre d'études. Cela permettra, à terme, de développer des applications pour l'utilisation des réseaux en état de repos comme biomarqueur de l'intégrité cérébrale.

ABSTRACT

Extreme prematurity and congenital heart disease are associated with a high risk of brain damage leading to severe neurocognitive disorders. Until recently, these lesions were examined based on neuroanatomical techniques, offering little information about their functional consequences. In this sense, the resting-state networks analysis by functional MRI is a promising approach to better understanding these lesions' effects. Moreover, they appear as early as the third trimester of gestation, with strong disruptions during a premature birth. From a clinical point of view, the impact of brain damage on the different resting-state networks could help prognosticate the impact of the injury since this damage, although present during the first months of life, does not have a clinical expression until several years after birth. Despite the possibilities offered by resting-state functional MRI, its application poses various methodological challenges. For example, the head movement can alter the image quality, leading to unusable data, usually discovered afterward during the image preprocessing steps. Indeed, visual inspection of the data is impossible due to the large volume of acquired data. Moreover, the preprocessing of neonatal resting-state data is very complex. Image preprocessing tools exist for adults, but this is difficult to apply to neonates because of the inversion of the white matter/gray contrast due to the myelination process or the constant growth.

To overcome these limitations, it is necessary to acquire excellent quality images and develop tools adapted to the needs of newborn data. To do so, each baby must be considered individually and with great care. Therefore, this project focuses on developing a protocol optimized for neonates and the evaluation of the head movement in real-time (while the baby is still in the MRI) to decide if the acquired data passes the quality criteria or if additional data has to be collected before the baby leaves the MRI room. This enables the acquisition of high-quality data with low motion, decreasing the number of discarded subjects in a study. Finally, we developed an open-source tool called NeoRS for neonatal data to allow the different centers to preprocess their data quickly and efficiently. NeoRS addresses the specificities of neonatal image preprocessing by paying particular attention to image registration, including neonatal atlas and parameters like differences in contrast due to myelination and different head sizes. We hope NeoRS will allow more centers to preprocess

their datasets, contributing to producing a higher number of studies. Ultimately, this will enable the development of applications for using resting-state networks as a biomarker of brain integrity.

TABLE OF CONTENTS

DEDICATION III

ACKNOWLEDGEMENTS IV

RÉSUMÉ V

ABSTRACT VII

TABLE OF CONTENTS IX

LIST OF TABLES XIV

LIST OF FIGURES XV

LIST OF SYMBOLS AND ABBREVIATIONS XVIII

LIST OF APPENDICES XX

CHAPTER 1 INTRODUCTION 1

CHAPTER 2 LITERATURE REVIEW 3

2.1 Functional neuroimaging techniques 3

2.1.1 Functional positron emission tomography 3

2.1.2 Functional MRI 4

2.1.3 Electroencephalography 5

2.1.4 Magnetoencephalography 5

2.1.5 Functional Near Infrared Spectroscopy 6

2.1.6 Final comparisons 6

2.2 MRI Basic principles 7

2.2.1 T1, T2 and T2* relaxation times 9

2.2.2 TE, TR and tissue contrast 10

2.2.3 Pulse sequences 10

2.3 Resting-state fMRI 12

2.3.1 Blood-Oxygen-Level-Dependent signal 12
2.3.2 EPI contrast 13
2.3.3 GRE-EPI artifacts 14
2.3.4 Multi-band EPI 15
2.3.5 Multi-echo rs-fMRI 16
2.3.6 Functional connectivity and resting-state networks 17
2.3.7 Related works 18
2.3.8 Clinical neonatal rs-fMRI 18
2.3.9 Challenges on neonates 19
2.4 Image preprocessing 21
2.4.1 Conn toolbox 22
2.4.2 FMRIPrep 23
2.4.3 Human Connectome Project Pipeline 23
2.4.4 Developing Human Connectome Project Pipeline 23
2.5 Data analysis 24
2.5.1 Seed-based correlations 24
2.5.2 Independent Components Analysis 25
2.5.3 Graph theory 25
2.5.4 Measures of correlation 27
CHAPTER 3 PROJECT ORGANIZATION 34
3.1 Objectives and impact of the contributions 34
3.2 Thesis overview 35
CHAPTER 4 ARTICLE 1: ALTERED RESTING STATE FUNCTIONAL CONNECTIVITY IN YOUTH WITH CONGENITAL HEART DISEASE OPERATED DURING INFANCY 36
4.1 Abstract 37

4.2 Introduction 37
4.3 Materials and methods 39
4.3.1 Participants 39
4.3.2 Individual and clinical variables 40
4.3.3 Executive function and self-regulation 40
4.3.4 MRI data acquisition 40
4.3.5 MRI data processing 41
4.3.6 Seed selection 42
4.3.7 Statistical analysis 43
4.4 Results 44
4.4.1 Participants' characteristics 44
4.4.2 Executive functions 46
4.4.3 Resting-state Functional Connectivity 48
4.4.4 Correlations between functional connectivity and BRIEF-A scores 52
4.5 Discussion 53
4.5.1 Limitations 56
4.6 Conclusion 56
4.7 Acknowledgment 57
4.8 Author contribution statement 57
4.9 Declaration of interests 57
4.10 References 57
CHAPTER 5 NEONATAL RS-FMRI ACQUISITION 64
5.1 CHU Sainte-Justine research neonatal acquisition protocol 64
5.2 Real-time head motion monitoring and MRI acquisition 65

5.3 Protocol optimization 69

CHAPTER 6 ARTICLE 2: NEORS: A NEONATAL RESTING STATE FMRI DATA PREPROCESSING PIPELINE 72

6.1 Abstract 72

6.2 Introduction 73

6.3 Materials and Methods 75

6.3.1 Data 75

6.3.2 Data structure 76

6.3.3 Pipeline overview 76

6.4 Data Processing 78

6.4.1 Structural 78

6.4.2 Functional 80

6.4.3 Denoising 82

6.4.4 Smoothing 84

6.5 Data Analysis - Functional Connectivity 84

6.5.1 Seed-Based Correlations (SBC) 84

6.6 Results 85

6.6.1 Image Registration 85

6.6.2 Skull stripping 86

6.6.3 Segmentation and Mask Creation 86

6.6.4 Functional Distortion Correction 88

6.6.5 Head Motion 89

6.6.6 Resting-state Networks - Seed-Based Correlations 91

6.7 Discussion 92

6.7.1 Limitations and Future Directions 95

6.8 Conclusion 96

6.9 Acknowledgements 97

6.10 Conflict of interests 97

6.11 Authors contributions 97

6.12 Funding 97

6.13 References 97

CHAPTER 7 GENERAL DISCUSSION 102

7.1 Resting-state fMRI in young adults born with congenital heart disease 102

7.2 Neonatal resting-state fMRI acquisition 102

7.3 NeoRS – resting-state fMRI image preprocessing pipeline 104

CHAPTER 8 CONCLUSION 106

REFERENCES 108

LIST OF TABLES

Table 2.1. Comparison of resting-state functional neuroimaging techniques (Mohammadi-Nejad et al., 2018). 7

Table 4.1 Participants' characteristics. 45

Table 4.2 BRIEF-A scales results..... 47

Table 4.3 Functional connectivity differences between CHD and control groups where CHD participants presented with lower functional connectivity than controls. 50

Table 4.4 Functional connectivity differences between CHD and control groups where CHD participants presented with higher functional connectivity than controls. 52

Table 5.1. Single-band rs-fMRI acquisition between centers comparison..... 71

LIST OF FIGURES

Figure 2.1. Representation of the positron-electron annihilation, creating two opposite direction photons of 511 KeV. 4

Figure 2.2. Vector representation of the spins aligned through the main magnetic field (B0), creating a net magnetization (M0). 8

Figure 2.3. Curves describing the relaxation times T1 and T2, respectively. 9

Figure 2.4. K-space trajectories for single-shot and blipped EPI. 12

Figure 2.5. Hemodynamic response function (Rangaprakash et al., 2021). 13

Figure 2.6. Example of GRE-EPI images presenting susceptibility and ghost artifact. 15

Figure 2.7. Graphical representation of the chemical shift artifact. 15

Figure 2.8. Neonatal resting-state networks characterized using independent component analysis (Ciarrusta et al., 2020). 19

Figure 2.9. Contrast differences between neonates and adults using MRI. 21

Figure 2.10. Workflow of a basic rs-fMRI pipeline (Mohammadi-Nejad et al., 2018). 22

Figure 2.11. Seed-to-seed correlation matrix. 24

Figure 2.12. Graph analysis based on connections (gray lines) and nodes (red ROIs)(Lv et al., 2018). 26

Figure 2.13. Group mean rs-fMRI correlation maps for different resting-state networks. Correlation maps are shown using Pearson correlation values r (W. Gao et al., 2015). 28

Figure 2.14. Representation of the Fisher transformation. 29

Figure 2.15. Group mean rs-fMRI correlation maps for different resting-state networks at term (A) and preterm (B). Correlation maps are shown using Fisher's z-transformed correlation coefficient z(r). (Smyser et al., 2016). 30

Figure 2.16. Gaussian distribution probability density plot. 31

Figure 2.17. Group mean rs-fMRI correlation maps for different resting-state networks in extremely preterm infants scanned at term-equivalent age. (A) Somatosensory and motor, (B) temporal/inferior parietal cortex encompassing the primary auditory cortex (*C*), posterior lateral and midline parts of the parietal cortex as well as the lateral aspects of the cerebellum (*D*), and medial and lateral sections of the anterior prefrontal cortex (*E*). Correlation maps are shown using standard Z-scores (Fransson et al., 2007). 32

Figure 2.18. Group mean rs-fMRI correlation maps of the somatosensory network. 33

Figure 4.1 Functional connectivity differences between CHD and control groups where CHD presented lower functional connectivity. 49

Figure 4.2 Functional connectivity differences between CHD and control groups where CHD participants presented with higher functional connectivity than controls. 51

Figure 5.1. CHU Sainte-Justine resting-state networks for different average framewise displacements (FD). 68

Figure 5.2. Baby Connectome Project resting-state networks for different average framewise displacements (FD). 69

Figure 6.1. Example of data naming and organization for NeoRS. 76

Figure 6.2. NeoRS workflow for neonatal resting-state functional connectivity processing and denoising. 77

Figure 6.3. Example of NeoRS input parameters. 78

Figure 6.4. T2-weighted and BOLD image registration to stereotaxic space. 85

Figure 6.5. Skull stripping parameters comparing default bet2 settings in neonates and NeoRS settings optimized for neonates. 86

Figure 6.6. One millimeter isotropic masks created from the tissue probability maps obtained with Mantis. White matter (red), CSF (yellow), gray matter (blue). 87

Figure 6.7. White matter, cerebrospinal fluid, and gray matter masks for regression of confounds. 87

Figure 6.8. Susceptibility-induced magnetic field inhomogeneity causing geometric distortions along the phase encoding direction..... 88

Figure 6.9. Example of head motion plots from a single subject. Plots are generated for each bold run and contain three different graphs per run..... 89

Figure 6.10. Two acquisitions of a high motion subject, run 1 excluded for having an average FD 0.25 mm, run 2 kept with an average FD < 0.25 mm..... 90

Figure 6.11. Example resting-state networks obtained by seed-based functional connectivity after image processing with NeoRS..... 91

Figure 6.12. Representative subject resting-state network example seed-to-seed functional connectivity correlations..... 92

LIST OF SYMBOLS AND ABBREVIATIONS

B0	Main magnetic field
BOLD	Blood-Oxygen-Level-Dependent
CHD	Congenital Heart Disease
CSF	Cerebrospinal Fluid
dHCP	Developing Human Connectome Project
EEG	Electroencephalography
EPI	Echo Planar Imaging
fNIRS	Functional Near Infrared Imaging System
FSPGR	Fast Spoiled Gradient
GRE	Gradient-Recalled Echo
HCP	Human Connectome Project
ICA	Independent Component Analysis
MEG	Magnetoencephalography
MPFC	Medial Prefrontal Cortex
MRI	Magnetic Resonance Imaging
M0	Net magnetization
PCC	Posterior Cingulate Cortex
PET	Positron Emission Tomography
RF	Radiofrequency
ROI	Region-of-Interest
RS-FC	Resting-state Functional Connectivity
rs-fMRI	Resting-state Functional Magnetic Resonance Imaging

RSN	Resting-State Networks
SAR	Specific Absorption Rate
SBC	Seed-Based Correlations
SE	Spin-Echo
sICA	Spatial Independent Component Analysis
SNR	Signal-to-Noise Ratio
T1	Longitudinal relaxation time
T2	Transverse relaxation time
TE	Echo Time
TR	Repetition Time
WM	White Matter

LIST OF APPENDICES

Appendix A supplementary materials article 1 125

CHAPTER 1 INTRODUCTION

The newborn brain is especially vulnerable to extreme prematurity and congenital heart disease (CHD). These are often associated with an increased risk of brain damage that can result in severe neurodevelopmental disability and long-term complications, such as cerebral palsy, autism, hyperactivity or neurocognitive delay (Brossard-Racine et al., 2016; Franz et al., 2018; Limperopoulos et al., 2008; Volpe, 2009).

Magnetic Resonance Imaging (MRI) showed that very preterm infants (born at ≤ 32 weeks of gestation) presented different types of white matter injury, such as periventricular leukomalacia, which is the most common form of brain injury in premature births (Smyser, Wheelock, Limbrick, & Neil, 2019). Furthermore, ultrasounds in Canada revealed that approximately 21% of very preterm infants presented structural brain anomalies such as intraventricular hemorrhage, the second most common form of preterm brain injury (Ryan, Lacaze-Masmonteil, & Mohammad, 2019). Moreover, CHD is also a significant cause of perinatal brain injury, with around 8 in 1000 births per year in Canada (Irvine, Luo, & Leon, 2015), and consists of structural malformations of the heart and vessels, resulting in blood flow impairment. This blood flow impairment reduces cerebral oxygen during brain maturation, leading to poor development (Kelly et al., 2017) and increased risk of injury during heart surgery (Newburger & Bellinger, 2006).

While it is well known that perinatal brain injury has devastating long-term effects on the infant's brain, the consequences may differ for each individual. Until recently, the examination of these lesions and the functional impact was based on neuroanatomical techniques offering little information on the evolution of the disease. Therefore, intending to improve the long-term life quality of these infants, it is warranted to find new brain integrity biomarkers that are reliable and non-invasive, allowing thereafter prompt brain injury diagnosis to apply therapy to minimize future complications.

A promising approach is the study of resting-state functional connectivity (RS-FC), as it would provide complementary information to structural imaging related to brain physiology. In this sense, the analysis of resting-state neural networks is encouraging since they have been shown to emerge as early as the third trimester of gestation (Doria et al., 2010) with substantial disruptions during

preterm birth (Enguix, Ding, & Lodygensky, 2018). Furthermore, clinically, the impact of brain damage on the different resting-state networks (RSN) would offer advances in prognosis since these impairments, although present at birth, are usually expressed at school age.

Several neuroimaging techniques exist to study functional connectivity. Nonetheless, the main focus of this project is on resting-state functional Magnetic Resonance Imaging (rs-fMRI), as it has already shown its potential in the study of this clinical population (W. Gao, Lin, Grewen, & Gilmore, 2017; Grayson & Fair, 2017; Keunen, Counsell, & Benders, 2017; Power, Fair, Schlaggar, & Petersen, 2010; Smyser & Neil, 2015; H. Zhang, Shen, & Lin, 2019). Moreover, rs-fMRI is a good technique for studying newborns as it is non-invasive and doesn't need participant collaboration. Also, MRI allows access to the deeper layers of the brain, providing consistent information about the high-order associative and low-level sensory resting-state networks. It also presents a good compromise between spatial resolution/signal-to-noise ratio (SNR) and an acceptable temporal resolution when using advanced acquisition techniques such as multi-band excitations. Furthermore, MRI allows multimodal acquisitions in a single scanning session providing information about the brain function and structure (i.e., T2-weighted, T1-weighted, diffusion tensor imaging).

Nevertheless, despite the great possibilities of rs-fMRI, the study of the newborn brain presents several methodological challenges related to data acquisition, preprocessing, and analysis that must be addressed. First, infants present higher head motion levels than adults, meaning that head movement artifacts might alter data quality. Image preprocessing tools exist for adults, but they are challenging to apply to neonates because of the constant growth or the inversion of the white/gray matter contrasts due to myelination, making neonatal image preprocessing very complex.

To overcome the challenges mentioned above, this project aims to shed light on the different approaches needed to acquire and preprocess neonatal resting-state data successfully. It includes an acquisition protocol, a real-time head motion quality control procedure, and NeoRS, an open-source pipeline to preprocess neonatal rs-fMRI data from different datasets. Additionally, a rs-fMRI study performed on youth born with congenital heart disease was carried out initially to understand the state-of-the-art preprocessing methods in mature brains. Furthermore, this study provides insights into the potential long-term effects that congenital heart malformations may have on resting-state networks.

CHAPTER 2 LITERATURE REVIEW

2.1 Functional neuroimaging techniques

Functional neuroimaging is a biomedical imaging technique detecting changes in brain metabolism and blood flow to understand brain activity. Between the most used functional neuroimaging techniques we can distinguish functional MRI (fMRI), functional positron emission tomography (functional PET), electroencephalography (EEG), magnetoencephalography (MEG), and functional near-infrared imaging system (fNIRS).

2.1.1 Functional positron emission tomography

Positron emission tomography (PET) provides information about brain function based on metabolic activity while performing a task or in a resting-state. Intravenous injection introduces a glucose molecule into the body labeled with a positron-emitter radionuclide, typically [^{18}F] fluorodeoxyglucose. The positron-emitter radionuclide is called a PET-tracer. During this process, the radionuclide emits positrons interacting with the immediate environment, annihilating the surrounding electrons. The electron-positron annihilation results in a pair of γ-photons of 511 keV traveling in opposite directions (Schaart, 2021)(Figure 2.1). To create the functional map, the scanner measures these photons to identify the region where the metabolic activity comes from (A. Kumar & Chugani, 2013). PET has been widely used in adults to explore the resting-state networks in different brain diseases such as neuropsychiatric disorders (Savio et al., 2017), depression (Fang et al., 2016) or Alzheimer's disease (Toussaint et al., 2012). However, despite having several clinical applications, the most common use of PET is in oncologic imaging for tumor detection (Anand, Singh, & Dash, 2009). In newborns, very few resting-state functional connectivity studies using PET exist (Thorngren-Jerneck et al., 2001). Probably, due to ethical concerns regarding exposure to radioactive products. PET offers a spatial resolution of 4 mm and a temporal resolution of 60 seconds or less (Jamadar et al., 2020). In contrast to conventional PET, this temporal resolution can be achieved by constant infusion of the PET-tracer (Li et al., 2020).

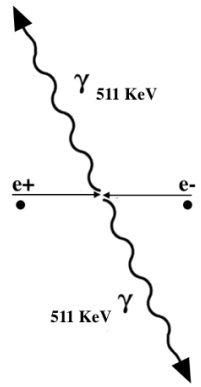

Figure 2.1. Representation of the positron-electron annihilation, creating two opposite direction photons of 511 KeV.

2.1.2 Functional MRI

fMRI allows for mapping the brain activity between different brain areas based on slow frequency changes associated with the Blood-Oxygen-Level-Dependent (BOLD) signal (Ogawa, Lee, Kay, & Tank, 1990; Ogawa et al., 1993). In contrast to diffusion tensor imaging, which provides micro-structural connectivity maps (Babaeeghazvini, Rueda-Delgado, Gooijers, Swinnen, & Daffertshofer, 2021), fMRI measures brain activity of different regions working simultaneously, providing information related to brain function. When performing fMRI acquisitions, we can distinguish between task-based and resting-state modalities. Task-based fMRI consists of demanding the subject to perform a task to observe brain activity while performing the task. In contrast with task-based fMRI, resting-state fMRI measures brain activity while the subject is not performing any task (Smitha et al., 2017). As asking a newborn to complete a task is not easy, we mainly use the resting-state approach. Furthermore, resting-state fMRI allows obtaining, from a single acquisition, global information about the brain's functional connectivity (Smyser et al., 2019).

The most common clinical, yet rare, applications of resting-state fMRI are preoperative mapping for brain tumor surgery (V. A. Kumar et al., 2020; Lee, Smyser, & Shimony, 2013; Smirnov et al., 2020; D. Zhang et al., 2009). Furthermore, it is also used to perform between-group comparisons to understand psychiatric diseases such as autism spectrum disorder, schizophrenia, and

Alzheimer's disease (Lee et al., 2013). In neonates, the available studies have concentrated on prematurity and hypoxic-ischemic encephalopathy (Smyser et al., 2019). Resting-state fMRI also allowed in-utero functional connectivity acquisition, showing the presence of the resting-state networks before birth (van den Heuvel & Thomason, 2016). Different neonatal studies also confirmed the existence of the resting-state networks from the third trimester of gestation (Doria et al., 2010) and that they can be modeled for extreme prematurity cases by adequate neonatal intense care (Smyser et al., 2013). Also, it has been shown that healthy neonatal brains present the same functional connectivity network patterns (Fransson et al., 2007). Finally, resting-state fMRI has a spatial resolution of around 2-3 mm and a temporal resolution of about 2-3 seconds when using single-band acquisitions and < 1 second when using multi-band acquisition techniques.

2.1.3 Electroencephalography

EEG measures the spontaneous electrical signal through electrodes placed on the scalp directly produced by neuronal activity (Biasiucci, Franceschiello, & Murray, 2019). Similarly to resting-state fMRI, EEG can be performed in a resting-state (Xue et al., 2020); however, few studies have been performed in resting-state. Until now, infant resting-state EEG has been used to study autism spectrum disorders (Bosl, Tierney, Tager-Flusberg, & Nelson, 2011; Tierney, Gabard-Durnam, Vogel-Farley, Tager-Flusberg, & Nelson, 2012). As awake EEG, it presents a temporal resolution in the millisecond range and a spatial resolution of around 2-3 cm. But, despite its excellent temporal resolution, the biggest limitation of EEG to measure functional connectivity is its bad spatial resolution and that it only provides information about the potential difference between two separate regions (Mohammadi-Nejad et al., 2018).

2.1.4 Magnetoencephalography

MEG is a functional imaging technique that measures neural activity through small magnetic fields created by the electrical currents produced by neural activity (Alhourani et al., 2016). It can be done task-based or in a resting-state. Similar to EEG acquisitions, MEG allows a direct measure of brain activity based on electrical signals, but with the advantage of being less affected by muscular activity and skull conductivity (Tamilia, Madsen, Grant, Pearl, & Papadelis, 2017). Furthermore, it doesn't require sensors to be connected to the head. Still, despite these advantages, MEG presents some drawbacks. First, it only measures cortical signals (Singh, 2014). The system has to be

adapted to the head size to obtain a suitable signal-to-noise ratio in infants (T. P. Roberts et al., 2014). Finally, MEG offers an excellent temporal resolution of less than 1 ms and a sub-millimeter spatial resolution (Mohammadi-Nejad et al., 2018).

2.1.5 Functional Near Infrared Spectroscopy

fNIRS is an optical neuroimaging system that uses near-infrared spectroscopy to measure brain activity through the hemodynamic response. It measures the local concentration of oxyhemoglobin and deoxyhemoglobin based on their different reflectance coefficients (Boas, Dale, & Franceschini, 2004). Furthermore, it allows measuring through the skull, which is crucial in clinical conditions. Several studies on neonates using fNIRS showed that resting-state networks could provide diagnostic and prognostic information on newborn brain development (Homae et al., 2010; Imai et al., 2014; White, Liao, Ferradal, Inder, & Culver, 2012). This technique is appropriate for neonates for its portability and non-invasiveness; however, the biggest drawback of fNIRS is the limited access to superficial layers of the brain (Peng & Hou, 2021). fNIRS offers a temporal resolution of 20 ms and a spatial resolution of 1-3 cm.

2.1.6 Final comparisons

PET imaging is widely used for oncology, neurosurgery, or cardiac diagnosis. It allows the study of the deep layers of the brain and presents a spatial resolution of around 4 mm, and its temporal resolution is between 30 and 40 s (Table 2.1). However, requiring radioactive product administration limits its utilization in newborns, especially in research settings.

Like PET imaging, resting-state fMRI also allows access to the deep layers of the brain, which is not the case for EEG, MEG, and fNIRS. Access to the deeper brain regions implies further and more complete characterization of the resting-state network topology, which could provide crucial information about brain development. Furthermore, resting-state fMRI offers a spatial resolution of around 2-3 mm, depending on the strength of the magnetic field. fMRI good spatial resolution provides more detailed images than EEG (2-3 cm) and fNIRS (1-3 cm). Also, even if resting-state fMRI spatial resolution is not optimal for image segmentation, it is easy to acquire high-resolution T2-weighted images to obtain optimal data for segmentation without changing the patient's position.

Additionally, multi-band acquisition techniques can dramatically improve temporal resolution. For example, the data acquired in the Developing Human Connectome Project (dHCP) presented a TR of 0.4 s (Edwards et al., 2022). The biggest drawback of resting-state fMRI, when compared to EEG, MEG, and fNIRS, is its complexity and price. Despite the advantages of rs-fMRI, like fNIRS, rs-fMRI doesn't measure direct brain activity, as it is based on delayed hemodynamic activity. Nonetheless, resting-state fMRI seems to be the most adapted functional neuroimaging technique for studying neonatal resting-state networks. It is the most complete of the aforementioned neuroimaging systems. It is non-invasive, allows access to the deep layers of the brain, and presents adequate spatial and temporal resolution.

Table 2.1. Comparison of resting-state functional neuroimaging techniques (Mohammadi-Nejad et al., 2018).

Resting-state neuroimaging technique	**Spatial resolution**	**Temporal resolution**	**Image obtained by**	**Deep brain access**
Functional PET	4 mm	~12-60 s	Metabolic activity	Yes
Functional MRI	2-3 mm	~1 s	Hemodynamic activity	Yes
Electroencephalography (EEG)	2-3 cm	< 1 ms	Electrical neural signals	No
Magnetoencephalography (MEG)	< 1 mm	< 1 ms	Magnetic neural signals	No
Functional Near Infrared Imaging System (fNIRS)	1-3 cm	20 ms	Hemodynamic activity	No

2.2 MRI Basic principles

A brief explanation of the fundamental MRI concepts is presented in this section to understand better its basic principles, tissue properties, acquisition parameters, and pulse sequences.

MRI allows the exploration of body tissue based on the magnetic properties of protons in the atomic nuclei of the hydrogen contained in the water molecules. The atomic nuclei present specific energy levels related to the quantum property spin (quantum number S). For example, the hydrogen proton has a spin quantum number of 1/2 and two different energy states -1/2 and +1/2, being the number of energy states defined as:

$$\text{Number of energy states} = 2S + 1$$

These protons are constantly spinning and have their own small magnetic fields. Each of these local magnetic fields is called a magnetic dipole moment and are randomly arranged to cancel each other out, resulting in a null net magnetic field. Therefore, for the MRI to work, a net magnetic field is needed. To achieve this, spins are placed under a strong magnetic field (B0) that forces them to align with the stronger magnetic field. As a result, slightly more protons are aligned with B0 than against it, resulting in a net magnetization (M0) in the B0 direction (Figure 2.2). Furthermore, these spins precess within B0 at a frequency called the Larmor frequency described by the equation:

$$f_0 = \gamma \cdot B0$$

Where f_0 is the precession frequency, and γ the gyromagnetic ratio of the hydrogen nucleus (45.58 MHz/Tesla).

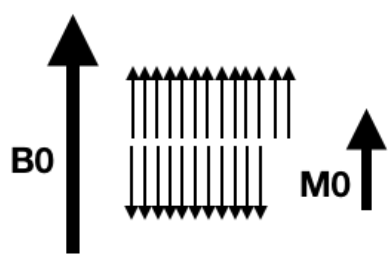

Figure 2.2. Vector representation of the spins aligned through the main magnetic field (B0), creating a net magnetization (M0).

The protons will then be excited by a radiofrequency (RF) pulse whose frequency matches the Larmor frequency. This is when resonance occurs and results in added energy to the protons. Protons are then flipped, creating a magnetization vector in the x-y plane (Mxy). After applying the RF pulse, the protons will return to their original state. During this relaxation process, data acquisition will be performed by measuring the signal induced by the relaxing protons. Different

magnetic field gradients in the three planes are employed to spatially locate the origin of every signal to create a 3D image.

It is important to note that the strength of the main magnetic field plays an essential role in MRI image quality. Stronger magnetic fields allow better signal-to-noise and contrast-to-noise ratio, allowing to observe smaller structures; however, they also present several challenges, such as enhanced susceptibility artifacts, non-uniform radiofrequency fields, or a higher deposit of energy (Ladd et al., 2018).

2.2.1 T1, T2 and T2* relaxation times

During the relaxation process, the spins return to their original energy state by releasing the energy received from the radiofrequency pulse. Therefore, we can distinguish between two types of relaxation, T1 relaxation, also called longitudinal or spin-lattice relaxation and T2 relaxation, also called transverse relaxation or spin-spin relaxation. T1 relaxation time corresponds to the necessary time required to recover the net magnetization (M0) to 67% of its initial value and can be described by the expression $1 - e^{-t/T1}$. T2 relaxation time corresponds to the time required for the transverse magnetization to decay to approximately 37% of its initial value and can be described by the expression $e^{-t/T2}$ (Figure 2.3).

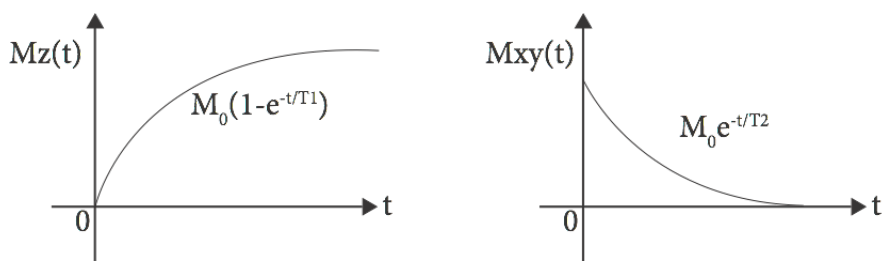

Figure 2.3. Curves describing the relaxation times T1 and T2, respectively.

Finally, the T2* relaxation time corresponds to the spin-spin interactions of the tissue as for T2, plus the main magnetic field inhomogeneities effect. This effect is never fixed as it depends on B0 homogeneity and produces a faster decay than T2. This effect can be expressed as:

$$\frac{1}{T2^*} = \frac{1}{T2} + \frac{1}{\mathrm{T2i}}$$

Where $1/T2i = \gamma \Delta Bi$ corresponds to the relaxation rate produced by the magnetic field inhomogeneities across a voxel.

2.2.2 TE, TR and tissue contrast

The previously mentioned process must be repeated several times to create an image. This is where echo time (TE) and repetition time (TR) come into play. In contrast to T1 and T2 relaxation times that are directly related to tissue properties, the TE and TR can be controlled by the user to acquire images with different weighting, such as T1-weighted, T2-weighted or spin-density.

Multiple RF pulses are usually applied to perform the entire acquisition. The time between two RF pulses is the TR. On the other hand, the TE corresponds to the time after excitation before the signal is measured, so the transverse magnetization decay is compensated to create an echo at TE. If we measure right after the RF pulse is applied, the signal would equal the original magnetization M0. As the longitudinal magnetization recovery and the transverse magnetization decay occur at the same time, we need to combine both effects to obtain the desired signal intensity for a given tissue, which for a classic spin-echo (SE) is described as:

$$S_{SE} = M0 \left(1 - e^{-\frac{TR}{T1}}\right)\left(e^{-\frac{TE}{T2}}\right)$$

Where M0 is the Boltzmann magnetization constant corresponding to the spin density.

We can note from the previous equation that when TE is made very short when compared to T2, TE/T2 would be approximately zero and $e^0 = 1$, nullifying the T2 weighting. Contrary to this, if TR is made long when compared to T1, then $e^{-TR/T1}$ would tend to zero canceling this way, the T1 weighting. In summary, to obtain T1-weighted images, short TR and TE are required. To get T2-weighted or T2*-weighted images, long TR and TE are needed, and finally, if very long TR and short TE are employed, both T1 and T2 effects would disappear, resulting in an image of the proton density of the tissue.

2.2.3 Pulse sequences

A pulse sequence consists of a sequence of RF pulses that are applied repeatedly. Here, three of the most popular pulse sequences will be briefly described as they are highly interesting for understanding this project.

2.2.3.1 Spin-echo

The spin-echo pulse sequence is one of the first developed and is still commonly used. This pulse sequence consists of the application of a 90º RF pulse followed by a 180º refocusing pulse allowing to eliminate the effect of the magnetic field inhomogeneities.

2.2.3.2 Gradient-recalled echo (GRE)

Another commonly used pulse sequence is the gradient echo. This is an alternative to spin echo as the use of smaller flip angles allows the use of a very short TR value decreasing this way the scan time, being the scan time defined as:

$$Scan\ time = TR * Ny * NEX$$

Being TR the repetition time, Ny the number of phase encoding steps (usually selected to achieve a specific resolution), and NEX the number of excitations (typically employed to achieve a certain SNR).

The idea of the GRE is to select the smallest TR while still being able to receive enough echo to create an image. With this aim, small flip angles are used. The Ernst angle is the flip angle that maximizes tissue signal (Ernst & Anderson, 1966). For instance, the signal in GRE-EPI is defined as:

$$S_{GRE} = M0\ e^{-\frac{TE}{T2}*} \frac{(1 - e^{-\frac{TR}{T1}}) \sin\theta}{1 - e^{-\frac{TR}{T1}} \cos\theta}$$

Being θ the flip angle.

Suppose a 90º flip angle is employed with a very short TR. In that case, the longitudinal magnetization has not enough time to recover to a suitable value, and a very low SNR is obtained.

2.2.3.3 Echo Planar Imaging

Echo planar imaging is one of the fastest MRI sequences and requires high-performance gradients to allow rapid switches. There exist two types of EPI sequences, single-shot EPI and multi-shot EPI. Single-shot EPI allows the acquisition of the whole k-space in a single TR. Originally, this was performed by employing a constant phase encoding gradient producing a zig-zag filling of the k-space and producing some artifacts after Fourier Transformation. Therefore, a blipped phase

encoding gradient is used to correct these artifacts instead of utilizing a continuous phase encoding gradient. There is, therefore, a short time of around 100 μs between every step that allows jumping from line to line to avoid zig-zag trajectories (Figure 2.4).

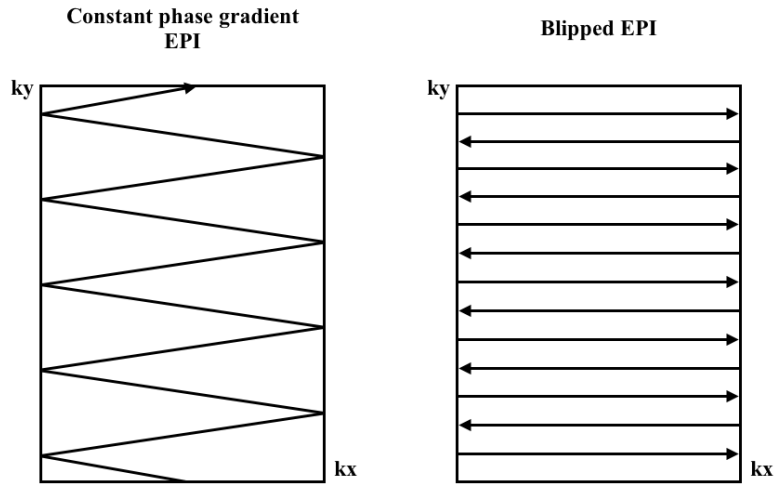

Figure 2.4. K-space trajectories for single-shot and blipped EPI.

The other form of EPI sequence is the multishot EPI, where the readout is divided into multiple shots allowing the acquisition of the whole k-space in a few segments. The number of echoes or lines of the k-space acquired every shot is called the echo train length. Compared to single-shot EPI, this technique creates less stress in the gradients. However, the acquisition is slower, being more susceptible to motion artifacts.

2.3 Resting-state fMRI

2.3.1 Blood-Oxygen-Level-Dependent signal

Resting-state fMRI measures brain activity based on slow frequency fluctuations (<0.1 Hz) in the BOLD signal (Ogawa et al., 1990; Ogawa et al., 1993). It consists of measuring localized changes in the deoxyhemoglobin produced by blood oxygenation (Drew, 2019). Brain activity in a specific region is directly linked to an increased blood flow in that region, providing higher quantities of oxygen and glucose for neuronal activity (Vincent, Moore, Kennedy, & Tracey, 2009). This local increase in blood flow is known as the hemodynamic response (Rangaprakash, Tadayonnejad,

Deshpande, O'Neill, & Feusner, 2021) (Figure 2.5). In addition, the local oxygenation produces changes in the magnetic field homogeneity that can be measured using T2* sensitive sequences.

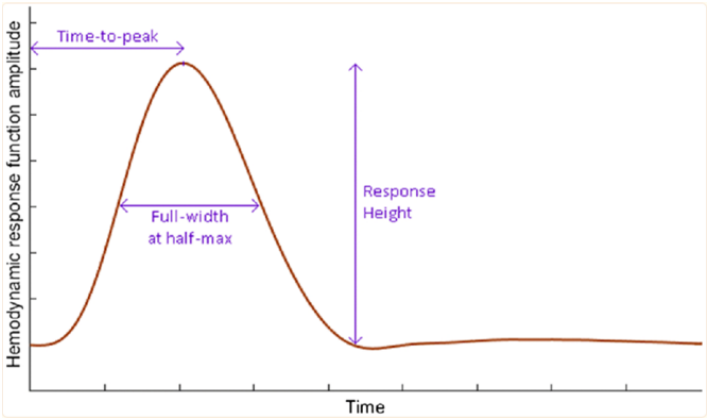

Figure 2.5. Hemodynamic response function (Rangaprakash et al., 2021).

2.3.2 EPI contrast

As previously mentioned, single-shot EPI is one of the fastest MRI sequences. Therefore, it is suitable for BOLD signal acquisition when setting the TE as close as possible to the T2* of the gray matter, being, thus, the state-of-the-art pulse sequence to acquire rs-fMRI data.

The contrast of EPI is determined by the excitation pulse, which can also be called the root pulse sequence, which is applied before the EPI module. Some of the possibilities are

- SE-EPI: 90º - 180º - It allows to overcome magnetic field inhomogeneities and provides T2 weighting.

- GRE-EPI: αº - It doesn't use the 180º pulse providing T2* weighting. This technique is faster and, therefore, the most suitable for resting-state fMRI acquisitions.

Other possibilities exist, such as inversion recovery-EPI or diffusion weighted-EPI, but they are outside this project's scope.

2.3.3 GRE-EPI artifacts

GRE-EPI is the most suitable for resting-state fMRI for allowing high-speed acquisition, providing a decent temporal resolution, minimizing head motion artifacts, and being susceptible to BOLD signals. However, one of the technical problems of this technique is the high susceptibility to artifacts. Amongst the most commonly observed when using single-shot GRE-EPI are susceptibility artifacts, chemical shift, and Nyquist ghost artifacts (Figure 2.6 and Figure 2.7). Susceptibility artifacts consist of a signal loss in the air/tissue interfaces, mainly in the sinuses (Newton, 2016), in the phase encoding direction. They can be minimized by proper shimming, TE reduction, or post-acquisition distortion correction approaches that we will discuss further. The chemical shift in EPI also occurs along the phase encoding direction and consists of a phase difference between the water and fat. To correct it, it is possible to decrease echo spacing, undersample the k-space or use fat suppression. Finally, Nyquist ghost artifacts involve signal displacement in the phase encoding direction. The causes of this artifact might be due to poor shimming, heating of the gradient coils, or head motion. However, the most common cause of Nyquist ghost artifact is the induction of eddy currents in the coils due to the rapid gradient changes that produce distortions in B0, adding phase shifts to the data. Some methods to reduce Nyquist ghost artifacts are shimming, lowering the phase encoding resolution, or using parallel imaging acceleration to increase the bandwidth per pixel along the phase encoding direction, shortening the readout time (Bammer et al., 2001; Griswold et al., 1999). Finally, if the artifacts persist, proper tuning of the gradients can also help.

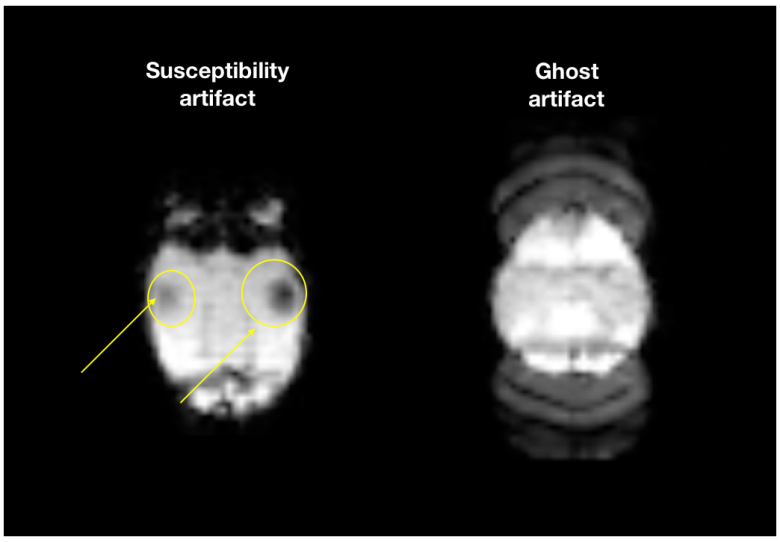

Figure 2.6. Example of GRE-EPI images presenting susceptibility and ghost artifact.

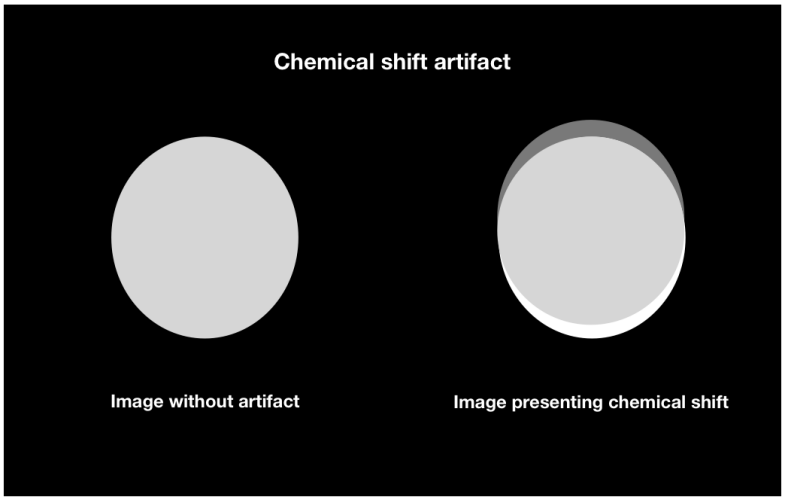

Figure 2.7. Graphical representation of the chemical shift artifact.

2.3.4 Multi-band EPI

Multi-band EPI acquisition, also called simultaneous multislice acquisition technique, is a recently adopted technique for resting-state fMRI acquisitions, which consists of simultaneously exciting and acquiring signals from several slices depending on the selected multi-band factor. For example, a multi-band factor of 8 means that eight slices will be simultaneously excited. The multi-band-

EPI acquisition allows shorter TR, resulting in improved temporal resolution and an increased number of acquired time points for a given acquisition time (Risk et al., 2021). It is also less susceptible to head motion and allows the possibility to improve spatial resolution. However, the major drawback of multi-band rs-fMRI is the degradation of the SNR due to the non-uniform noise created by the geometrical arrangement of the receiver coil (g-factor). This creates different levels of SNR in the different regions of the brain (Bouyagoub, Dowell, Gabel, & Cercignani, 2021; Robson et al., 2008). Yet, results have shown negligible differences when analyzing rs-fMRI and multi-band rs-fMRI data (Smitha et al., 2018).

2.3.5 Multi-echo rs-fMRI

A single RF excitation pulse is used to acquire a whole brain volume when using single-shot GRE-EPI rs-fMRI. Also, as previously mentioned, the TE is centered around the T2* of the gray matter, so every RF pulse data is acquired at a single time delay (TE); this acquisition approach is called single-echo rs-fMRI. Recently, an alternative approach is multi-echo rs-fMRI which consists in acquiring several TE per RF excitation pulse. The acquisition of several TE would allow obtaining information about the non-neural sources of signal, such as head motion, cardiac, respiratory, or hardware-related signals to be eliminated as they are not TE dependent. Furthermore, it is possible to approximate the signal at a voxel as a monoexponential decay of the form:

$$S(t) = S_0 e^{-\frac{t}{T2^*}}$$

Where S_0 is the signal intensity after the RF pulse when t=0. When performing single-echo rs-fMRI, it is impossible to determine if the signal changes in a voxel from volume to volume are due to a change in the decay rate 1/T2* or a change in S_0. However, by acquiring several TE, it is possible to determine whether the signal change is S_0 or 1/T2* related, as neural signals mainly produce changes in 1/T2* and non-neural signals produce changes in S_0 (Power et al., 2018).

Multi-echo acquisitions also improve the statistical power of regions with short T2* where typically there is signal dropout due to selected TE. Using a weighted average from the combination of several echoes results in a dramatic reduction of the signal dropouts, however, increased TR is needed to perform the equivalent single-echo rs-fMRI as additional echoes require a longer time (Kundu et al., 2017).

2.3.6 Functional connectivity and resting-state networks

Resting-state functional connectivity measures the temporal correlation of spontaneous BOLD signals between different brain regions. The regions with correlated activity create functional networks, and these functional networks are what we call a resting-state network (Woodward & Cascio, 2015). It is important to mention that other measures of brain connectivity exist such as structural and effective connectivity. Structural connectivity refers to anatomically connected brain regions by white matter tracts (Babaeeghazvini et al., 2021). Effective connectivity can be described as a combination of structural and functional connectivity. It describes the causal influence between neural units (Z. Liu et al., 2017; Stephan & Friston, 2010). However, in this literature review, we will only focus on functional connectivity as the other measures of connectivity are outside of the scope of this project.

Along with other functional neuroimaging techniques, resting-state fMRI has been able to consistently identify and reproduce resting-state networks of healthy subjects across the lifespan. Resting-state fMRI also allowed the characterization of the canonical resting-state networks including the default mode, the executive control, the salience, the sensorimotor, the auditory, and the visual network (Hausman et al., 2020; Heine et al., 2012). The default mode network includes the medial prefrontal cortex, the posterior cingulate cortex, and the angular gyrus and is related to internal and self-related processes (Whitfield-Gabrieli et al., 2011). The executive control network includes the dorsolateral prefrontal cortex and the anterior cingulate cortex and was observed to appear lateralized. The left executive control was shown to be related to language and cognition, and the right executive control to perceptual, nociception, and somesthetic processing (Laird et al., 2011; Smith et al., 2009). The salience network includes the anterior cingulate and fronto-insular cortex with connections to limbic structures. It is related to conflict monitoring, response selection, and information integration (Cole & Schneider, 2007; K. L. Roberts & Hall, 2008). The sensorimotor network includes the supplementary motor, the primary motor cortex, and the bilateral mid-frontal gyri, and shows the activation patterns observed in motor tasks (Biswal, Yetkin, Haughton, & Hyde, 1995). The auditory network includes the bilateral superior temporal gyri, the posterior insular cortex, and Heschl's gyrus and is associated to pitch and tone discrimination and speech (Laird et al., 2011). Finally, the visual network can be divided into three networks. The lateral or secondary visual network, including the peristriate area and the superior occipital and lateral gyrus, is related to complex emotional stimuli. The medial or primary visual

network, including the striate and parastriate regions, is important to simple visualization. And the occipital visual network, including the occipital pole, is related to high-level visual processing such as orthography (Heine et al., 2012; Wang et al., 2020).

2.3.7 Related works

Several neonatal rs-fMRI studies have shown the potential of this neuroimaging technique, and significant steps have been made in the last decade. Thus, it could be applied in the neonatal period to develop new neuroprotective drugs. Furthermore, as we will see in older infant studies, rs-fMRI has been able to detect the impact of diseases in very difficult to diagnose mental disorders. Some examples are attention deficit, hyperactivity, autism, or the Syndrome of Tourette. This section presents the recent findings on clinical neonatal resting-state networks.

2.3.8 Clinical neonatal rs-fMRI

We define the resting-state network as the different brain regions that show synchronous activity. They can also be called intrinsic connectivity networks or functional brain systems (Seitzman, Snyder, Leuthardt, & Shimony, 2019) and allow the characterization of brain function. In recent years the study of resting-state networks has exponentially increased due to their versatility and potential to identify and predict the progression of brain diseases (J. J. Chen, Herman, Keilholz, & Thompson, 2020; Westphal et al., 2017). Indeed, since the discovery of resting-state networks in 1995 (Biswal et al., 1995), rs-fMRI studies have led to a better understanding of brain architecture and brain development (W. Gao et al., 2017; Grayson & Fair, 2017; Keunen et al., 2017; Power et al., 2010; Smyser & Neil, 2015; H. Zhang et al., 2019). Furthermore, resting-state networks in newborns are consistently observed and present a high resemblance to adult networks (Figure 2.8) (Ciarrusta et al., 2020; Fransson et al., 2009; Fransson et al., 2007; W. Gao et al., 2009). Interestingly, rs-fMRI allowed the in-utero acquisition, showing the presence of resting-state networks before birth and prompt signs of vulnerability (van den Heuvel & Thomason, 2016).

Different neonatal studies also confirmed the existence of resting-state networks from the third trimester of gestation (Doria et al., 2010). When studying the motor cortex, Smyser et al. found that the effect of white matter injury on the BOLD signal was proportional to injury severity. Also, they proved the viability of using rs-fMRI to explore the resting-state networks alterations associated with premature birth and white matter injury (Smyser et al., 2013). Furthermore,

alterations of the ventral attention and default mode networks at birth were shown to be related to behavioral inhibition at two years old (Sylvester et al., 2018), which opens the opportunity for early diagnostics and treatment. Also, in older infants, rs-fMRI found aberrant functional connectivity in different mental disorders such as hyperactivity disorder, autism spectrum disorder, or Tourette Syndrome (Church et al., 2009; Fair et al., 2010; T. B. Jones et al., 2010). Finally, Smyser et al. showed that term and preterm babies scanned at comparable postmenstrual age presented differences in high-order networks (language, default mode, and frontoparietal networks), suggesting that rs-fMRI may be a convenient tool for identifying prematurely born infants at risk of neurodevelopmental impairment (Smyser et al., 2016).

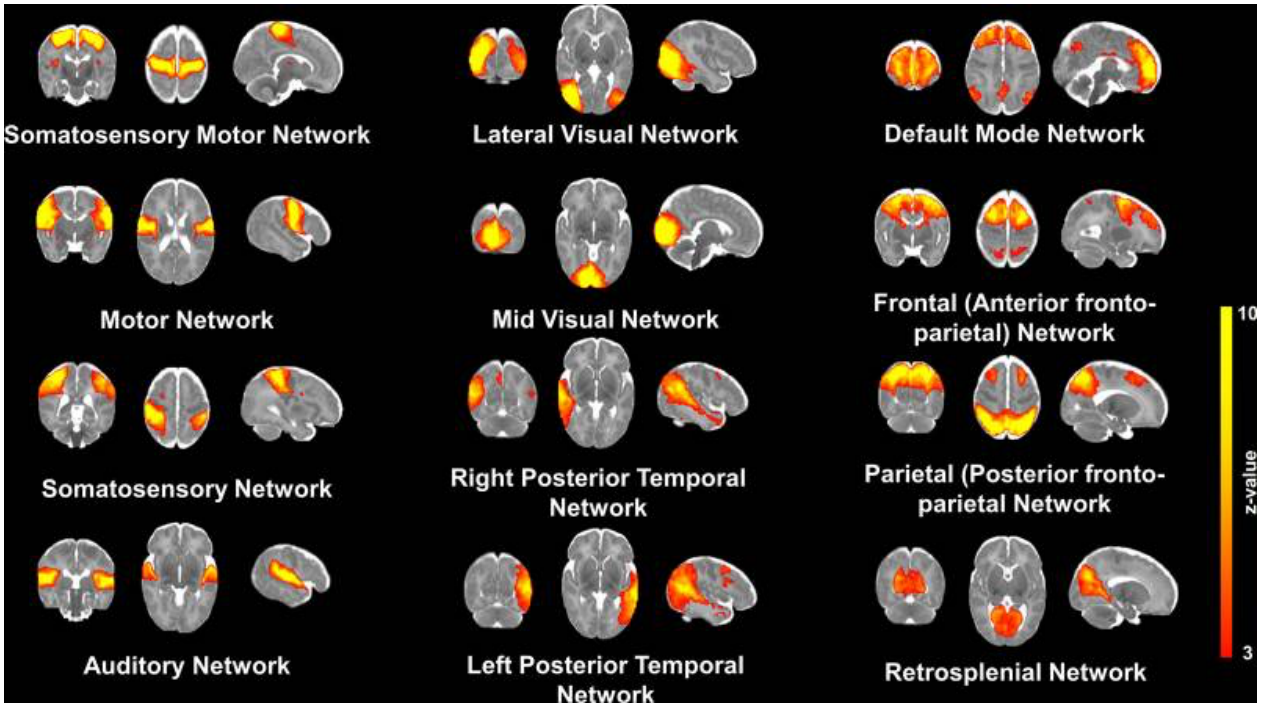

Figure 2.8. Neonatal resting-state networks characterized using independent component analysis (Ciarrusta et al., 2020).

2.3.9 Challenges on neonates

Even if the study of resting-state networks in neonates is a promising approach, its clinical application presents diverse methodological challenges. It is well known that the resting-state

networks signal is very stable across subjects (Lee et al., 2013); however, different artifacts and confounders can easily affect it. Amongst the most common, we can find susceptibility distortions, head motion (Maknojia, Churchill, Schweizer, & Graham, 2019), and or cerebrospinal fluid (CSF) and white matter (WM) signals (Jo et al., 2013; Power et al., 2014). For these reasons, robust data preprocessing is imperative to limit the undesirable effects of the signals coming from non-neural sources so the resting-state networks can be assessed appropriately (Giove, Gili, Iacovella, Macaluso, & Maraviglia, 2009; Lund, Madsen, Sidaros, Luo, & Nichols, 2006).

There are available tools to preprocess resting-state fMRI data in the adult brain. Still, preprocessing the newborn resting-state fMRI data requires using modified methods (Smyser & Neil, 2015). For example, the newborn brain size varies depending on the participant's age at the scan (Smyser & Neil, 2015), making adult skull-stripping tools less robust for newborns. Also, different age-specific templates are needed for precise segmentations, normalization, and seed-based connectivity analysis. Furthermore, when scanning newborns, choosing the different acquisition parameters is particularly critical. The baby's brain has more water and lower lipid content due to myelination and synaptic formations. Hence, T2-weighted images are necessary to produce sufficient contrast for tissue segmentation (Askin Incebacak et al., 2022) (Figure 2.9). Yet, increasing the TE to increase the T2 effect results in a lower signal because transverse magnetization has time to fall to low values. Moreover, newborns present higher levels of motion and must be handled using specific tools (Badke D'Andrea et al., 2022; Smyser & Neil, 2015). Real-time motion monitoring technologies, such as FIRMM (Dosenbach et al., 2017), can be employed, although open-source solutions are not yet available.

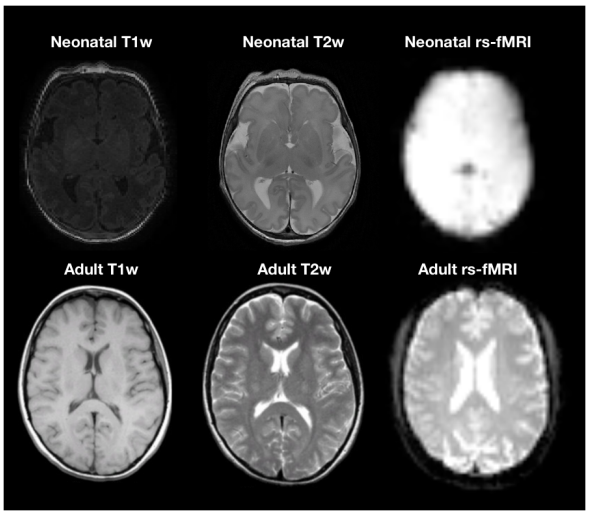

Figure 2.9. Contrast differences between neonates and adults using MRI.

2.4 Image preprocessing

Image preprocessing refers to the operations of images at the most basic level. It aims to improve the image by reducing unwanted distortions or enhancing specific features important for subsequent analysis steps.

As previously mentioned, several tools exist to preprocess adult resting-state fMRI data. Amongst the most employed toolkits in which nearly all pipelines lie, we find SPM (https://www.fil.ion.ucl.ac.uk/spm/), AFNI (Cox, 1996) and FSL (Jenkinson, Beckmann, Behrens, Woolrich, & Smith, 2012; Smith et al., 2004; Woolrich et al., 2009). SPM, AFNI, and FSL are open-source software libraries containing tools to preprocess and display neuroimaging data. SPM is a Matlab based software package developed for fMRI, EEG, MEG, PET, and single photon emission computed tomography data analysis. In contrast to SPM, AFNI was developed based on C, Python, R, and shell scripts mainly for the data analysis of the different MRI modalities, including anatomical MRI, functional MRI, and diffusion-weighted imaging. Like AFNI, FSL was conceived for the analysis of the different MRI neuroimaging modalities; however, this one was developed using C++ and shell scripts.

Several straightforward pipelines for adult brains were developed based on the previously mentioned toolkits to automatize, standardize, and simplify the data preprocessing procedure. They allow the easy preprocess of resting-state fMRI data, and their fundamental steps include coregistration, template normalization, distortion correction, segmentation, slice timing correction,

and skull stripping. Furthermore, some of them include tools for performing temporal denoising strategies to control residual physiological signals and motion artifacts (Figure 2.10).

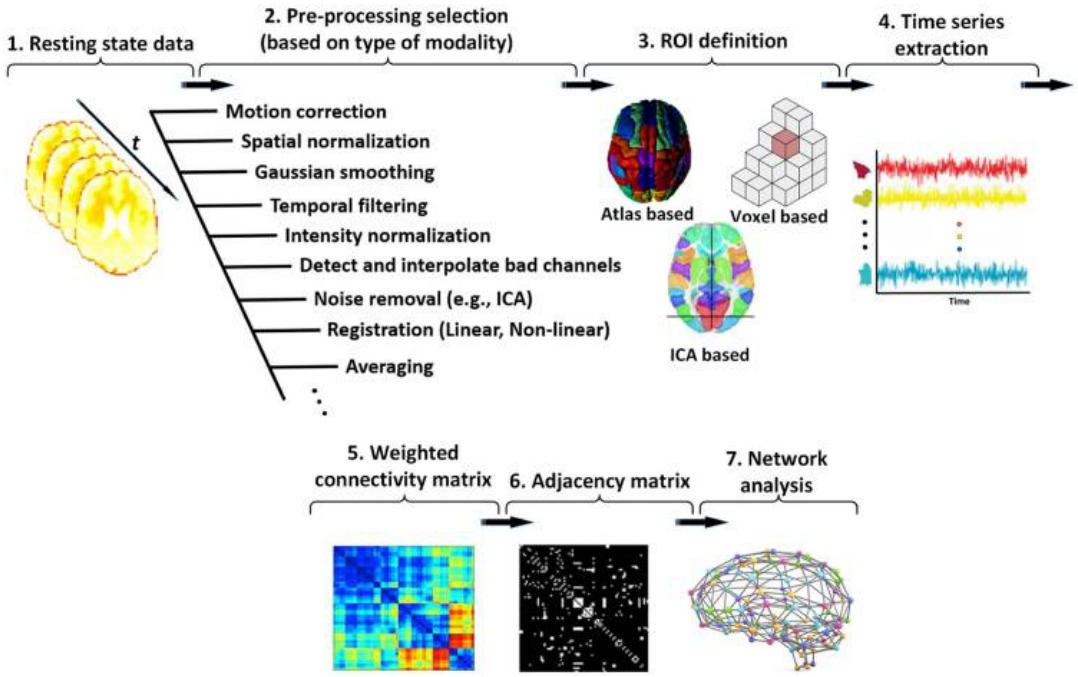

Figure 2.10. Workflow of a basic rs-fMRI pipeline (Mohammadi-Nejad et al., 2018).

Amongst the most used pipelines, we can find the Conn toolbox (CONN) (Whitfield-Gabrieli & Nieto-Castanon, 2012), fmriprep (Esteban et al., 2019), and the Human Connectome Pipeline (HCP) (Glasser et al., 2013). However, to the best of my knowledge, the only existing open-source pipeline to preprocess neonatal rs-fMRI data is the dHCP pipeline which was mainly conceived to preprocess the high-quality data from the dHCP dataset (Fitzgibbon et al., 2020)

2.4.1 Conn toolbox

CONN was developed to compute, display and analyze task-based and resting-state fMRI adult data, and the software is based on Matlab/SPM. Furthermore, it includes quality controls and allows multiple functional connectivity analyses such as Seed-based correlations (SBC), Independent Component Analysis (ICA), and graph theory analysis. Finally, the software includes group-level and population-level inferences.

2.4.2 FMRIPrep

FMRIPrep is a minimal preprocessing pipeline based on a combination of state-of-the-art tools that are all open-source, which includes AFNI, FSL, ANTs (https://stnava.github.io/ANTs/), and FreeSurfer (https://surfer.nmr.mgh.harvard.edu/). Similarly to CONN, fMRIPrep also provides quality control reports for outlier identification; however, fMRIPrep is focused on robust and easy data preprocessing and doesn't provide further denoising steps, data analysis, or statistical tools.

2.4.3 Human Connectome Project Pipeline

The HCP pipelines consist of a combination of tools, mainly shell scripts, to preprocess the high-quality data from the HCP project dataset, making it harder to adapt to different datasets. The structural data preprocessing lies on FreeSurfer and denoising on ICA-FIX. As fMRIPrep, this pipeline doesn't allow for further data analysis and doesn't include statistical tools. Nevertheless, it is the best pipeline for HCP data-related studies as the tools are fully adapted for the dataset and provide a large variety of data quality controls.

2.4.4 Developing Human Connectome Project Pipeline

As the HCP pipeline, the dHCP pipeline has demonstrated outstanding results when preprocessing their datasets; however, its implementation on clinical or smaller datasets remains difficult as large datasets are required for independent components denoising. Moreover, because the dHCP pipeline was specifically developed and optimized for the dHCP database, it can be challenging to set up for cohorts collected at different centers with different tools and parameters. For instance, in the dHCP denoising process, independent correlated signals that can be categorized as neural or non-neural signals are separated using spatial independent component analysis (sICA). When the dimensionality is correctly selected, this denoising technique has been demonstrated to deliver superior outcomes in adults and infants (Alfaro-Almagro et al., 2018; Griffanti et al., 2017). However, classifying the identified signals as structured noise or neural signals is often done manually and is difficult to automate. To address this constraint, the dHCP pipeline uses a machine learning approach (ICA-based Xnoiseifier) (Salimi-Khorshidi et al., 2014) to separate the identified components as neural signals or noise. Thus, to train the machine learning algorithm, at least 35 manually labeled individuals must be used, which requires a specialist and, in most cases, is not achievable in smaller cohorts (Fitzgibbon et al., 2020).

2.5 Data analysis

The approach used for resting-state fMRI data analysis is functional connectivity, which consists of a temporal linear correlation measure between different brain regions (Smitha et al., 2017). We can distinguish seed-based correlations analysis, independent component analysis, and graph theory among the most used functional connectivity approaches.

2.5.1 Seed-based correlations

It was the method adopted by Bharat Biswal for the first resting-state functional connectivity analysis (Biswal et al., 1995). It measures the average time series of a region of interest (ROI) or seed region. The average signal of the ROI is then used to evaluate linear correlation with the other brain voxels. This straightforward method is often employed when one or several pre-defined regions want to be explored with respect to the rest of the brain. It is a hypothesis-driven method and requires previous knowledge for ROI selection. Overall brain connectivity can also be evaluated using this method by performing seed-to-seed connectivity and visualizing the correlation matrix (Figure 2.11). The main advantage of seed-based functional connectivity is its simplicity and ease of interpreting the results. However, its main drawback is that it depends on the seed position, making it vulnerable to bias (Lv et al., 2018).

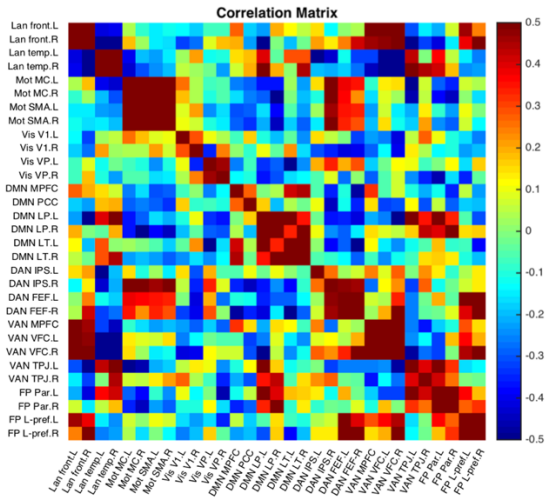

Figure 2.11. Seed-to-seed correlation matrix.

Seed-based functional connectivity maps are computed as the Fisher transformed Pearson correlation coefficients (r) between an ROI/seed average time series and every other voxel of the brain:

$$r(x) = \frac{\int S(x,t)\, R(t)dt}{\sqrt{\int R^2(t)dt \int S^2(x,t)dt}}$$

$$z(x) = tanh^{-1}(r(x))$$

Where S corresponds to the BOLD time series of every voxel, R corresponds to the average BOLD time series of an ROI/seed and r is the functional connectivity map of Pearson correlation coefficients, and z is the Fisher transformed r.

2.5.2 Independent Components Analysis

Similarly to seed-based correlation analysis, the independent components analysis approach allows the study of the correlated brain regions. It uses multivariate decomposition to extract the different resting-state networks from the BOLD signal. To create spatial maps, it decomposes the signal from every brain voxel that is temporally and spatially independent. The independent components analysis is a data-driven approach. It presents the advantage of not needing prior knowledge about the source signal, which makes it ideal for whole-brain blind evaluations (McKeown et al., 1998).

Furthermore, it has a high test-retest reliability (Zuo et al., 2010). However, the number of independent components in which the signal is decomposed has to be defined a priori. This greatly impacts the results, as depending on the number of components, a resting-state network could be broken into sub-networks (Lv et al., 2018). Furthermore, another drawback is that neural signals need to be separated from the noise, which usually has to be done by experience or prior knowledge (Smitha et al., 2017).

2.5.3 Graph theory

Graph theory is employed to construct mathematical models of the whole brain networks for analyzing brain networks topology. The study of these brain networks is based on different edges (connections) and nodes (ROIs) that together create a graph (Figure 2.12).

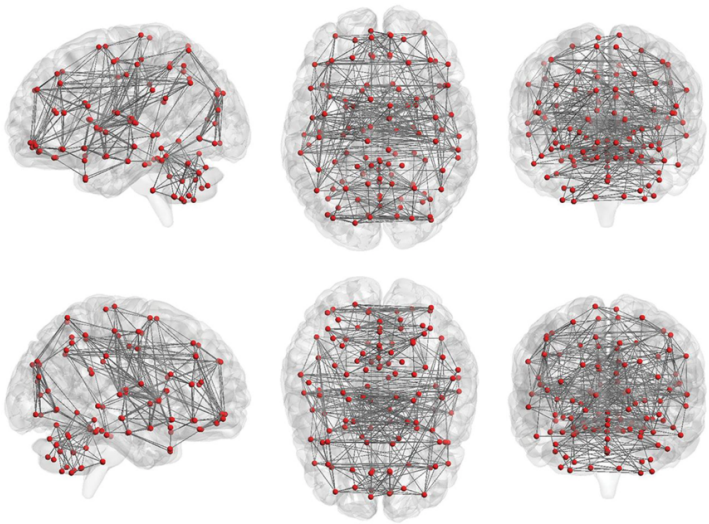

Figure 2.12. Graph analysis based on connections (gray lines) and nodes (red ROIs)(Lv et al., 2018).

In contrast with SBC and ICA, which provide information about the ROI/voxel correlation within the rest of the brain, graph theory allows for the exploration of different functional connectivity metrics that might be complementary to one of the previously cited analysis methods. The most employed metrics of this method are clustering coefficient, path length, degree of a node, and centrality.

- The clustering coefficient represents a measure of local integration and allows characterization of the degree of connection between a node and the neighboring ones.

- The path length is defined as the shortest distance between two nodes. In other words, it is the minimum number of edges traversed to go from one node to another.

- The degree of a node corresponds to that node's total number of connections.

- Centrality represents the number of shortest-path neighbors of a node (Smitha et al., 2017).

The main advantage of graph theory is that it allows the characterization of the whole brain topology; however, the results are not intuitive and may be difficult to interpret (Lv et al., 2018).

In conclusion, today, there is no gold-standard method, and each method can be employed individually or combined based on the type of study that wants to be performed. Seed-based correlation is a hypothesis-driven approach. It is straightforward to use, is simple, and the results are easy to interpret; however, it requires previous knowledge. It is ideal to evaluate functional connectivity when having a previous hypothesis. Independent components analysis is a data-driven approach and doesn't need prior knowledge. However, there is no consensus on the choice of the number of independent components, which may affect the results. It is most of the time employed for global brain exploration. Indeed, Doria et .al in their study about the emergence of resting-state networks in the preterm brain showed that the seed-based correlation and the independent components approach produced similar results for the different evaluated resting-state networks when both applied correctly (Doria et al., 2010). Finally, graph theory can be used alone or to provide complementary information to functional connectivity measures such as topological organization measurements (Achard & Bullmore, 2007; He et al., 2009; Meunier, Achard, Morcom, & Bullmore, 2009; Rubinov & Sporns, 2010).

2.5.4 Measures of correlation

When looking at the resting-state functional connectivity literature, we can observe that the results are presented using different units for the correlation strength. For instance, amongst the most common scores used to show functional connectivity, we find the Pearson correlation, the Fisher transformed correlation, and the standard z-score.

2.5.4.1 Pearson correlation coefficient: r

Pearson correlation is the most basic correlation coefficient from which the following two scores are derived. It is denoted as r and measures the strength of a linear association between two variables. It ranges from -1 to +1, being 0, a value indicating no association between both variables. The Pearson correlation coefficient between two paired variables 'x' and 'y' can be calculated as follows

$$r_{x,y} = \frac{\sum_{i=1}^{n}(x_i - \bar{x})(y_i - \bar{y})}{\sqrt{\sum_{i=1}^{n}(x_i - \bar{x})^2}\sqrt{\sum_{i=1}^{n}(y_i - \bar{y})^2}}$$

Where n is the sample size, x and y are the individual sample points, and $\bar{x}$ and $\bar{y}$ are the samples mean.

An example of a study showing Pearson correlation values is Gao et al. 2015 in Cerebral Cortex (W. Gao et al., 2015). They showed resting-state networks of infants of different ages and adults using a seed-based correlation approach (Figure 2.13).

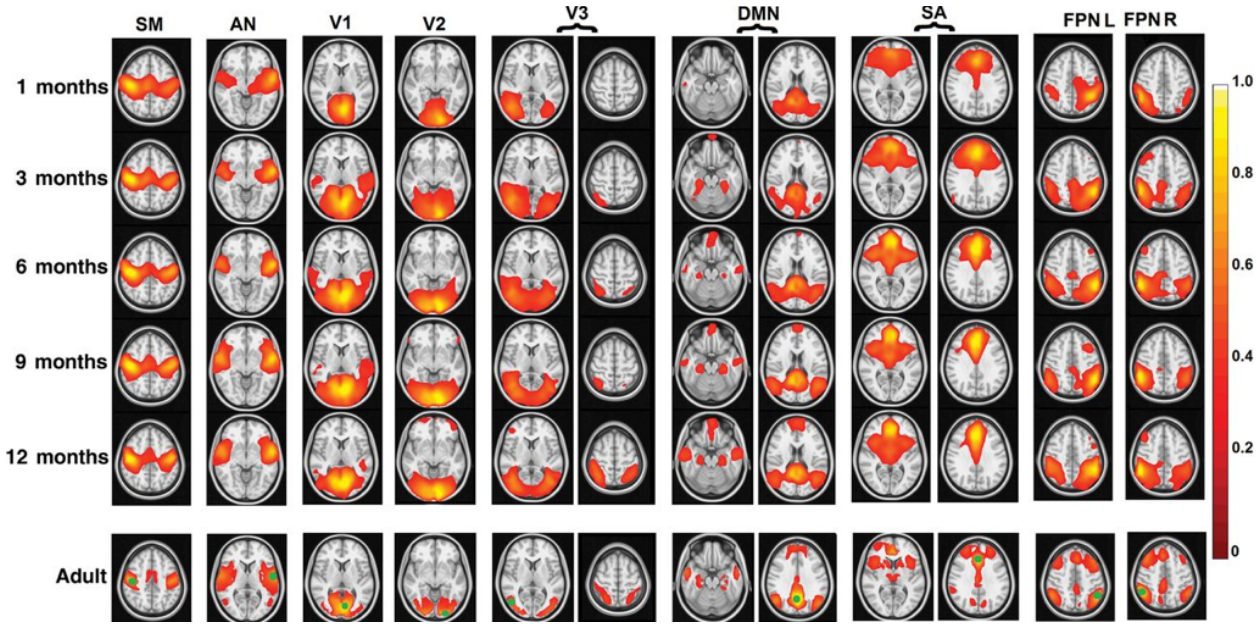

Figure 2.13. Group mean rs-fMRI correlation maps for different resting-state networks. Correlation maps are shown using Pearson correlation values r (W. Gao et al., 2015).

2.5.4.2 Fisher transformed correlation values: z(r)

Fisher transformation is used to perform a hypothesis test about the Pearson correlation coefficient r between two variables.

$$z(x) = \frac{1}{2}\ln\left(\frac{1+r}{1-r}\right) = tanh^{-1}(r(x))$$

This transformation is applied to obtain an approximately normal distribution of the correlation coefficients (Figure 2.14).

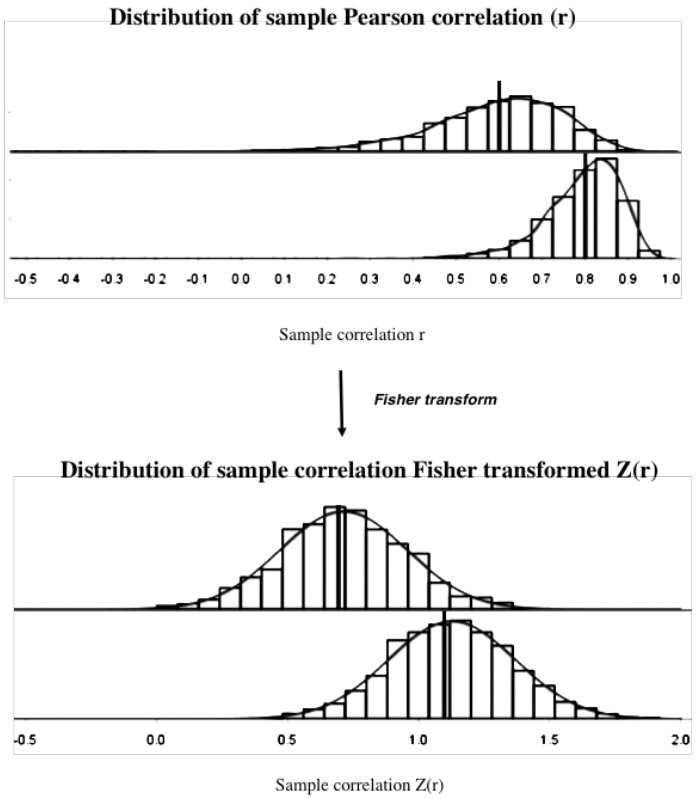

Figure 2.14. Representation of the Fisher transformation.

A study showing z(r) values is Smyser et al. 2016 in Cerebral Cortex (Smyser et al., 2016). They evaluated the effect of prematurity in the neonatal period. Resting-state networks were computed using a seed-based correlation and presented for different ages (Figure 2.15).

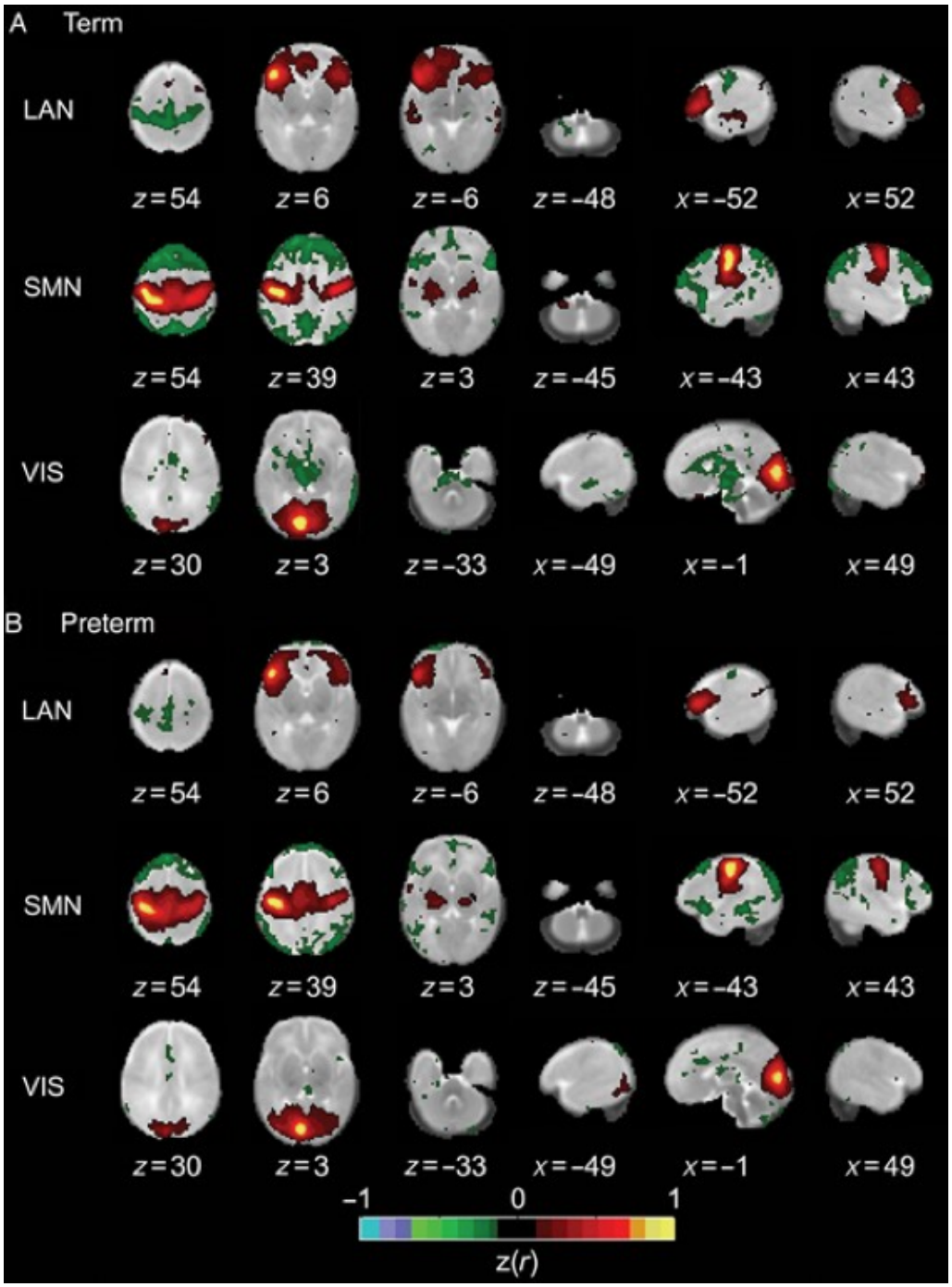

Figure 2.15. Group mean rs-fMRI correlation maps for different resting-state networks at term (A) and preterm (B). Correlation maps are shown using Fisher's z-transformed correlation coefficient z(r). (Smyser et al., 2016).

2.5.4.3 Standard Z-score: Z

Another score to measure functional connectivity is the standard z-score. It tells about the deviation from the mean of the Fisher transformed values.

$$Z = \frac{x - \mu}{\sigma}$$

Where x is z(r), μ is the mean, and σ is the standard deviation.

This is useful to standardize the raw scores of a normal distribution enabling the comparison of two scores from different samples (Figure 2.16). For instance, if a Z-score equals 0, it is on the mean, and a positive Z-score indicates that the score is over the mean. A Z-score of +1 means one standard deviation above the mean.

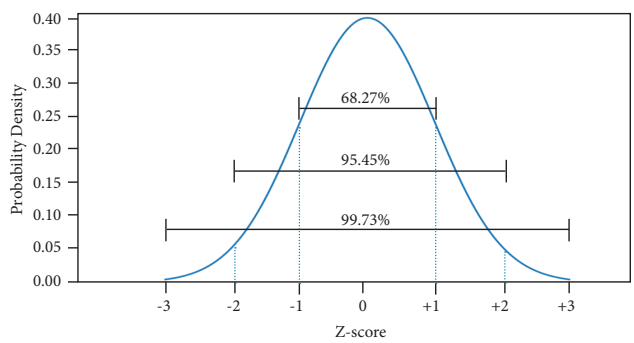

Figure 2.16. Gaussian distribution probability density plot.

Let's assume a 95% confidence level. Its associated p-value is 0.05. In this case, the associated critical Z-scores are -1.96 and +1.96. If the Z-score found is between those values, the p-value is higher than 0.05, and the null hypothesis can't be rejected. On the other hand, if the Z-scores fall outside that range, it is possible to reject the null hypothesis, meaning that the observed results are not likely to arise from random chance.

An example of a study showing standard Z-scores is Fransson et al. 2007 in PNAS (Fransson et al., 2007). Using an independent components analysis approach, they evaluated group resting-state networks in infants born extremely preterm and scanned at term-equivalent age.

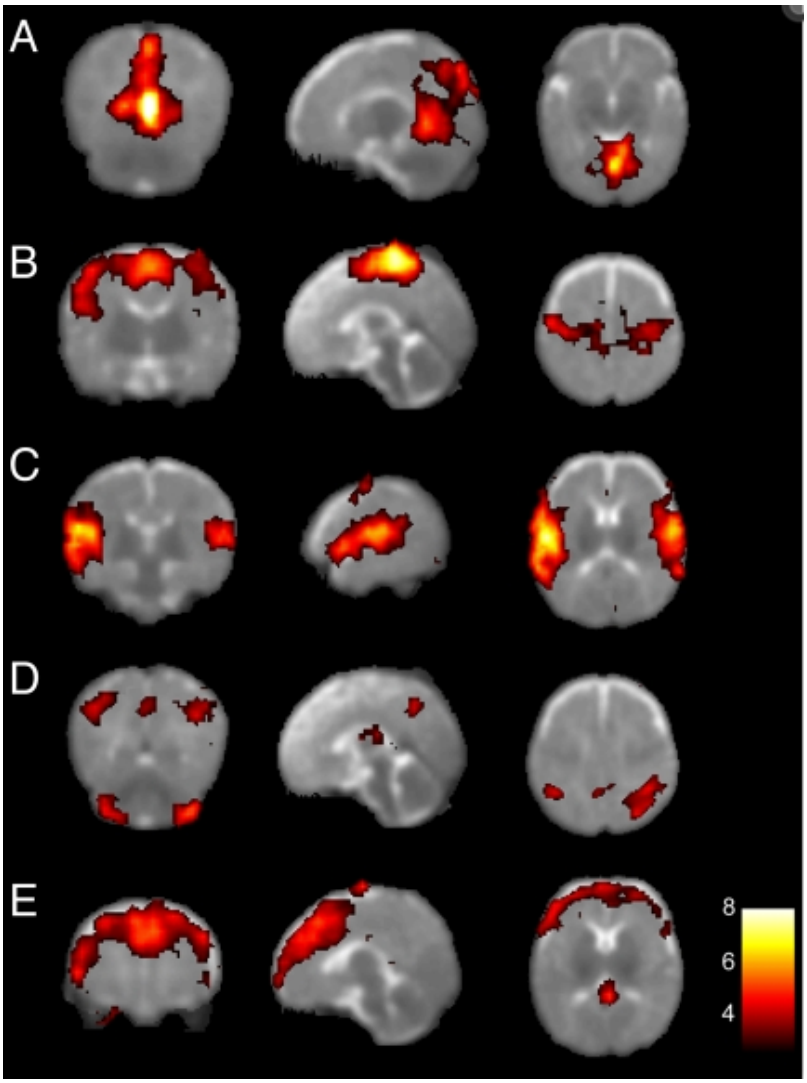

Figure 2.17. Group mean rs-fMRI correlation maps for different resting-state networks in extremely preterm infants scanned at term-equivalent age. (A) Somatosensory and motor, (B) temporal/inferior parietal cortex encompassing the primary auditory cortex (*C*), posterior lateral and midline parts of the parietal cortex as well as the lateral aspects of the cerebellum (*D*), and medial and lateral sections of the anterior prefrontal cortex (*E*). Correlation maps are shown using standard Z-scores (Fransson et al., 2007).

2.5.4.4 Recommendations

Functional connectivity maps of Pearson correlation values or Fisher transformed r values can be used when showing a single subject. However, if multiple subjects' average correlations are studied, then Fisher transformed values are recommended. Using Monte Carlo simulation, Silver

et al. evaluated the behavior of averaging Pearson correlation values versus averaging Fisher's transformed values. They showed that differences in standard errors were negligible when the sample size was 30. However, notable benefits appeared by transforming Pearson correlation coefficients to Fisher's z for smaller sample sizes. For these reasons, it is recommended to use Fisher transformed values for average correlations (Silver & Dunlap, 1987). Finally, if comparisons want to be done between different samples, the most appropriate metric would be the standard Z-score. It allows the translation of individual z(r) values into terms of deviation from the population mean, allowing the comparison of values in different normal distributions.

Three different studies of the same resting-state network, using different measures of correlation, are shown in Figure 2.18 (Ciarrusta et al., 2020; W. Gao et al., 2015; Smyser et al., 2016).

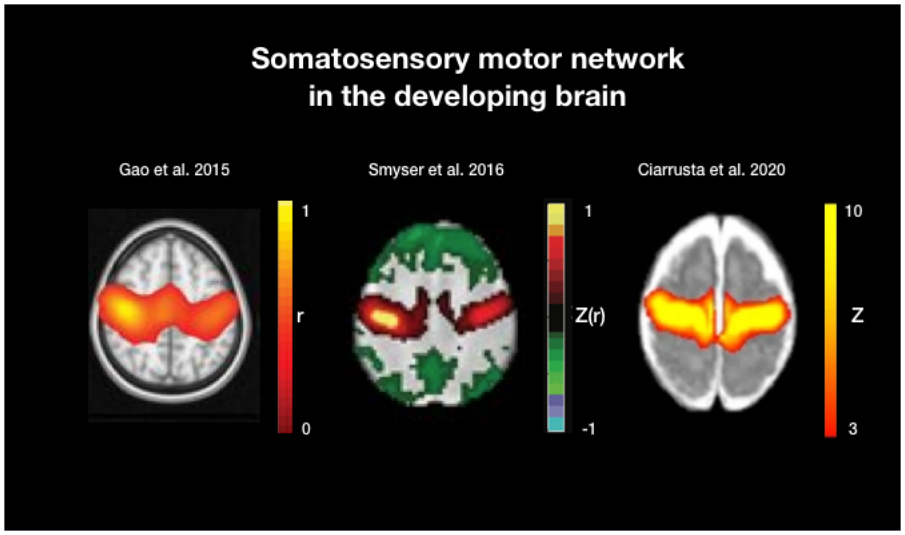

Figure 2.18. Group mean rs-fMRI correlation maps of the somatosensory network.

CHAPTER 3 PROJECT ORGANIZATION

The present work summarizes the research conducted as part of the Ph.D. program in Biomedical Engineering at Polytechnique of Montreal. The research was carried out at the Neuropoly lab under the supervision of Dr. Julien Cohen-Adad (Department of Biomedical Engineering) and at the Research Center of the CHU Sainte-Justine co-supervised by Dr. Gregory Lodygensky (Department of Pediatrics). This project was also done with the collaboration of Dr. Christopher Smyser, Dr. Jeffrey Neil, and Jeanette Kenley from the Washington University School of Medicine, Saint Louis.

Based on the literature review previously presented in Chapter 2, we have seen that different approaches need to be employed when compared to adults to characterize the neonatal resting-state networks. For example, several factors may influence the neonatal acquisition, such as differences in head size depending on age, head motion, or myelination. Also, we observed that no open-source tools are available to preprocess neonatal resting-state fMRI data, which leads to a reduced number of researchers performing neonatal rs-fMRI studies. The issues found in the literature review suggest that new approaches are needed to successfully acquire neonatal rs-fMRI data, such as real-time head motion quality controls and open-source tools to preprocess the acquired data.

3.1 Objectives and impact of the contributions

This project has two main objectives:

O1. Set up a multicenter neonatal resting-state fMRI acquisition protocol adapted to clinical conditions, which include real-time head motion quality control. This will guide every center aiming to perform neonatal rs-fMRI in clinical conditions where acquisition time is minimal, and parameters such as the Specific Absorption Rate (SAR) are crucial.

O2. Provide an open-source tool to preprocess neonatal resting-state fMRI data. This will enable the community to implement a straightforward computational infrastructure and preprocess their data immediately after scanning sessions. As a result, more centers will be able to work together and preprocess their datasets thanks to the democratization of rs-fMRI preprocessing, which will hopefully advance the development of clinical biomarker applications.

3.2 Thesis overview

The thesis is divided into eight different chapters. Chapter 1 includes the context and the facts that motivated the fulfillment of this project, followed by a review of the literature in Chapter 2. The literature review presents the different functional neuroimaging tools and why rs-fMRI was chosen over the other neuroimaging techniques for developing this thesis. The various available tools to preprocess rs-fMRI data, mainly for adults, are presented in the literature review, and the challenges of preprocessing neonatal resting-state functional MRI.

Chapter 3 presents the main objectives and an overview of the thesis.

Chapter 4 consists of a rs-fMRI study performed on young adults that had surgery for congenital heart disease at birth. It describes the methods employed to preprocess and analyze adult rs-fMRI and provides insights into the long-lasting effect of congenital heart disease in resting-state networks.

Chapter 5 presents the specificities and existing challenges of scanning neonates, especially the head motion issue. It includes a real-time head motion quality control approach to ensure that the acquired data has the required quality.

Chapter 6 presents NeoRS, the pipeline developed as a part of this project, to preprocess neonatal rs-fMRI data. It also shows the different methods and tools employed to create this open-source pipeline.

Finally, Chapters 7 and 8 correspond to the general discussion, where the main results are summarized and discussed, and the conclusion.

CHAPTER 4 ARTICLE 1: ALTERED RESTING STATE FUNCTIONAL CONNECTIVITY IN YOUTH WITH CONGENITAL HEART DISEASE OPERATED DURING INFANCY

Authors: V. Enguix[1,2], K. Easson[3,4], G. Gilbert[5], C. Saint-Martin[6], C. Rohlicek[7], D. Luck[1,2], *M. Brossard-Racine[6-9] and *G. A. Lodygensky[1,2].

1. Canadian Neonatal Brain Platform, Canada
2. Department of Pediatrics, CHU Sainte-Justine Research Center, University of Montreal, Canada
3. Advances in Brain & Child Development (ABCD) Research Laboratory, Research Institute of the McGill University Health Centre, Montreal, QC, Canada
4. Department of Neurology & Neurosurgery, Faculty of Medicine, McGill University, Montreal, QC, Canada
5. MR Clinical Science, Philips Healthcare, Markham, ON, Canada
6. Department of Medical Imaging, Division of Pediatric Radiology, Montreal Children's Hospital, Montreal, QC, Canada
7. Department of Pediatrics, Division of Cardiology, Montreal Children's Hospital, Montreal, QC, Canada
8. School of Physical & Occupational Therapy, McGill University, Montreal, QC, Canada
9. Department of Pediatrics, Division of Neonatology, Montreal Children's Hospital, Montreal, QC, Canada.

* shared last authorship

Funding information: This study was collectively funded by the Faculty of Medicine of McGill University and the Research Institute of the McGill University Health Centre and the Montreal Children's Hospital Foundation.

This article has been published in PlosOne, 15 April 2022 (Enguix, Easson, et al., 2022).

4.1 Abstract

Congenital heart disease (CHD) has been associated with structural brain growth impairments and long-term developmental impairments, including deficits in learning, memory, and executive functions. However, it is unclear if early life brain alterations alter the development of the brain's functional connectivity networks in survivors of complex CHD. Therefore, this study aimed to compare resting-state functional connectivity networks associated with executive function deficits between youth (16 to 24 years old) with complex CHD (mean age=20.13; SD=2.35) who underwent open-heart surgery during infancy and age- and sex-matched controls (mean age=20.41; SD=2.05). Using the Behavior Rating Inventory of Executive Function – Adult Version questionnaire, we found that participants with CHD presented with poorer performance on the inhibit, initiate, emotional control, working memory, self-monitor, and organization of materials clinical scales than healthy controls. We then compared the resting-state networks theoretically corresponding to these impaired functions, namely the default mode, dorsal attention, fronto-parietal, fronto-orbital, and amygdalar networks, between the two groups. Participants with CHD presented with decreased functional connectivity between the fronto-orbital cortex and the hippocampal regions and between the amygdala and the frontal pole. Increased functional connectivity was observed within the default mode network, the dorsal attention network, and the fronto-parietal network. Overall, our results suggest that youth with CHD present with disrupted resting-state functional connectivity in widespread networks and regions associated with altered executive functioning, which may be a consequence of early life brain maldevelopment.

Keywords: Congenital heart disease, resting-state functional connectivity, adolescents

4.2 Introduction

Congenital heart disease (CHD) refers to the presence of structural malformation(s) of the heart walls, valves, main blood vessels, and their relationships, resulting in impaired blood flow. With an incidence of 0.85% live births per year in Canada, CHD is the most common neonatal defect (Bernier, Stefanescu, Samoukovic, & Tchervenkov, 2010). The standard of care practice for most complex CHD lesions is to perform open-heart surgery utilizing cardiopulmonary bypass during

infancy, resulting in a significant improvement in life expectancy (Reid et al., 2006). Although these individuals are now expected to live well into adulthood, a large variety of neurodevelopmental impairments are reported during childhood and adolescence. Among these, difficulties with language, social cognition, and higher order cognitive abilities have been widely reported (Easson et al., 2019; Latal et al., 2016; Marelli, Miller, Marino, Jefferson, & Newburger, 2016; Tyagi et al., 2017). Moreover, the emerging literature in older children, adolescents, and adults with CHD converge in reporting specific difficulties with executive functions associated with poorer psychosocial health status and quality of life (Calderon & Bellinger, 2015; Cassidy, White, DeMaso, Newburger, & Bellinger, 2015; Latal et al., 2016; Marelli et al., 2016; Tyagi et al., 2017).

It is now well recognized that CHD impacts brain development during the antenatal and neonatal periods (Brossard-Racine et al., 2016). Magnetic Resonance Imaging (MRI) has contributed to our understanding of cerebral pathophysiological mechanisms in CHD. Indeed, a growing body of quantitative structural MRI studies have reported the presence of regional alterations in brain development in adolescents and young adults with complex CHD (Bolduc, Lambert, Ganeshamoorthy, & Brossard-Racine, 2018). Differences reported include smaller volumes or morphometric variations in the cortical and subcortical grey matter (Fontes et al., 2020; Fontes et al., 2019; Latal et al., 2016; Watson et al., 2016), as well as microstructural alterations predominantly in the association tracts and frontal regions (Easson et al., 2020; Ehrler, Latal, Kretschmar, von Rhein, & O'Gorman Tuura, 2020). Moreover, previous findings have reported associations between regional structural alterations and cognitive functions; however, these relationships were generally small in magnitude (Fontes et al., 2019; Latal et al., 2016; von Rhein et al., 2014).

When examining brain functional connectivity in CHD, results are scarce. Resting-state functional MRI (rs-fMRI) is a neuroimaging technique that evaluates regional brain interactions occurring while the participant is at rest (i.e., not performing any task). This technique allows the investigation of resting-state networks, which provide information about inherent brain function during normal development or following injury. Resting-state networks are described as low frequency fluctuations (<0.1 Hz) in the blood-oxygen-level-dependent (BOLD) signal that can be reproducible across subjects (Lee et al., 2013). Since the discovery of resting-state networks, rs-fMRI studies have provided new insights into the understanding of typical and atypical brain

functioning at rest when studying various pediatric and adult brain pathologies, including autism spectrum disorder, schizophrenia, and Alzheimer's disease (Figueroa et al., 2017; Hojjati, Ebrahimzadeh, & Babajani-Feremi, 2019; Wang et al., 2019). To the best of our knowledge, only one study to date has examined functional connectivity using rs-fMRI in individuals with CHD. The authors reported that neonates with complex CHD, prior to open-heart surgery, presented with preserved global functional network organization, but altered regional functional connectivity, when compared to healthy controls (De Asis-Cruz, Donofrio, Vezina, & Limperopoulos, 2018). More precisely, altered functional connectivity was found in subcortical regions, including the putamen, caudate nucleus, globus pallidus, and thalamus, and in various cortical regions, especially in frontal, parietal, and temporal areas. Although this first study provides valuable insight into functional network topology and regional functional connectivity, it remains unknown if these functional connectivity deficits remain present beyond the post-surgical period. Moreover, whether these connectivity alterations are associated with later-developing cognitive functions remains to be determined. The current study aimed to fill these gaps. To do so, we sought to compare functional connectivity between youth with complex CHD who had undergone open-heart surgery during infancy and healthy peers, targeting networks associated with at-risk executive functions. We hypothesized that youth with complex CHD would exhibit altered functional connectivity in networks associated with executive functioning. As a secondary objective, we also explored the direct relationships between functional network connectivity and altered executive functions. A better understanding of the neural correlates of cognitive difficulties in youth with complex CHD will provide insight into the development and implications of the disease.

4.3 Materials and methods

4.3.1 Participants

French- and English-speaking youth aged 16 to 24 years old born with complex CHD who underwent open-heart surgery (OHS) using cardiopulmonary bypass during the first year after birth were enrolled in this study. Participants born preterm (<37 weeks of gestation), with documented congenital infection, a known chromosomal or genetic abnormality, or multiorgan dysmorphic features were excluded. Participants with CHD were recruited from the pediatric and the adult

cardiology units of the McGill University Health Center (MUHC) as previously reported (Fontes et al., 2019).

A control group, matched for age and sex, was recruited from local colleges, universities, and the community through advertisements and word of mouth. Controls were considered healthy if they had no history of brain tumor or malformation, traumatic brain injury, developmental or neurologic conditions and had not received rehabilitation or special education services during childhood or adolescence. Written informed consent was obtained from the participant, or legal guardians when younger than 18 years old. The study was approved by the MUHC Pediatric Research Ethics Board.

4.3.2 Individual and clinical variables

All the participants underwent a single study visit at the Montreal Children's Hospital to complete a brain MRI. Height and weight were measured before the MRI to compute body mass index (BMI). Socioeconomic status (SES) was measured using the Hollingshead Four-Factor Index questionnaire (Hollingshead, 1975) and relevant clinical information, such as cardiac diagnosis, age at first surgery, and number of open-heart surgeries, was extracted from the medical records of the CHD participants.

4.3.3 Executive function and self-regulation

On the day of the MRI, participants completed the Behavior Rating Inventory of Executive Function – Adult Scale (BRIEF-A) a norm-referenced, self-reported questionnaire that evaluates executive function and self-regulation (Rouel, Raman, Hay, & Smith, 2016). This test is composed of nine clinical scales: inhibit, shift, emotional control, self-monitor, initiate, working memory, plan/organize, task monitor, and organization of materials, which together provide a total score for metacognition and behavioral regulation. On the BRIEF-A, higher scores represent poorer executive functioning.

4.3.4 MRI data acquisition

Participants underwent a single brain MRI on a 3.0 T MRI (Achieva X-series, Philips Healthcare) using a 32-channel head coil. The acquisition protocol included three-dimensional 1 mm isotropic T1-weighted images (TE = 3.7 ms, TR = 8.1 ms, TI = 1010 ms, pixel bandwidth = 191.4 Hz/pixel, FOV = 240x240 mm, slice thickness =1 mm, flip angle = 8º) and a gradient-echo echo planar

imaging (EPI) sequence (TE =30 ms, TR=2600ms, pixel bandwidth = 2197.48 Hz/pixel, FOV=240x240 mm, acquisition matrix=80x80, slice thickness = 3 mm, flip angle = 70º, 47 slices/volume, interleaved, no gap). During the resting-state sequence, participants were awake and instructed to keep their eyes closed. The anatomical images were reviewed for overt brain anomalies by an experienced neuroradiologist, who was blinded to the clinical history of the participants.

4.3.5 MRI data processing

Before pre-processing, T1-weighted and EPI images were visually inspected for possible artifacts (e.g., spikes, signal loss, aliasing). Spatial pre-processing of images was first performed and included the following steps: functional cross-realignment for head motion correction, slice timing correction, outlier scrubbing (Power, Barnes, Snyder, Schlaggar, & Petersen, 2012), normalization to Montreal Neurological Institute (MNI) 152 space, and outlier detection using the Artifact Detection Tool (ART) (www.nitrc.org/projects/artifact_detect). Afterwards, data were spatially smoothed with an 8 mm full-width half-maximum gaussian kernel (Motoyama et al., 2019).

We used a gaussian kernel of 2-3 times the voxel size, as this has been shown to be optimal to correct for truncation artifacts (Lindquist & Wager, 2008), to increase signal-to-noise ratio, and to reduce the influence of residual variability and gyral anatomy across subjects. After spatial pre-processing, realigned images in MNI space were visually inspected by overlapping the MNI structures over structural and functional data to confirm optimal realignment.

The BOLD signal of interest may be altered by macrovessel signal, mainly those located in the pial surface, as well as by some non-physiological signals, such as head motion. To correct for these nuisance variables, temporal processing was performed using a component-based noise correction method (Behzadi, Restom, Liau, & Liu, 2007; Friston, Williams, Howard, Frackowiak, & Turner, 1996; Power et al., 2014). From the T1-weighted images, white matter and cerebrospinal fluid were segmented using SPM12 (www.fil.ion.ucl.ac.uk/spm) and used in a subsequent step to remove the temporal confounding factors. Nuisance variables were based on cerebrospinal fluid signal, white matter signal, motion, and realignment parameters (Friston et al., 1996). Potential outliers were identified from subject motion and observed global BOLD signal using ART. Volumes with framewise displacement higher than 0.5 mm and/or that presented global signal changes above 3 standard deviations were identified as outliers. The anatomical CompCor method was used for

nuisance correction (Behzadi et al., 2007; Muschelli et al., 2014), as it has been shown to be as efficient as global signal regression-based methods, but without inducing undue anti-correlations (Behzadi et al., 2007; Murphy, Birn, Handwerker, Jones, & Bandettini, 2009). Functional data were linearly detrended and band-pass filtered [0.008 – 0.09Hz] to adjust for low frequency fluctuations related to very slow head displacements, scanner-related drifts, and high frequency noise effects (Alonazi et al., 2019; Tomiyama et al., 2019; Wehrle et al., 2018; Whitfield-Gabrieli & Nieto-Castanon, 2012).

A quality control plot was created to detect outliers after denoising, consisting of a voxel-to-voxel correlation histogram. Before denoising, functional connectivity distribution values within the whole brain showed highly positively skewed distributions and appeared to be very different across subjects due to the influence of large-scale physiological signals and head motion effects. After having corrected for the aforementioned confounders, functional connectivity distributions appeared to be well centered and very similar across subjects, suggesting that the noise effect had been appropriately removed (see Appendix A - Figure A. 1). To achieve the desired denoising data quality, we employed for every subject: white matter (5 components), cerebrospinal fluid (5 components), scrubbing (one per identified outlier volume), motion (6 components + 1st order derivatives). After this step, as the degrees of freedom of every participant were still high, we decided to include the quadratic effects to the realignment component to improve motion related denoising. Finally, we used the number of degrees of freedom remaining after the denoising process as an exclusion factor, excluding subjects with less than 15 degrees of freedom. All the participants presented with centered and normalized data and enough degrees of freedom to be analyzed.

To process and analyze the resting-state fMRI data, we used the CONN Toolbox 18.b (http://nitrc.org/projects/conn), based on SPM12 and running in MATLAB R2018a (MathWorks, Inc, Natick, MA, USA) on an Ubuntu 18.04 machine.

4.3.6 Seed selection

Seed-based functional connectivity (SBC) analysis was performed to identify differences in brain functional connectivity between the CHD and control groups. Considering the increasingly recognized functional challenges reported in adolescents and young adults with CHD, we chose to use a hypothesis-driven approach over a data-driven approach to compare functional connectivity in networks related to executive function as identified by the BRIEF-A. Seeds for each region and

network were placed using the probabilistic Harvard-Oxford atlas (http://neuro.debian.net/pkgs/fsl-harvard-oxford-atlases.html). The selected seeds corresponded to brain regions or networks known to be involved in executive functions that were found to be significantly different in our group comparisons of the BRIEF-A clinical scales. In line with these findings, we analyzed the default mode network (internal modes of cognition) (Davey, Pujol, & Harrison, 2016), the dorsal attention network (attentional capabilities) (Rohr et al., 2017), the fronto-parietal (Figueroa-Vargas et al., 2020) and fronto-orbital networks (high-level cognition function) (Barbey, Koenigs, & Grafman, 2011; Ross, LoPresti, Schon, & Stern, 2013), and the amygdalar network (emotional control) (Frank et al., 2014; LeDoux, 2007). To assess the different networks, seeds were placed as specified in the Conn toolbox (Whitfield-Gabrieli & Nieto-Castanon, 2012). The medial prefrontal cortex (mPFC) and the posterior cingulate cortex (PCC) were chosen to assess the default mode network (DMN), the intra-parietal sulcus (IPS) and the frontal eye fields (FEF) to assess the dorsal attention network (DAN), and the lateral prefrontal cortex (LPFC) and the parietal cortex (PPC) to assess the fronto-parietal network (FPN). The fronto-orbital network was added to the analyses given its link with executive functions and the amygdalar network was added for playing an important role in emotional control, with seeds placed in the fronto-orbital cortex and in the amygdala, respectively.

4.3.7 Statistical analysis

4.3.7.1 Participants' characteristics and BRIEF-A scores

Participants' characteristics were compared between the CHD and control groups using independent sample t-tests or chi-square tests, as appropriate. Variables that showed significant group differences were considered potential confounders and included in subsequent analyses. Analyses of covariance (ANCOVA) were performed for each clinical scale of the BRIEF-A, using potential confounders as covariates when relevant. The only significantly different confounder between the CHD and control groups was socioeconomic status, which was included as a covariate in subsequent analyses. In all analyses, the alpha level was set at 0.05.

4.3.7.2 Resting-state functional connectivity

The average time series of each single seed was computed across each seed region in each participant, and then correlated with the time series of every other voxel in the brain. Correlation

maps were calculated using the standard Pearson product-moment formula as described in Biswal et al. (Biswal et al., 1995). Correlation coefficients were normalized by Fisher's z-transformation.

Group differences in functional connectivity between CHD and controls were assessed using ANCOVA, using socioeconomic status as a covariate. Statistical significance between groups was established as $p < 0.001$ (uncorrected) at the voxel level and as $p < 0.05$ (corrected for family wise error [FWE]) at the cluster level (W. Liu, Hu, An, Zhou, & Gong, 2019; L. Zhang et al., 2020).

Additionally, to explore the direct associations between network functional connectivity and executive function deficits, we performed two-tailed Pearson correlations between functional connectivity and BRIEF-A scores, focusing on the BRIEF-A scales previously identified to be significantly different between the two groups. These correlation analyses were performed separately in the control and CHD groups. The level of statistical significance as set at $p < 0.05$. We did not correct for multiple comparisons considering the exploratory nature of these analyses.

4.4 Results

4.4.1 Participants' characteristics

In total, we collected 43 rs-fMRI acquisitions in the CHD group and 47 in the control group. Of these, five participants from the CHD group and two from the control group were excluded from the analysis for not having a complete rs-fMRI acquisition. Another CHD participant was excluded from the analysis for not passing the aforementioned quality assessment. Our final sample for analysis consisted of 37 participants with CHD (14/37 male) and 45 controls (19/45 male). Of the 37 participants with CHD, 32 (86.49%) presented with a two-ventricular cardiac physiology: dextro-transposition of the great arteries (n = 13), Tetralogy of Fallot (n = 10), total anomalous pulmonary venous connection (n = 2), ventricular and atrial septal defects (n = 5), and truncus arteriosus type I (n = 2). Only 5/37 (13.51%) presented with a univentricular physiology: double outlet right ventricle (n = 1), pulmonary atresia (n = 3), and hypoplastic left heart syndrome (n = 1). CHD participants had between one and four open-heart surgeries (median 1) at the time of the study visit. Mean age at first surgery was 68.65 days old, with a range from zero to 293 days after birth. Socioeconomic status was found to be significantly higher in the control group when compared to the CHD group and was consequently included as a covariate in subsequent analyses. No other significant group differences were found for age at MRI, sex, and BMI (Table 4.1).

Table 4.1 Participants' characteristics.

Variables; mean [SEM], N (%)	**CHD (n=37)**	**CTL (n=45)**	**p-value**
Age at MRI, years	20.13 [0.38]	20.41 [0.30]	0.34
Age first surgery, days	68.65 [15.51]	-	-
Sex			0.80
Male	14 (37.8%)	19 (42.2%)	
Female	23 (62.2%)	26 (57.8%)	
Body mass index	23.31 [0.67]	23.92 [0.56]	0.23
Socioeconomic status	39.95 [2.07]	50.73 [1.54]	<0.001
Type of CHD			
Single ventricle	5/37 (13.5%)	-	-
Tetralogy of Fallot	10/37 (27.0%)	-	-
Transposition of great arteries	13/37 (35.1%)	-	-
Other two-ventricle physiology			
Ventricular/atrial septal defects	5/37(13.5%)	-	-
Truncus arteriosus type I	2/37(5.4%)	-	-
Total anomalous pulmonary	2/37(5.4%)	-	-
venous connection	134.5 [8.57]	-	-

Total surgery time (min)			
Aortic cross clamp time (min)	76.59 [6.09]	-	-
Deep hypothermia time (min)	19.28 [4.06]	-	-
Catheterizations	22/32 (68.75%)	-	-
Balloon atrial septostomy before surgery	8/15 (53.33%)	-	-

Legend: CHD: congenital heart disease, CTL: control, SEM: standard error of the mean.

Brain anomalies on conventional MRI likely from an acquired origin were detected in 7/37 (18.92%) CHD participants and 4/45 (8.89%) of the controls, which was not statistically different (p=0.210) These anomalies included: One CHD participant with cystic dilation of the perivascular spaces; two CHD participants with periventricular white matter injury; two CHD participants and three controls with susceptibility artifact, likely representing blood deposition or calcification; and two CHD participants and one control with asymmetrical ventricles. Brain anomalies likely from a developmental origin were found in 6/37 (16.22%) CHD participants and 2/45 (4.44%) controls, (p=0.123). These anomalies included: Three CHD participants and one control with gray matter heterotopia; two CHD participants and two controls with developmental venous anomalies; one CHD participant with cortical developmental anomaly; and one CHD participant with Chiari I malformation. The observed anomalies were all considered to be mild and from a remote origin, and none of the brain anomalies detected on conventional MRI overlapped with any of the connectivity networks analyzed.

4.4.2 Executive functions

After controlling for SES, participants with CHD demonstrated significantly poorer performance than control participants on the inhibit ($F(1,76) = 7.16$; $p = 0.009$), emotional control ($F(1,76) = 7.24$; $p = 0.009$), self-monitor ($F(1,76) = 7.09$; $p = 0.009$), initiate ($F(1,76) = 4.22$; $p = 0.04$), working memory ($F(1,76) = 5.25$; $p = 0.025$), and organization of materials ($F(1,76) = 18.51$; $p<0.001$) clinical scales of the BRIEF-A. By contrast, there were no significant differences between

groups for the shift ($F(1,76) = 1.21$; $p = 0.27$), plan/organize ($F(1,76) = 3.40$; $p = 0.07$), and task monitor ($F(1,76)=3.53$; $p=0.06$) clinical scales. Scores for BRIEF-A scales are summarized in Table 4.2. Participants were classified as having a clinically significant deficit on a given clinical scale when having a score ≥ 65. On average, a greater percentage of participants with CHD had clinically significant executive function deficits as compared to controls (6 – 40% in CHD vs. 0 – 13.6% in controls) across the different clinical scales. Differences in the prevalence of clinically significant deficits were statistically significant for the inhibit ($\chi^2 = 14.23$; $p < 0.001$), working memory ($\chi^2 = 7.1$; $p = 0.008$), and organization of materials ($\chi^2 = 11.09$; $p < 0.001$) clinical scales (see Appendix A - Table A. 1).

Table 4.2 BRIEF-A scales results

Mean (SEM)	**CHD (n=35)**	**CTL (n=44)**	**p-value**
Inhibit**	55.6 (2.21)	50.4 (2.04)	0.009
Shift	53.6 (2.15)	51.5 (2.41)	0.27
Emotional control**	56.9 (1.93)	49.5 (2.57)	0.009
Self-monitor**	54.1 (2.28)	46.5 (2.19)	0.009
Initiate*	54.9(1.80)	51.2 (2.42)	0.04
Working memory*	59.1 (2.11)	53.0 (2.34)	0.02
Plan/ Organize	53.5 (1.62)	50.5 (1.93)	0.07
Task monitor	57.0 (2.02)	52.8(2.86)	0.06
Organization of materials***	55.2 (2.19)	46.6 (2.76)	<0.001

Legend: * $p < 0.05$; ** $p < 0.01$; ***$p < 0.001$. NB: Higher scores of BRIEF-A indicate poorer performance.

4.4.3 Resting-state Functional Connectivity

We performed comparisons of seed-based functional connectivity between the two groups for the default mode, dorsal attention, fronto-parietal, fronto-orbital, and amygdalar networks. For each analysis, the threshold of statistical significance as set to $p < 0.001$ (uncorrected) at the voxel level and $p < 0.05$ (corrected for family wise error [FWE]) at the cluster level. Voxels that did not survive the threshold were not displayed.

4.4.3.1 Decreased functional connectivity

Fronto-orbital network: Our analyses revealed lower inter-network functional connectivity in the CHD group when compared to controls between the right fronto-orbital cortex and the left hippocampus and between the left fronto-orbital cortex and bilateral (Figure 4.1, Table 4.3).

Amygdalar network: We found significantly lower inter-network functional connectivity in the CHD group compared to controls between the left amygdala and the right frontal pole and between the left amygdala and the right cingulate and paracingulate gyrus (Figure 4.1, Table 4.3).

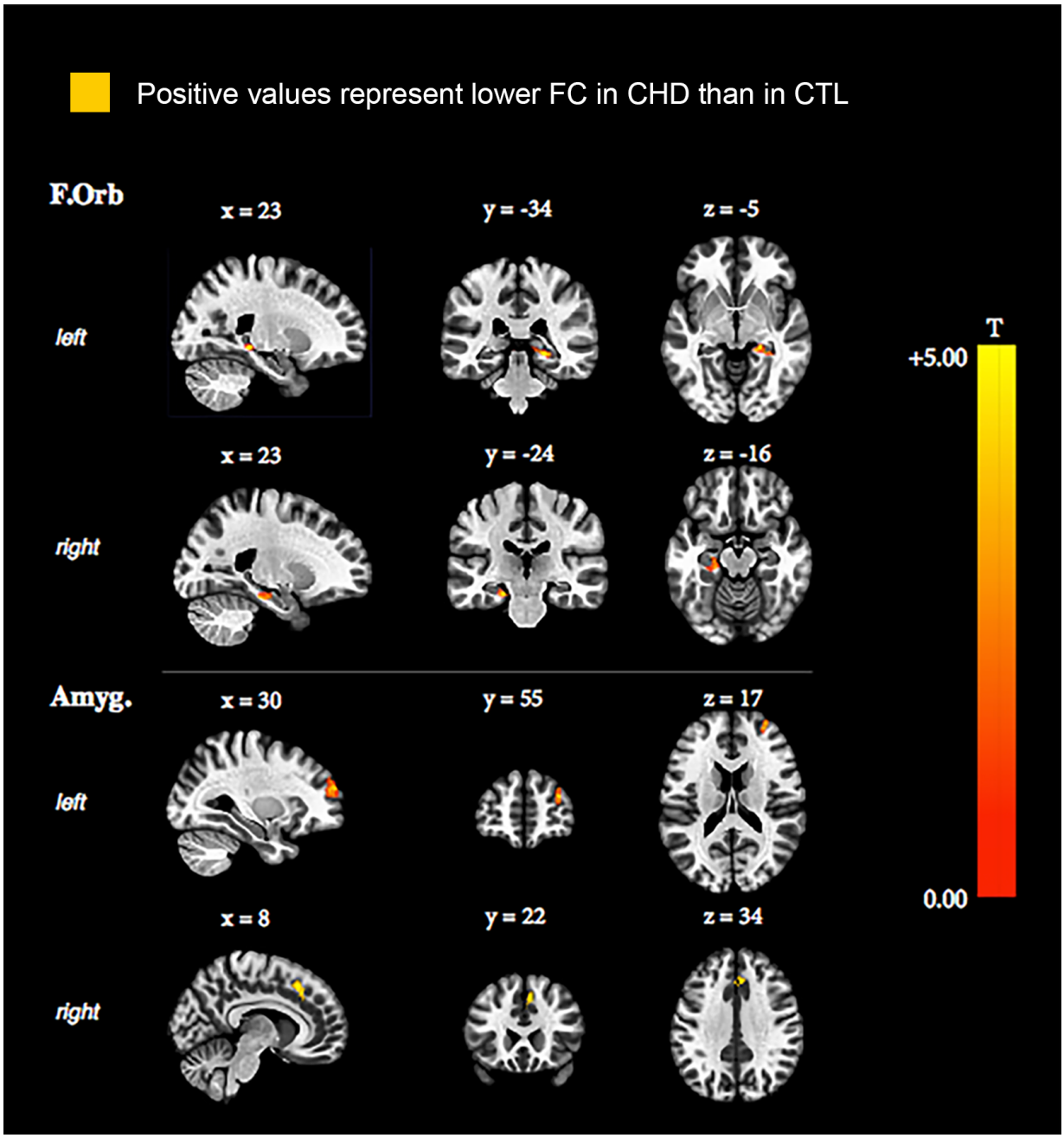

Figure 4.1 Functional connectivity differences between CHD and control groups where CHD presented lower functional connectivity.

Legend: CHD: congenital heart disease, CTL: controls, F.Orb: fronto-orbital network, Amyg: amygdalar network.

Table 4.3 Functional connectivity differences between CHD and control groups where CHD participants presented with lower functional connectivity than controls.

	Affected region	**Cluster size**	**Peak p-uncorrected**	**Cluster p<FWE**
CHD lower FC than CTL				
F.Orb (right cortex)	Left hippocampus	113	<0.001	0.03
F.Orb (left cortex)	Right and left hippocampus	185	<0.001	<0.01
Amyg (left amygdala)	Frontal pole right	270	<0.001	<0.001
Amyg (left amygdala)	Cingulate and paracingulate gyrus right	134	<0.001	0.01

Legend: FC: functional connectivity, CHD: congenital heart disease, CTL: controls, F.Orb: fronto-orbital network, Amyg: amygdalar network.

4.4.3.2 Increased functional connectivity

Default mode network: When compared to controls, participants with CHD presented with higher intra-network functional connectivity between the medial prefrontal cortex and the posterior cingulate cortex (Figure 4.2, Table 4.4).

Dorsal attention network: Similar to the DMN, our analyses showed significantly higher inter-network functional connectivity in participants with CHD when compared to controls between the left intraparietal sulcus (ips_l) and the bilateral hippocampal and parahippocampal regions, but also between the right intraparietal sulcus (ips_r) and the right hippocampal and parahippocampal regions (Figure 4.2, Table 4.4). No significant differences were found for the frontal eye fields.

Fronto-parietal network: We observed significantly higher inter-network functional connectivity in the CHD group when compared to controls between the left parietal cortex (ppc_l) and the left caudate, left accumbens, and left putamen, and between the ppc_l and the right crus of the

cerebellum (Figure 4.2, Table 4.4). No significant differences were found for the lateral prefrontal cortex.

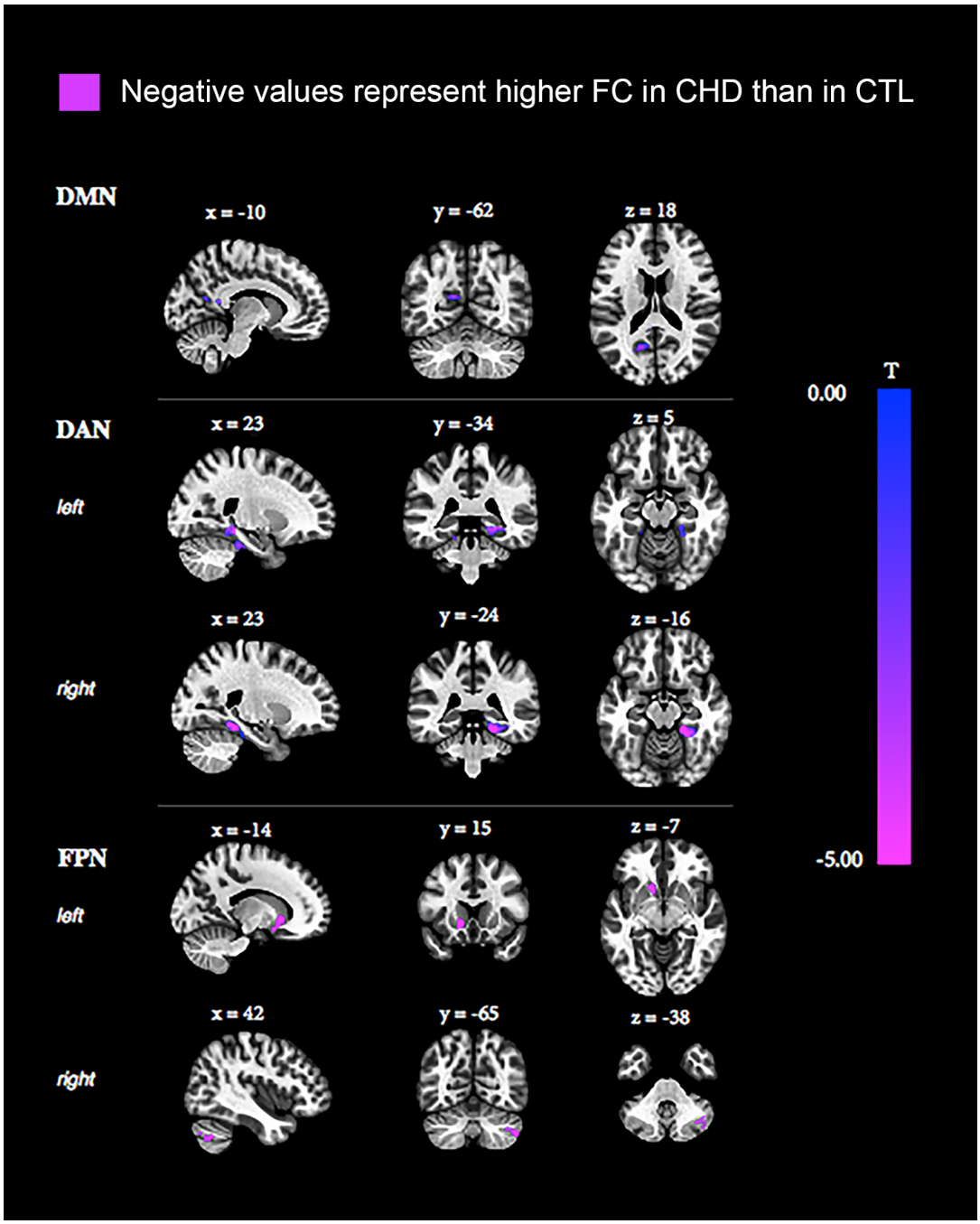

Figure 4.2 Functional connectivity differences between CHD and control groups where CHD participants presented with higher functional connectivity than controls.

Legend: CHD: congenital heart disease, CTL: controls, DMN: default mode network, DAN: dorsal attention network, FPN: fronto-parietal network.

Table 4.4 Functional connectivity differences between CHD and control groups where CHD participants presented with higher functional connectivity than controls.

	Affected region	**Cluster size**	**Peak p-uncorrected**	**Cluster p<FWE**
CHD higher FC than CTL				
DMN (medial prefrontal cortex)	Posterior cingulate cortex	133	<0.001	0.018
DAN (intraparietal sulcus left)	Right hippocampal and parahippocampal regions	405	<0.001	<0.001
DAN (intraparietal sulcus left)	Left hippocampal and parahippocampal regions	263	<0.001	<0.001
DAN (intraparietal sulcus right)	Right hippocampal and parahippocampal regions	348	<0.001	<0.001
FP (parietal cortex left)	Left caudate, left accumbens and left putamen	161	<0.001	0.01
FP (parietal cortex left)	Cerebellum Crus 1-2 right	151	<0.001	0.01

Legend: FC: functional connectivity, CHD: congenital heart disease, CTL: controls, DMN: default mode network; DAN: dorsal attention network; FPN: fronto-parietal network.

4.4.4 Correlations between functional connectivity and BRIEF-A scores

We observed two different sets of significant correlations between functional connectivity and BRIEF-A scores in the CHD participants and in the control participants. In the CHD group, significant correlations were found between right frontal orbital – left hippocampus functional connectivity and the inhibit scale ($r = -0.36$, $p = 0.03$), as well as between medial prefrontal cortex – posterior cingulate functional connectivity and the organization of materials scale ($r = 0.35$, $p =$

0.038). In the control group, significant correlations were observed between left intraparietal sulcus – right hippocampus functional connectivity and the emotional control scale ($r = 0.36$, $p = 0.014$), as well as between left amygdala – cingulate/paracingulate gyrus functional connectivity and the organization of materials scale ($r = -0.35$, $p = 0.019$).

4.5 Discussion

The present study investigated cerebral functional connectivity in brain networks associated with executive functioning in youth born with complex CHD who had undergone open-heart surgery using cardiopulmonary bypass during infancy. Our evaluation of function-specific resting-state networks revealed statistically significant differences in functional connectivity in youth born with complex CHD, when compared to healthy peers, with significant alterations of functional connectivity within the fronto-orbital cortex, amygdala, default mode, dorsal attention, and fronto-parietal networks.

To the best of our knowledge, this is the first resting-state functional connectivity study on post-operative CHD patients. The only other previous study of resting-state functional connectivity in this population was performed in neonates with complex CHD prior to open-heart surgery (De Asis-Cruz et al., 2018). This prior study reported that pre-operative CHD neonates exhibited reduced rich club network organization in functional brain network connectivity when compared to healthy term-born neonates, as well as reduced sub-network connectivity, predominantly implicating the subcortical areas, such as the caudate, putamen, and thalamus, and their connections to the contralateral frontal, parietal, and temporal cortices. They also reported reduced functional connectivity within the hippocampus and other brain structures, in line with our current findings. Indeed, we found decreased functional connectivity in youth with CHD between the fronto-orbital network and the hippocampus. Taken together, these observations may suggest that alterations in hippocampal functional connectivity that are present prior to open-heart surgery likely persist during development and after cerebral hemodynamics have been restored following cardiac surgery. Our results also converge with previous findings from anatomical studies that have demonstrated smaller hippocampal volumes and morphometric differences in adolescents and young adults with CHD, associated with poorer memory and executive functioning (Fontes et al., 2019; Latal et al., 2016). Future fMRI studies using the hippocampal structural input as a seed in

network analysis could clarify the relationship between the structural alterations and functional connectivity alterations reported in youth with CHD.

Participants with complex CHD in our study also presented with decreased functional connectivity between the amygdala and frontal and cingulate regions. The amygdala's interaction with the frontal cortex plays a crucial role in the regulation of emotion (Banks, Eddy, Angstadt, Nathan, & Phan, 2007), known to be vulnerable in CHD survivors and found to be significantly different from controls on the associated BRIEF-A clinical scale. Elevated rates of anxiety disorders, attention deficit hyperactivity disorder, and depression have been reported in adolescents and adults with complex CHD (DeMaso et al., 2017; Pike et al., 2018), which could theoretically be related to amygdala dysfunction. In adolescents with major depressive disorders, studies have previously shown decreased amygdala functional connectivity (Cullen et al., 2014; Tang et al., 2018). A recent study reported that adults with complex CHD are more likely than controls to present with some personality traits, in particular neuroticism (i.e., experiencing emotional negativity and instability) (Skoczek et al., 2019). However, whether these psychiatric symptoms are present in youth with CHD and are related to altered functional amygdalar connectivity will need to be further investigated, considering that we did not specifically evaluate mental health.

An unexpected finding was the observation of increased functional connectivity of the DMN in participants with CHD when compared to controls. The DMN has been extensively studied in the healthy populations and in various psychiatric, neurological, and neurodevelopmental conditions (Bauml et al., 2019; Davey et al., 2016; Gardini et al., 2015; Sheline et al., 2009; L. Zhang et al., 2020). While decreased functional connectivity within the DMN has been widely reported in pathologies such as autism spectrum disorder, schizophrenia, and Alzheimer's disease (Buckner, Andrews-Hanna, & Schacter, 2008), an increased functional connectivity between the mPFC and the PCC has been demonstrated in patients with mild cognitive impairment (Gardini et al., 2015). This is particularly of interest considering that there is emerging literature suggesting that seniors living with CHD are at greater risk of early onset dementia (Bagge et al., 2018; Keir et al., 2019). Moreover, the DMN is engaged in self-referential (internal) thinking and is disengaged during attentional-demanding (external) processes (Sheline et al., 2009). Thus, greater activity within the DMN when individuals are at rest is thought to be reflective of difficulties in switching from internal to external thoughts (Bozhilova, Michelini, Kuntsi, & Asherson, 2018). In participants with CHD, this may reflect their cognitive and attentional dysfunction in daily life (Batra,

Alexander, & Silka, 2012; Holst et al., 2020; Pierick, Lynn, McCracken, Oster, & Iannucci, 2021), as they may experience difficulties switching from internal to external stimulation. However, considering that we have not evaluated attention and hyperactivity, this hypothesis remains speculative. Similarly, altered amygdalar connectivity, combined with DMN dysfunction, may underlie in part some of the difficulties in regulating emotions or internal states that are frequently observed in individuals with CHD (Bauml et al., 2019)

Participants with CHD also demonstrated increased functional connectivity in the dorsal attention network and the fronto-parietal network when compared to controls. The dorsal attention network is known to be engaged during externally directed attentional tasks and its activity is increased when individuals must focus their attention on external stimuli. Its level of activity is thought to reflect and predict attentional skills (Rohr et al., 2017). Although we did not evaluate attention specifically, participants with CHD presented with lower scores on the organization of materials scale, likely reflecting difficulty when handling more than one stimulus at the same time, which is driven in part by attentional skills. Regarding the fronto-parietal network differences, increased resting-state functional connectivity was specifically observed in the CHD group between the parietal cortex and the cerebellar Crus 1 and Crus 2 regions. Theses cerebellar regions are known to be involved in executive functions, coherent with our findings (Z. Gao, Liu, Zhang, Liu, & Hao, 2020).

When performing correlations between functional connectivity and BRIEF-A scores, we observed different modest correlations in the two groups. Interestingly, we observed a negative correlation between amygdala – cingulate/paracingulate gyrus connectivity and the organization of materials scale in the control group, while a positive correlation between the default mode intra-network functional connectivity and this scale was detected in the CHD group. Higher levels of inhibition have been shown to correlate with decreased amygdala – cingulate functional connectivity (Blackford et al., 2014). However, we could not find previous reports of a relationship of organizational cognitive tasks with amygdala – cingulate or default mode network functional connectivity. The lack of strong associations in these exploratory analyses may have been mitigated by the use of a self-reported questionnaire to measure executive functioning, which may have induced some bias. Although the BRIEF-A has been demonstrated to be valid and reliable for measuring executive function in various clinical populations (Rouel et al., 2016), standardized batteries may be more objective in examining a wider range of higher-order cognitive performance.

Abnormalities in functional connectivity may reflect alterations of the structural organization of white matter tracts. Indeed, several diffusion tensor imaging studies have detected lower fractional anisotropy in adolescents with CHD (Brewster, King, Burns, Drossner, & Mahle, 2015; Easson et al., 2020; Ehrler et al., 2020; Rivkin et al., 2013; Watson et al., 2018). These findings may reflect potential alterations to numerous facets of white matter microstructure, including alterations to myelination, axon density, axon diameter, axon orientation, or cell membrane permeability (D. K. Jones, Knosche, & Turner, 2013). Additionally, we recently applied neurite orientation dispersion and density imaging, an advanced diffusion MRI modelling technique, in this cohort of CHD survivors, detecting widespread reductions in the neurite density index, reflecting a lower density of axon packing (Easson et al., 2020). Altered regions included frontal and limbic white matter tracts, in line with the altered functional connectivity we describe in these regions. Nevertheless, future multi-modal MRI studies combining structural and functional connectivity analyses are needed to disentangle these complex relationships.

4.5.1 Limitations

Our results should be considered within the context of their limitations. It is important to highlight that our sample of CHD participants included a mixed cohort of different CHD physiologies, and therefore cannot be generalized to a specific subtype. Nevertheless, the fact that we included participants with a variety of complex CHD physiologies operated during infancy is representative of the clinical diversity of this condition. Lastly, the differences found in socioeconomic status between the two groups may be a limitation of the study; however, we carefully corrected for this potential confounder in our analyses.

4.6 Conclusion

The current study provides the first evidence supporting the presence of altered functional connectivity in youth born with complex CHD. Specifically, we found atypical functional connectivity in youth with CHD in the fronto-orbital cortex, amygdala, default mode, dorsal attention, and fronto-parietal networks. In this new era of open-science, future studies using longitudinal imaging in large multi-center cohorts will strengthen our understanding of long-term altered connectivity and how to measure the risk for these alterations at an individual level, in order to better identify at-risk children and adolescents that could benefit from targeted therapies

4.7 Acknowledgment

We would like to thank the participants and their families for their participation, and the clinicians, technologists, and research assistants for their implication in this study. At the time of the study, VE received studentship support from Québec Bio-Imaging Network, GAL held a Fonds de recherche du Québec – Santé (FRQ-S) Research Scholar Awards, and MBR a Canada Research Chair in Brain and Child Development.

4.8 Author contribution statement

V. Enguix: Methodology, Formal analysis, Writing- Original draft preparation; **K.Easson:** Data curation, Project administration, Writing- Reviewing and Editing; **G. Gilbert:** Methodology, Resources, Writing - Reviewing and Editing; **C. Saint-Martin:** Resources, Writing - Reviewing and Editing; **C. Rohlicek**: Resources, Writing - Reviewing and Editing; **D. Luck:** Writing- Reviewing and Editing; **G.A Lodygensky:** Conceptualization, Validation, Resources, Supervision, Writing - original draft; Reviewing and Editing; **M. Brossard-Racine**: Conceptualization, Validation, Investigation; Methodology; Project administration, Resources, Supervision, Funding acquisition; Writing - original draft; Reviewing and Editing;

4.9 Declaration of interests

Guillaume Gilbert is an employee of Philips Healthcare who per our institutional agreement provided support during the implementation of the MRI acquisition protocol. Philips Healthcare provided support in the form of salaries for one author [G.G], but did not fund or sponsored the study and did not have any additional role in the study design, data collection and analysis, decision to publish, or preparation of the manuscript. The specific role of this author is articulated in the 'author contributions' section. This does not alter our adherence to PLOS ONE policies on sharing data and materials.

4.10 References

Alonazi, B. K., Keller, S. S., Fallon, N., Adams, V., Das, K., Marson, A. G., & Sluming, V. (2019). Resting-state functional brain networks in adults with a new diagnosis of focal epilepsy. *Brain Behav, 9*(1), e01168. doi:10.1002/brb3.1168

Bagge, C. N., Henderson, V. W., Laursen, H. B., Adelborg, K., Olsen, M., & Madsen, N. L. (2018). Risk of Dementia in Adults With Congenital Heart Disease: Population-Based Cohort Study. *Circulation, 137*(18), 1912-1920. doi:10.1161/CIRCULATIONAHA.117.029686

Banks, S. J., Eddy, K. T., Angstadt, M., Nathan, P. J., & Phan, K. L. (2007). Amygdala-frontal connectivity during emotion regulation. *Soc Cogn Affect Neurosci, 2*(4), 303-312. doi:10.1093/scan/nsm029

Barbey, A. K., Koenigs, M., & Grafman, J. (2011). Orbitofrontal contributions to human working memory. *Cereb Cortex, 21*(4), 789-795. doi:10.1093/cercor/bhq153

Batra, A. S., Alexander, M. E., & Silka, M. J. (2012). Attention-deficit/hyperactivity disorder, stimulant therapy, and the patient with congenital heart disease: evidence and reason. *Pediatr Cardiol, 33*(3), 394-401. doi:10.1007/s00246-012-0162-6

Bauml, J. G., Baumann, N., Avram, M., Mulej Bratec, S., Breeman, L., Berndt, M., . . . Sorg, C. (2019). The Default Mode Network Mediates the Impact of Infant Regulatory Problems on Adult Avoidant Personality Traits. *Biol Psychiatry Cogn Neurosci Neuroimaging, 4*(4), 333-342. doi:10.1016/j.bpsc.2018.11.005

Behzadi, Y., Restom, K., Liau, J., & Liu, T. T. (2007). A component based noise correction method (CompCor) for BOLD and perfusion based fMRI. *Neuroimage, 37*(1), 90-101. doi:10.1016/j.neuroimage.2007.04.042

Bernier, P. L., Stefanescu, A., Samoukovic, G., & Tchervenkov, C. I. (2010). The challenge of congenital heart disease worldwide: epidemiologic and demographic facts. *Semin Thorac Cardiovasc Surg Pediatr Card Surg Annu, 13*(1), 26-34. doi:10.1053/j.pcsu.2010.02.005

Biswal, B., Yetkin, F. Z., Haughton, V. M., & Hyde, J. S. (1995). Functional connectivity in the motor cortex of resting human brain using echo-planar MRI. *Magn Reson Med, 34*(4), 537-541. doi:10.1002/mrm.1910340409

Blackford, J. U., Clauss, J. A., Avery, S. N., Cowan, R. L., Benningfield, M. M., & VanDerKlok, R. M. (2014). Amygdala-cingulate intrinsic connectivity is associated with degree of social inhibition. *Biol Psychol, 99*, 15-25. doi:10.1016/j.biopsycho.2014.02.003

Bolduc, M. E., Lambert, H., Ganeshamoorthy, S., & Brossard-Racine, M. (2018). Structural brain abnormalities in adolescents and young adults with congenital heart defect: a systematic review. *Dev Med Child Neurol, 60*(12), 1209-1224. doi:10.1111/dmcn.13975

Bozhilova, N. S., Michelini, G., Kuntsi, J., & Asherson, P. (2018). Mind wandering perspective on attention-deficit/hyperactivity disorder. *Neurosci Biobehav Rev, 92*, 464-476. doi:10.1016/j.neubiorev.2018.07.010

Brewster, R. C., King, T. Z., Burns, T. G., Drossner, D. M., & Mahle, W. T. (2015). White Matter Integrity Dissociates Verbal Memory and Auditory Attention Span in Emerging Adults with Congenital Heart Disease. *J Int Neuropsychol Soc, 21*(1), 22-33. doi:10.1017/S135561771400109X

Brossard-Racine, M., du Plessis, A., Vezina, G., Robertson, R., Donofrio, M., Tworetzky, W., & Limperopoulos, C. (2016). Brain Injury in Neonates with Complex Congenital Heart Disease: What Is the Predictive Value of MRI in the Fetal Period? *AJNR Am J Neuroradiol, 37*(7), 1338-1346. doi:10.3174/ajnr.A4716

Buckner, R. L., Andrews-Hanna, J. R., & Schacter, D. L. (2008). The brain's default network: anatomy, function, and relevance to disease. *Ann N Y Acad Sci, 1124*, 1-38. doi:10.1196/annals.1440.011

Calderon, J., & Bellinger, D. C. (2015). Executive function deficits in congenital heart disease: why is intervention important? *Cardiol Young, 25*(7), 1238-1246. doi:10.1017/S1047951115001134

Cassidy, A. R., White, M. T., DeMaso, D. R., Newburger, J. W., & Bellinger, D. C. (2015). Executive Function in Children and Adolescents with Critical Cyanotic Congenital Heart Disease. *J Int Neuropsychol Soc, 21*(1), 34-49. doi:10.1017/S1355617714001027

Cullen, K. R., Westlund, M. K., Klimes-Dougan, B., Mueller, B. A., Houri, A., Eberly, L. E., & Lim, K. O. (2014). Abnormal amygdala resting-state functional connectivity in adolescent depression. *JAMA Psychiatry, 71*(10), 1138-1147. doi:10.1001/jamapsychiatry.2014.1087

Davey, C. G., Pujol, J., & Harrison, B. J. (2016). Mapping the self in the brain's default mode network. *Neuroimage, 132*, 390-397. doi:10.1016/j.neuroimage.2016.02.022

De Asis-Cruz, J., Donofrio, M. T., Vezina, G., & Limperopoulos, C. (2018). Aberrant brain functional connectivity in newborns with congenital heart disease before cardiac surgery. *Neuroimage Clin, 17*, 31-42. doi:10.1016/j.nicl.2017.09.020

DeMaso, D. R., Calderon, J., Taylor, G. A., Holland, J. E., Stopp, C., White, M. T., . . . Newburger, J. W. (2017). Psychiatric Disorders in Adolescents With Single Ventricle Congenital Heart Disease. *Pediatrics, 139*(3). doi:10.1542/peds.2016-2241

Easson, K., Dahan-Oliel, N., Rohlicek, C., Sahakian, S., Brossard-Racine, M., Mazer, B., . . . Majnemer, A. (2019). A Comparison of Developmental Outcomes of Adolescent Neonatal Intensive Care Unit Survivors Born with a Congenital Heart Defect or Born Preterm. *J Pediatr, 207*, 34-41 e32. doi:10.1016/j.jpeds.2018.11.002

Easson, K., Rohlicek, C. V., Houde, J. C., Gilbert, G., Saint-Martin, C., Fontes, K., . . . Brossard-Racine, M. (2020). Quantification of apparent axon density and orientation dispersion in the white matter of youth born with congenital heart disease. *Neuroimage, 205*, 116255. doi:10.1016/j.neuroimage.2019.116255

Ehrler, M., Latal, B., Kretschmar, O., von Rhein, M., & O'Gorman Tuura, R. (2020). Altered frontal white matter microstructure is associated with working memory impairments in adolescents with congenital heart disease: A diffusion tensor imaging study. *Neuroimage Clin, 25*, 102123. doi:10.1016/j.nicl.2019.102123

Figueroa, C. A., Mocking, R. J. T., van Wingen, G., Martens, S., Ruhe, H. G., & Schene, A. H. (2017). Aberrant default-mode network-hippocampus connectivity after sad memory-recall in remitted-depression. *Soc Cogn Affect Neurosci, 12*(11), 1803-1813. doi:10.1093/scan/nsx108

Figueroa-Vargas, A., Carcamo, C., Henriquez-Ch, R., Zamorano, F., Ciampi, E., Uribe-San-Martin, R., . . . Billeke, P. (2020). Frontoparietal connectivity correlates with working memory performance in multiple sclerosis. *Sci Rep, 10*(1), 9310. doi:10.1038/s41598-020-66279-0

Fontes, K., Courtin, F., Rohlicek, C. V., Saint-Martin, C., Gilbert, G., Easson, K., . . . Brossard-Racine, M. (2020). Characterizing the Subcortical Structures in Youth with Congenital Heart Disease. *American Journal of Neuroradiology, 41*(8), 1503-1508. doi:10.3174/ajnr.A6667

Fontes, K., Rohlicek, C. V., Saint-Martin, C., Gilbert, G., Easson, K., Majnemer, A., . . . Brossard-Racine, M. (2019). Hippocampal alterations and functional correlates in adolescents and young adults with congenital heart disease. *Hum Brain Mapp, 40*(12), 3548-3560. doi:10.1002/hbm.24615

Frank, D. W., Dewitt, M., Hudgens-Haney, M., Schaeffer, D. J., Ball, B. H., Schwarz, N. F., . . . Sabatinelli, D. (2014). Emotion regulation: quantitative meta-analysis of functional activation and deactivation. *Neurosci Biobehav Rev, 45*, 202-211. doi:10.1016/j.neubiorev.2014.06.010

Friston, K. J., Williams, S., Howard, R., Frackowiak, R. S., & Turner, R. (1996). Movement-related effects in fMRI time-series. *Magn Reson Med, 35*(3), 346-355. doi:10.1002/mrm.1910350312

Gao, Z., Liu, X., Zhang, D., Liu, M., & Hao, N. (2020). The indispensable role of the cerebellum in visual divergent thinking. *Sci Rep, 10*(1), 16552. doi:10.1038/s41598-020-73679-9

Gardini, S., Venneri, A., Sambataro, F., Cuetos, F., Fasano, F., Marchi, M., . . . Caffarra, P. (2015). Increased functional connectivity in the default mode network in mild cognitive impairment: a maladaptive compensatory mechanism associated with poor semantic memory performance. *J Alzheimers Dis, 45*(2), 457-470. doi:10.3233/JAD-142547

Hojjati, S. H., Ebrahimzadeh, A., & Babajani-Feremi, A. (2019). Identification of the Early Stage of Alzheimer's Disease Using Structural MRI and Resting-State fMRI. *Front Neurol, 10*, 904. doi:10.3389/fneur.2019.00904

Hollingshead, A. B. (1975). *Four factor index of social status*. New Haven, Conn.: Yale University, Dept. of Sociology.

Holst, L. M., Kronborg, J. B., Jepsen, J. R. M., Christensen, J. O., Vejlstrup, N. G., Juul, K., . . . Ravn, H. B. (2020). Attention-deficit/hyperactivity disorder symptoms in children with surgically corrected Ventricular Septal Defect, Transposition of the Great Arteries, and Tetralogy of Fallot. *Cardiol Young, 30*(2), 180-187. doi:10.1017/S1047951119003184

Jones, D. K., Knosche, T. R., & Turner, R. (2013). White matter integrity, fiber count, and other fallacies: the do's and don'ts of diffusion MRI. *Neuroimage, 73*, 239-254. doi:10.1016/j.neuroimage.2012.06.081

Keir, M., Ebert, P., Kovacs, A. H., Smith, J. M. C., Kwan, E., Field, T. S., . . . Marelli, A. (2019). Neurocognition in Adult Congenital Heart Disease: How to Monitor and Prevent Progressive Decline. *Canadian Journal of Cardiology, 35*(12), 1675-1685. doi:10.1016/j.cjca.2019.06.020

Latal, B., Patel, P., Liamlahi, R., Knirsch, W., O'Gorman Tuura, R., & von Rhein, M. (2016). Hippocampal volume reduction is associated with intellectual functions in adolescents with congenital heart disease. *Pediatr Res, 80*(4), 531-537. doi:10.1038/pr.2016.122

LeDoux, J. (2007). The amygdala. *Curr Biol, 17*(20), R868-874. doi:10.1016/j.cub.2007.08.005

Lee, M. H., Smyser, C. D., & Shimony, J. S. (2013). Resting-state fMRI: a review of methods and clinical applications. *AJNR Am J Neuroradiol, 34*(10), 1866-1872. doi:10.3174/ajnr.A3263

Lindquist, M. A., & Wager, T. D. (2008). Spatial smoothing in fMRI using prolate spheroidal wave functions. *Hum Brain Mapp, 29*(11), 1276-1287. doi:10.1002/hbm.20475

Liu, W., Hu, X., An, D., Zhou, D., & Gong, Q. (2019). Resting-state functional connectivity alterations in periventricular nodular heterotopia related epilepsy. *Sci Rep, 9*(1), 18473. doi:10.1038/s41598-019-55002-3

Marelli, A., Miller, S. P., Marino, B. S., Jefferson, A. L., & Newburger, J. W. (2016). Brain in Congenital Heart Disease Across the Lifespan: The Cumulative Burden of Injury. *Circulation, 133*(20), 1951-1962. doi:10.1161/CIRCULATIONAHA.115.019881

Motoyama, Y., Oshiro, Y., Takao, Y., Sato, H., Obata, N., Izuta, S., . . . Kan, S. (2019). Resting-state brain functional connectivity in patients with chronic pain who responded to subanesthetic-dose ketamine. *Sci Rep, 9*(1), 12912. doi:10.1038/s41598-019-49360-1

Murphy, K., Birn, R. M., Handwerker, D. A., Jones, T. B., & Bandettini, P. A. (2009). The impact of global signal regression on resting state correlations: are anti-correlated networks introduced? *Neuroimage, 44*(3), 893-905. doi:10.1016/j.neuroimage.2008.09.036

Muschelli, J., Nebel, M. B., Caffo, B. S., Barber, A. D., Pekar, J. J., & Mostofsky, S. H. (2014). Reduction of motion-related artifacts in resting state fMRI using aCompCor. *Neuroimage, 96*, 22-35. doi:10.1016/j.neuroimage.2014.03.028

Pierick, A. R., Lynn, M., McCracken, C. M., Oster, M. E., & Iannucci, G. J. (2021). Treatment of attention deficit/hyperactivity disorder in children with CHD. *Cardiol Young*, 1-4. doi:10.1017/S1047951120004965

Pike, N. A., Roy, B., Gupta, R., Singh, S., Woo, M. A., Halnon, N. J., . . . Kumar, R. (2018). Brain abnormalities in cognition, anxiety, and depression regulatory regions in adolescents with single ventricle heart disease. *J Neurosci Res, 96*(6), 1104-1118. doi:10.1002/jnr.24215

Power, J. D., Barnes, K. A., Snyder, A. Z., Schlaggar, B. L., & Petersen, S. E. (2012). Spurious but systematic correlations in functional connectivity MRI networks arise from subject motion. *Neuroimage, 59*(3), 2142-2154. doi:10.1016/j.neuroimage.2011.10.018

Power, J. D., Mitra, A., Laumann, T. O., Snyder, A. Z., Schlaggar, B. L., & Petersen, S. E. (2014). Methods to detect, characterize, and remove motion artifact in resting state fMRI. *Neuroimage, 84*, 320-341. doi:10.1016/j.neuroimage.2013.08.048

Reid, G. J., Webb, G. D., Barzel, M., McCrindle, B. W., Irvine, M. J., & Siu, S. C. (2006). Estimates of life expectancy by adolescents and young adults with congenital heart disease. *J Am Coll Cardiol, 48*(2), 349-355. doi:10.1016/j.jacc.2006.03.041

Rivkin, M. J., Watson, C. G., Scoppettuolo, L. A., Wypij, D., Vajapeyam, S., Bellinger, D. C., . . . Newburger, J. W. (2013). Adolescents with D-transposition of the great arteries repaired in early infancy demonstrate reduced white matter microstructure associated with clinical risk factors. *J Thorac Cardiovasc Surg, 146*(3), 543-549 e541. doi:10.1016/j.jtcvs.2012.12.006

Rohr, C. S., Vinette, S. A., Parsons, K. A. L., Cho, I. Y. K., Dimond, D., Benischek, A., . . . Bray, S. (2017). Functional Connectivity of the Dorsal Attention Network Predicts Selective

Attention in 4-7 year-old Girls. *Cereb Cortex, 27*(9), 4350-4360. doi:10.1093/cercor/bhw236

Ross, R. S., LoPresti, M. L., Schon, K., & Stern, C. E. (2013). Role of the hippocampus and orbitofrontal cortex during the disambiguation of social cues in working memory. *Cogn Affect Behav Neurosci, 13*(4), 900-915. doi:10.3758/s13415-013-0170-x

Rouel, M., Raman, J., Hay, P., & Smith, E. (2016). Validation of the Behaviour Rating Inventory of Executive Function - Adult Version (BRIEF-A) in the obese with and without binge eating disorder. *Eat Behav, 23*, 58-65. doi:10.1016/j.eatbeh.2016.07.010

Sheline, Y. I., Barch, D. M., Price, J. L., Rundle, M. M., Vaishnavi, S. N., Snyder, A. Z., . . . Raichle, M. E. (2009). The default mode network and self-referential processes in depression. *Proc Natl Acad Sci U S A, 106*(6), 1942-1947. doi:10.1073/pnas.0812686106

Skoczek, A., Prochownik, P., Gancarczyk, U., Libiszewska, N., Podolec, P., & Komar, M. (2019). Personality traits of patients suffering from congenital heart defects. *Wiad Lek, 72*(11 cz 1), 2135-2144. Retrieved from https://www.ncbi.nlm.nih.gov/pubmed/31860861

Tang, S., Lu, L., Zhang, L., Hu, X., Bu, X., Li, H., . . . Huang, X. (2018). Abnormal amygdala resting-state functional connectivity in adults and adolescents with major depressive disorder: A comparative meta-analysis. *EBioMedicine, 36*, 436-445. doi:10.1016/j.ebiom.2018.09.010

Tomiyama, H., Nakao, T., Murayama, K., Nemoto, K., Ikari, K., Yamada, S., . . . Kanba, S. (2019). Dysfunction between dorsal caudate and salience network associated with impaired cognitive flexibility in obsessive-compulsive disorder: A resting-state fMRI study. *Neuroimage Clin, 24*, 102004. doi:10.1016/j.nicl.2019.102004

Tyagi, M., Fteropoulli, T., Hurt, C. S., Hirani, S. P., Rixon, L., Davies, A., . . . Newman, S. P. (2017). Cognitive dysfunction in adult CHD with different structural complexity. *Cardiol Young, 27*(5), 851-859. doi:10.1017/S1047951116001396

von Rhein, M., Buchmann, A., Hagmann, C., Huber, R., Klaver, P., Knirsch, W., & Latal, B. (2014). Brain volumes predict neurodevelopment in adolescents after surgery for congenital heart disease. *Brain, 137*(Pt 1), 268-276. doi:10.1093/brain/awt322

Wang, Y., Qin, Y., Li, H., Yao, D., Sun, B., Li, Z., . . . Luo, C. (2019). Abnormal Functional Connectivity in Cognitive Control Network, Default Mode Network, and Visual Attention Network in Internet Addiction: A Resting-State fMRI Study. *Front Neurol, 10*, 1006. doi:10.3389/fneur.2019.01006

Watson, C. G., Asaro, L. A., Wypij, D., Robertson, R. L., Jr., Newburger, J. W., & Rivkin, M. J. (2016). Altered Gray Matter in Adolescents with d-Transposition of the Great Arteries. *J Pediatr, 169*, 36-43 e31. doi:10.1016/j.jpeds.2015.09.084

Watson, C. G., Stopp, C., Wypij, D., Bellinger, D. C., Newburger, J. W., & Rivkin, M. J. (2018). Altered White Matter Microstructure Correlates with IQ and Processing Speed in Children and Adolescents Post-Fontan. *J Pediatr, 200*, 140-149 e144. doi:10.1016/j.jpeds.2018.04.022

Wehrle, F. M., Michels, L., Guggenberger, R., Huber, R., Latal, B., O'Gorman, R. L., & Hagmann, C. F. (2018). Altered resting-state functional connectivity in children and adolescents born very preterm short title. *Neuroimage Clin, 20*, 1148-1156. doi:10.1016/j.nicl.2018.10.002

Whitfield-Gabrieli, S., & Nieto-Castanon, A. (2012). Conn: a functional connectivity toolbox for correlated and anticorrelated brain networks. *Brain Connect, 2*(3), 125-141. doi:10.1089/brain.2012.0073

Zhang, L., Zuo, X. N., Ng, K. K., Chong, J. S. X., Shim, H. Y., Ong, M. Q. W., . . . Zhou, J. H. (2020). Distinct BOLD variability changes in the default mode and salience networks in Alzheimer's disease spectrum and associations with cognitive decline. *Sci Rep, 10*(1), 6457. doi:10.1038/s41598-020-63540-4

CHAPTER 5 NEONATAL RS-FMRI ACQUISITION

This chapter describes the neonatal rs-fMRI acquisition protocol set up for the 3T GE Discovery MR750 from the CHU Sainte-Justine. It also provides a real-time head motion quality control to ensure that enough low motion rs-fMRI data have been collected before the baby leaves the MRI room. The rs-fMRI acquisition consists of two 5-minutes single-shot interleaved GRE-EPI and the quality control is performed right after each 5-minutes acquisition.

5.1 CHU Sainte-Justine research neonatal acquisition protocol

Data is acquired using an MRI 3T GE Discovery MR750 using a 32-channel head coil. The acquisition protocol includes a 3D Fast Spoiled Gradient BRAVO, a 3D T2 CUBE, a 32-directions diffusion tensor imaging, two reversed phase encoding polarity 26-directions diffusion basis spectrum imaging, and two reversed phase encoding direction GRE-EPI rs-fMRI. Only T2-weighted and rs-fMRI sequences will be further discussed in this section, as the rest of the sequences are outside this project's scope. Nonetheless, it is convenient to present every sequence in the acquisition protocol as the acquisition time, the sequence order, or the energy deposit per mass may influence the whole acquisition protocol.

Structural 3D T1- and T2-weighted images are acquired to ensure high-resolution data to identify the different brain structures. T1-weighted images are acquired as a part of the protocol to identify specific brain injuries, such as punctate white matter lesions (Nguyen et al., 2019). However, as previously mentioned, for the neonatal population, the most appropriate in terms of contrast are T2-weighted images, as the brain is not fully myelinated. The high-resolution T2-weighted images will serve as a reference for further data preprocessing of the functional data and will allow proper tissue segmentation. The CUBE T2 sequence was selected as it enables contiguous sub-millimeter high SNR data acquisition by replacing several 2D slice acquisitions with a single 3D volume. Furthermore, 3D Fast SE reduces energy deposit as the scanning time is reduced and, more importantly, presents reduced flip angles compared to traditional SE. Traditional SE 180º pulses require fast switching of the magnetic field gradients, increasing this way the SAR. The SAR

corresponds to the energy deposit in the body tissue by the radiofrequency field, and it's given in watts/kg. It can be described as

$$SAR = (\sigma A^2 \omega^2 B_l^2 \mathrm{D})/2\rho$$

Where σ is the tissue conductivity, A is the body cross-sectional area, ω is the RF frequency, B_l is the mean amplitude of the RF pulse, D is the duty cycle, which corresponds to the percentage of time the RF is activated, and ρ is the body mass.

We can observe that SAR increases with the volume, being the deposit of energy in neonates a fourfold of the deposit in adults because of the reduced tissue volume. However, SAR is essential when scanning neonates for being much more vulnerable. SAR produces an elevation of the tissue temperature of approximately 1ºC/hour for a SAR of 1 watt/kg, which may produce heat-induced injury. For example, a commonly used T2-weighted acquisition sequence in clinical MRI is SE PROPELLER. This sequence allows oversampling the center of the k-space to obtain high SNR and contrast; however, it also presents a high SAR, limiting the acquisition to a few slices to avoid overheating. For instance, the SE PROPELLER used in clinical MRI at the CHU Sainte-Justine produces 1.96 watts/kg in contrast to the 1.31 watts/kg produced by the 3D CUBE.

The rs-fMRI acquisition consists of two single-shot interleaved GRE-EPI with reversed phase encoding polarity to perform distortion correction. One hundred volumes plus five dummies are acquired per acquisition, and each acquisition takes 5 min and 15 seconds, for a total of 200 volumes (10 min 30 s). The employed TE is 30 ms as it provides decent values of SNR while staying centered close to the T2* value of the main resting-state networks (Rajasilta et al., 2020; Rogers et al., 2017; Smyser et al., 2010; Smyser et al., 2016). A TR of 3 seconds is employed, and a flip angle of 70º. We decided to keep the acquisition parameters unaltered to perform group comparisons with the previously acquired neonates; however, some possible improvements in the acquisition protocol will be further discussed.

5.2 Real-time head motion monitoring and MRI acquisition

Resting-state fMRI is a 4D acquisition technique, making it susceptible to head motion. Head motion produces mismatches between the different acquired volumes and can create false correlations that don't correspond to neural signals. Currently, due to high levels of head motion, approximately half of the acquired pediatric data cannot be analyzed. To address this challenge in

the CHU Sainte-Justine, a real-time head motion monitoring protocol was developed as a part of this project. The head motion real-time quality control allows us to determine whether or not the acquired neonatal rs-fMRI data is of enough quality to be further analyzed. If the collected data doesn't pass the quality control the baby is re-scanned.

To set up the real time head motion quality control in the CHU Sainte-Justine, we decided to perform two 5-minute GRE-EPI with reversed phase encoding polarity instead of one acquisition of 10-minutes plus several volumes in reversed phase encoding polarity for several reasons. First, the software of the 3T GE Discovery MR750 from CHU Sainte-Justine doesn't allow for real-time data extraction. Therefore, performing two shorter consecutive GRE-EPI allows us to complete the head motion quality control of the first acquisition while the next 5 minutes are collected. This optimizes the time in the MRI. But most importantly, it enables us to immediately re-scan the baby if the first acquisition didn't pass the quality controls. Also, acquiring two consecutive GRE-EPI of the same length reduces distortions in the anterior and posterior regions as they appear averaged.

The quality control is based on functional cross realignment of the rs-fMRI data. This technique consists of 6 degrees of freedom image registration between every acquired volume and the reference volume. The 6 degrees of freedom correspond to 3 rotations around the x-axis (pitch), y-axis (yaw), and z-axis (roll), and 3 translations in x-(left/right), y- (anterior/posterior), and z-axes (inferior/superior). The registration parameters for every volume are saved as a matrix and then employed to compute the framewise displacement of every volume. This metric described by Power et al. 2012 allows to index the head movement from one volume to the next and can be described as the addition of the absolute value of the 6 registration parameters (Power et al., 2012).

To determine the acceptable levels of head motion, we preprocessed N=16 babies from the CHU Sainte-Justine dataset and N=11 from the Baby Connectome Project (Howell et al., 2019). We evaluated several metrics, including the total number of volumes, the number of volumes with excessive motion (framewise displacement > 0.25mm)(Smyser et al., 2016), and the average framewise displacement of the whole run. Finally, the average framewise displacement was selected as the main metric for quality control as it provides information about the whole run. It is easy to interpret, as it doesn't depend on other factors such as the TR and showed linear correlation with the proportion of bad volumes over the total number of acquired volumes [r (CHU Sainte-Justine dataset)=0.92; r(Baby Connectome Project dataset)=0.89]. Finally, we performed seed-

based correlation to explore different resting-state networks: language, motor, visual primary, and default mode networks. A single seed region was used to characterize each resting-state network. The average time series of every seed region was extracted and then correlated with the rest of the voxels of the brain to obtain the Pearson correlation values. The Pearson correlation values were Fisher transformed and thresholded between 0.5 and 1.5. We then evaluated the results of both cohorts through qualitative assessment to determine the limit values of average framewise displacement.

For the CHU Sainte-Justine dataset, we could distinguish the aforementioned resting-state networks when at least two 5-minute acquisitions presented an average framewise displacement inferior to 0.25 mm per acquisition. For very low framewise displacement sequences, 5-minutes seemed enough to characterize the resting-state networks. The Baby Connectome Project dataset needed only a 5-minute acquisition to characterize the resting-state networks. This is probably because of the higher number of samples per 5 minutes acquired, being 420 samples/run for the Baby Connectome Project dataset versus 100 samples/run for the CHU Sainte-Justine. The Baby Connectome Project uses a TR of 0.72 seconds compared to our TR of 3 seconds, which explains the higher number of samples for the same scanning time. Interestingly, the observed average framewise displacement limit was 0.25 mm for both datasets.

When evaluating the different resting-state networks, preterm and term-equivalent age subjects were employed when analyzing the CHU Sainte-Justine dataset. Full-term infants were evaluated in the Baby Connectome Project dataset. This may also explain slight differences in the resting-state networks due to development, such as network bilaterality.

Motion in newborns from the CHU Sainte-Justine dataset with different levels of average framewise displacement (noted as FD) for the language, motor, primary visual, and default mode are presented in Figure 5.1.

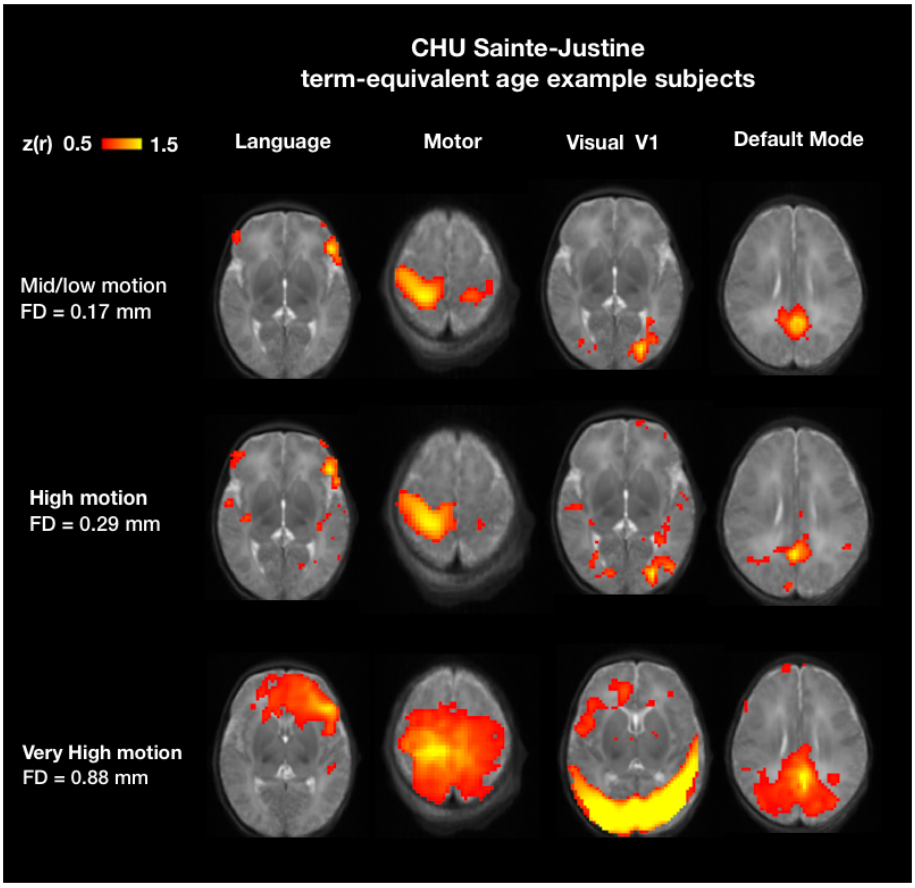

Figure 5.1. CHU Sainte-Justine resting-state networks for different average framewise displacements (FD).

Motion in newborns from the Baby Connectome Project dataset with different levels of average framewise displacement (noted as FD) for the language, motor, primary visual, and default mode are presented in Figure 5.2.

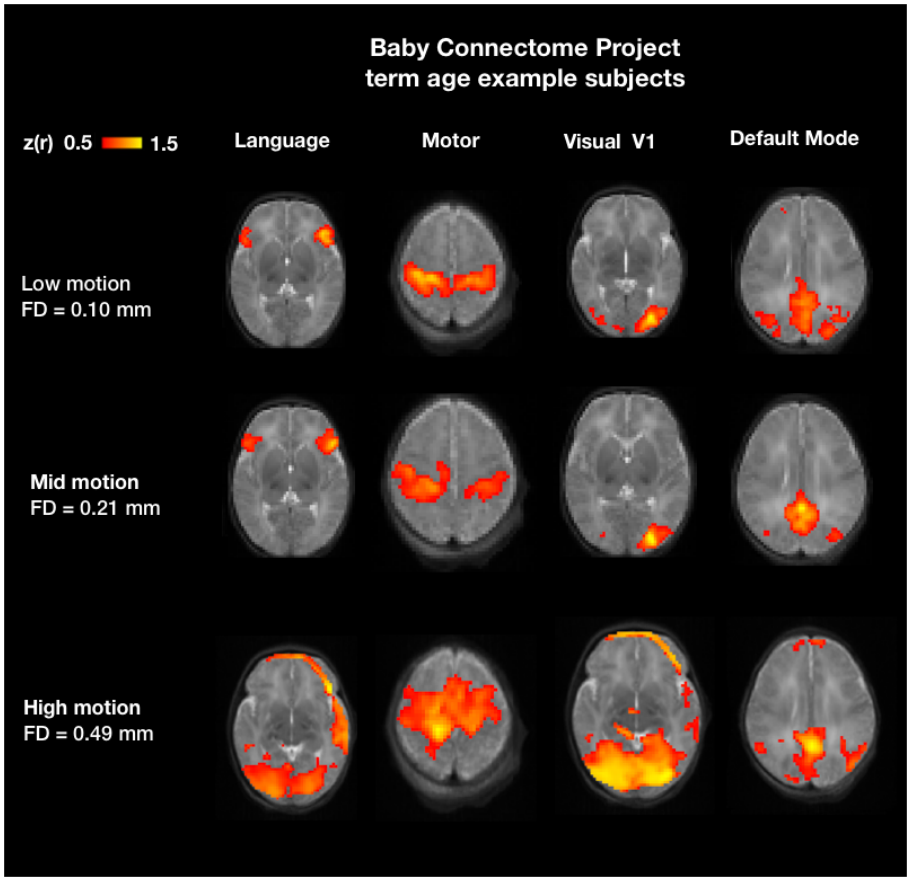

Figure 5.2. Baby Connectome Project resting-state networks for different average framewise displacements (FD).

5.3 Protocol optimization

We observed that at the beginning of the acquisition procedure, babies presented lower levels of motion as they were still completely sleeping. Also, we observed that they tolerate EPI acquisitions very well. Therefore, doing rs-fMRI at the beginning of the acquisition protocol minimized head motion and improved data quality. Also, as mentioned in the previous section, real-time head motion monitoring is crucial to ensure that good quality rs-fMRI data has been acquired and that it will be possible to analyze. As it has been shown, acquiring more than 10 minutes of rs-fMRI can significantly improve reliability not only due to the increased number of time points but also because of the increased total scan duration (Anderson, Ferguson, Lopez-Larson, & Yurgelun-Todd, 2011; Birn et al., 2013). Performing three scans of 5 minutes would improve the reliability

and ensure that at least 10 minutes of data would present the required quality to be analyzed. As mentioned before, with the current setup, head motion assessment has to be performed while the following sequence is being acquired and can't be performed in real-time. Though, the implementation of this procedure improved the overall data quality allowing us to process a higher number of babies that other ways would have been discarded. The intention is to perform the quality control of the first scan during the acquisition of the second one and then perform the quality control of the second scan during the acquisition of the third one. If scan one or two don't pass the quality control, additional scans could be added until having at least 10 minutes of good quality data.

The TR is the second parameter that needs to be optimized in our acquisition protocol. Even if multi-band acquisitions can't be performed with the current setup due to MRI software-related incompatibilities specified by the GE technical service, the TR could also be improved. For example, let's compare the neonatal resting-state acquisition from the CHU Sainte-Justine with the acquisition performed by De Asis Cruz et al. (De Asis-Cruz, Bouyssi-Kobar, Evangelou, Vezina, & Limperopoulos, 2015) using the same scanner [Table 5.1]. We observed that achieving the same number of slices with similar acquisition parameters requires a TR of 2000 ms instead of 3000 ms. This improves temporal resolution, reduces head motion artifacts, and allows the acquisition of more time points in the same amount of time. Ideally, a multi-band sequence would allow improving the spatial resolution to 2x2x2 mm while keeping a TR of less than 1000 ms, with the aforementioned benefits from a lower TR, and allowing to skip the slice timing correction preprocessing step due to the high sampling frequency (Glasser et al., 2013).

Furthermore, the flip angle could also be optimized to match the Ernst angle to maximize the SNR (Glasser et al., 2013). In such a way, the equation presented in the literature review could be employed to determine the flip angle that maximizes the signal value in GRE-EPI. Another potential improvement would be the reduction of the flip angle under the Ernst angle value. Gonzalo-Castillo et al. showed that a reduction of the flip angle under the Ernst value for the study of gray matter using sequences such as gradient echo for fMRI could significantly reduce the RF power, reducing this way the risk of heat-induced injury without compromising the signal (Gonzalez-Castillo, Roopchansingh, Bandettini, & Bodurka, 2011).

Table 5.1. Single-band rs-fMRI acquisition between centers comparison

	CHU Sainte Justine	**De Asis Cruz et al.**
MRI	GE Discovery MR750	GE Discovery MR750
Magnetic Field	3 T	3 T
Subjects scanned	Neonates	Neonates
#slices	~ 32	~ 34
Slice thickness	3 mm	3 mm
Matrix size	64 x 64	64 x 64
Voxel size	3 x 3 mm	3.125 x 3.125 mm
TR	3000 ms	2000 ms
TE	30 ms	35 ms
Flip angle	70˚	60˚

Two SE-EPI reversed phase encoding polarity containing only a few volumes could be performed to improve the distortion correction preprocessing step instead of using the GRE-EPI. This would allow a more accurate distortion correction as GRE-EPI is much more susceptible to signal dropouts than SE-EPI. However, this might increase scan time which is very limited.

Finally, multi-echo rs-fMRI could be employed to improve the denoising process as it helps determine whether the signal intensity changes in a voxel were produced due to a T2* variation or motion.

CHAPTER 6 ARTICLE 2: NEORS: A NEONATAL RESTING STATE FMRI DATA PREPROCESSING PIPELINE

Authors: V. Enguix[1,2,3*], J. Kenley[4], D. Luck,[1,3], J. Cohen-Adad[2,5,6], G.A. Lodygensky[1,3].

1. Department of Pediatrics, CHU Sainte-Justine, University of Montreal, Canada

2. NeuroPoly Lab, Institute of Biomedical Engineering, Polytechnique Montreal, Canada

3. Canadian Neonatal Brain Platform, Canada

4. Washington University School of Medicine, Saint Louis, USA

5. Functional Neuroimaging Unit, CRIUGM, University of Montreal, Montreal, QC, Canada

6. Mila – Quebec AI Institute, Montreal, QC, Canada

This article has been published in Frontiers in Neuroinformatics, 17 June 2022 (Enguix, Kenley, Luck, Cohen-Adad, & Lodygensky, 2022).

6.1 Abstract

Resting-state functional MRI (rs-fMRI) has been shown to be a promising tool to study intrinsic brain functional connectivity and assess its integrity in cerebral development. In neonates, where functional MRI is limited to very few paradigms, rs-fMRI was shown to be a relevant tool to explore regional interactions of brain networks. However, to identify the resting-state networks, data needs to be carefully processed to reduce artifacts compromising the interpretation of results. Because of the non-collaborative nature of the neonates, the differences in brain size and the reversed contrast compared to adults due to myelination, neonates can't be processed with the existing adult pipelines, as they are not adapted. Therefore, we developed NeoRS, a rs-fMRI pipeline for neonates. The pipeline relies on popular neuroimaging tools (FSL, AFNI, SPM) and is optimized for the neonatal brain. The main processing steps include image registration to an atlas,

skull stripping, tissue segmentation, slice timing and head motion correction and regression of confounds which compromise functional data interpretation. To address the specificity of neonatal brain imaging, particular attention was given to registration including neonatal atlas type and parameters, such as brain size variations, and contrast differences compared to adults. Furthermore, head motion was scrutinized, and motion management optimized, as it is a major issue when processing neonatal rs-fMRI data. The pipeline includes quality control using visual assessment checkpoints. To assess the effectiveness of NeoRS processing steps we used the neonatal data from the Baby Connectome Project dataset including a total of 10 neonates. NeoRS was designed to work on both multi-band and single-band acquisitions and is applicable on smaller datasets. NeoRS also includes popular functional connectivity analysis features such as seed-to-seed or seed-to-voxel correlations. Language, default mode, dorsal attention, visual, ventral attention, motor and fronto-parietal networks were evaluated. Topology found the different analyzed networks were in agreement with previously published studies in the neonate. NeoRS is coded in Matlab and allows parallel computing to reduce computational times; it is open-source and available on GitHub [https://github.com/venguix/NeoRS]. NeoRS allows robust image processing of the neonatal rs-fMRI data that can be readily customized to different datasets.

Keywords: Resting-state, fMRI, neonates, preprocessing, pipeline.

6.2 Introduction

The analysis of resting-state functional connectivity (RS-FC) constitutes a promising tool as it provides complementary information to structural imaging related to brain physiology. Indeed, since its discovery in 1995 (Biswal et al., 1995) rs-fMRI studies have provided new insights in the understanding of brain architecture and cerebral development (W. Gao et al., 2017; Grayson & Fair, 2017; Keunen et al., 2017; Power et al., 2010; Smyser & Neil, 2015; H. Zhang et al., 2019). Smyser et. al demonstrated the feasibility of using rs-fMRI to explore the alterations in resting-state networks (RSN) associated with preterm birth and white matter injury (Smyser et al., 2013). Alterations of the default mode and ventral attention networks at birth, are associated with behavioral inhibition at age of two years, (Sylvester et al., 2018) which suggests early alterations of the RSN present a correlation with clinical manifestations, and opens the opportunity of early diagnostics and treatment. Additionally, neonatal RSN are consistently identifiable and present

with high similarities to older populations (Fransson et al., 2009; Fransson et al., 2007; W. Gao et al., 2009). RS-FC is based on low frequency regional fluctuations (<0.1 Hz) in the Blood-Oxygen-Level-Dependent (BOLD) (Ogawa et al., 1990; Ogawa et al., 1993) signal while the participant is not performing any task, a useful feature when evaluating neonates (Smyser & Neil, 2015). RSN signal is very stable across subjects (Lee et al., 2013), but vulnerable to several artifacts such as head-motion (Maknojia et al., 2019), susceptibility distortions and or white matter (WM) and cerebrospinal fluid (CSF) signals (Jo et al., 2013; Power et al., 2014). Robust rs-fMRI data processing is key to reduce the nuisance effects of the non-neural signals in the data to identify reliable resting-state activity (Giove et al., 2009; Lund et al., 2006). Its clinical potential and implementation present several methodological challenges that need to be addressed before considering its use to develop a new generation of biomarkers. For this reason, straightforward to use and open-source tools for the neonatal rs-fMRI data processing need to be readily available. Tools for mature brains already exist to process rs-fMRI data, but analyzing the neonatal brain presents challenges that need to be addressed with new approaches (Smyser & Neil, 2015). There are several straightforward rs-fMRI data processing pipelines developed for adults such as Conn toolbox (Whitfield-Gabrieli & Nieto-Castanon, 2012),fmriprep (Esteban et al., 2019), the Human Connectome Pipeline (HCP) (Glasser et al., 2013), the Resting-state Analysis Toolkit (REST) (Rubinov & Sporns, 2010), or the Connectome Computation System (CCS) (Xu, Yang, Jiang, Xing, & Zuo, 2015), however, those are not adapted to the newborn brain which presents additional challenges, such as different contrast due to myelination (Enguix et al., 2018). T2-weighted images are usually needed for tissue segmentation in place of T1-weighted images. Further, varying brain sizes between subjects (Smyser & Neil, 2015) makes adult skull stripping less robust on the neonatal brain. Additionally, different age specific atlases and tissue probability maps are required for accurate segmentations, common space normalization and seed-based analysis.

To the best of our knowledge the only existing open-access pipeline to process neonatal rs-fMRI data is the one developed by the developing Human Connectome Project (dHCP) (Fitzgibbon et al., 2020). While this pipeline has proven to provide excellent results with the dHCP data, its implementation on smaller or clinical datasets remains challenging, as it requires large datasets for independent component (IC) denoising. Furthermore, the dHCP pipeline can be difficult to set up for cohorts acquired at other centers, because the pipeline was developed/optimized from the dHCP database specifically. For example, the dHCP denoising step is based on spatial independent

component analysis (sICA), which separates independent correlating signals that can be classified as neural or non-neural signal. This denoising technique has been shown to provide superior results in adults and infants when the dimensionality is accurately set (Alfaro-Almagro et al., 2018; Griffanti et al., 2017). However, the identified signals need to be classified as neural signal or structured noise, which in most cases is performed manually and a difficult process to automate. To overcome this limitation, the dHCP pipeline uses a machine learning approach (ICA-based Xnoiseifier) (Salimi-Khorshidi et al., 2014) to classify the independent components as neural signals or noise. The machine learning algorithm requires a minimum of 35 manually labelled subjects to be trained, which is not always possible in smaller cohorts and requires specialists to manually classify the independent components (Fitzgibbon et al., 2020).

To overcome the aforementioned challenges, we developed NeoRS, with the goal of creating a robust open-source pipeline containing the necessary tools to preprocess rs-fMRI data. The main advantages of NeoRS are it has been developed specifically for neonates, simple to implement and flexible to process different datasets. Additionally, it can process single subject data, utilizes parallelizable environment and includes visual quality control checkpoints at each step.

The data processing steps include T2-weighted image alignment to a common space, slice timing correction and segmentation, and rs-fMRI procedures are slice timing, distortion correction using reversed phase encoding polarity acquisitions, alignment in a common space, motion correction, removal of nuisance confounds and noise compromising functional data interpretation. Further, simple resting-state functional connectivity cross-correlations based on seed-to-voxel and seed-to-seed approaches are incorporated.

6.3 Materials and Methods

6.3.1 Data

NeoRS has been evaluated on neonates (7+/-1.4 weeks old) from the *Baby Connectome Project (BCP)* (Howell et al., 2019) dataset. For this study only participants scanned at 9 weeks old or less and contained T2-weighted images and rs-fMRI were used (N=10). Participants were naturally sleeping and were scanned on a 3.0 T MRI Prisma from Siemens using a 32-channel head coil. This study included a T2-weighted structural image (TE = 564 ms, TR = 3200 ms, matrix=320x320 mm, FOV = 256x256 mm, resolution = 0.8 x 0.8 x 0.8 mm, flip angle = variable, in-plane

acceleration factor=2, acquisition time = 5 min 57 s), two gradient-echo (GRE) echo-planar imaging (EPI) blip-up/blip-down (TE =37 ms, TR=800 ms, matrix=104x91 mm, FOV = 208x182 mm, resolution = 2x2x2 mm, flip angle = 52°, multi-band acceleration factor=8, acquisition time = 5 min 47 s, 420 volumes), and two spin-echo (SE) EPI blip-up/blip-down for distortion correction purpose (TE =66 ms, TR=8000 ms, matrix=104x91 mm, FOV = 208x182 mm, resolution = 2x2x2 mm, flip angle = 52°, multi-band acceleration factor=1, acquisition time = 33 s, 3 volumes).

6.3.2 Data structure

To facilitate collaborations, NeoRS uses the Brain Imaging Data Structure (BIDS) format as described in https://bids.neuroimaging.io/. See (Figure 6.1) for an example of data naming and organization for NeoRS.

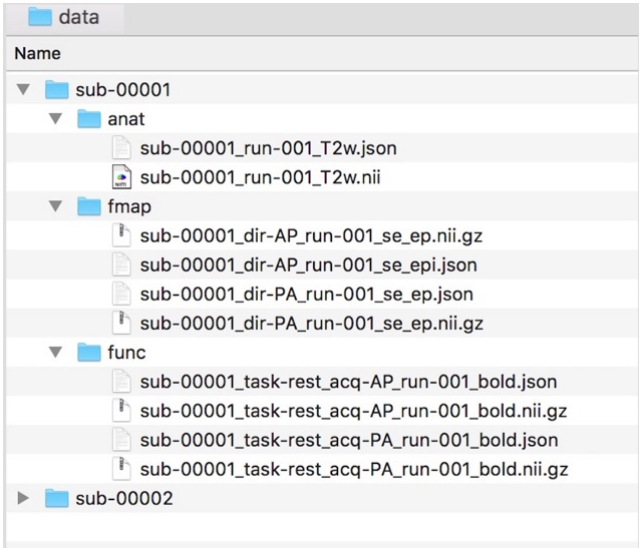

Figure 6.1. Example of data naming and organization for NeoRS.

6.3.3 Pipeline overview

NeoRS is a neonatal rs-fMRI data processing pipeline developed on Matlab and calls for commands developed on well-known open-source neuroimaging tools, such as FSL 6.0.3.1 (Jenkinson et al., 2012; Smith et al., 2004; Woolrich et al., 2009), AFNI 20.2.10 (Cox, 1996) and SPM 12 (https://www.fil.ion.ucl.ac.uk/spm/). It runs on both MacOS and Linux operating systems. NeoRS

has been tested on a MacBook pro 2015 with operating system High Sierra and on a Linux computer using Ubuntu 18.04.5 by running the pipeline from the beginning to end on different subjects on both computers. NeoRS is built to accommodate MRI data acquired with different manufacturers. The pipeline was tested using the aforementioned BCP data, as well as the not publicly available data from CHU Sainte-Justine acquired on a GE 3T MR750, but this manuscript focuses only on BCP results. Furthermore, the pipeline has single subject capabilities. NeoRS has been developed to accommodate a parallelizable environment, allowing several subjects to be simultaneously processed depending on the number of selected cores. To investigate, two subjects were processed on an early 2015 MacBook pro with 2.7 GHz Intel Core i5 processor and 8 GB 1867 MHz DDR3 memory by using a single core vs 2 parallel cores and found a reduction of computing time of 1.8 times when using the 2 parallel cores. This function is optional and requires the Matlab parallel toolbox.

See NeoRS workflow in (Figure 6.2).

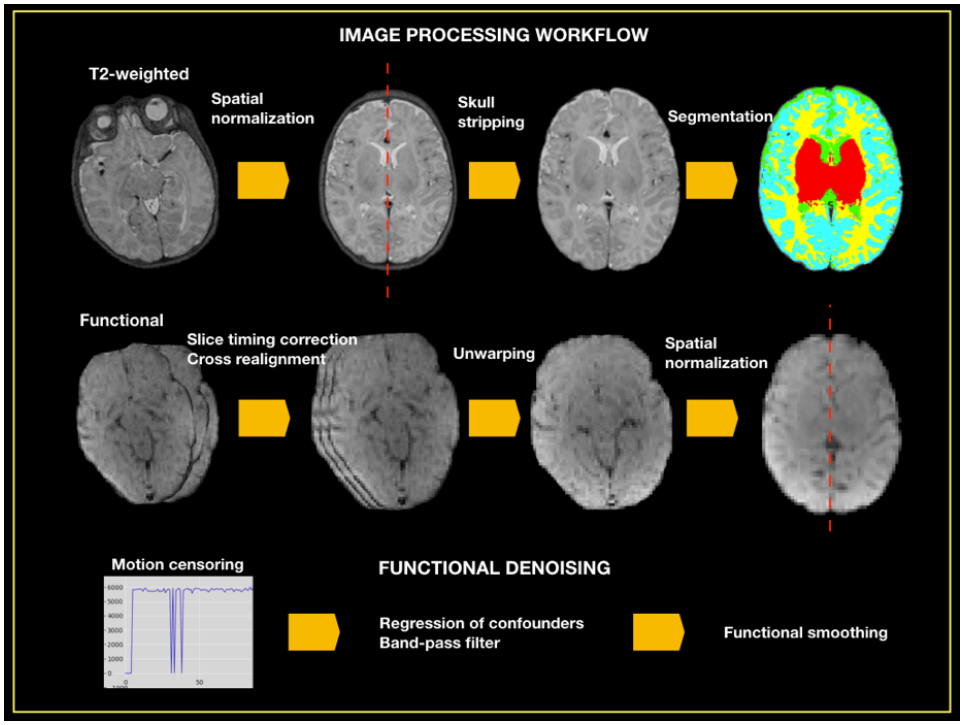

Figure 6.2. NeoRS workflow for neonatal resting-state functional connectivity processing and denoising.

To ensure images align to the orientation of the standard template a reorientation to standard is performed in both structural and functional data prior to other data processing procedures by employing fslreorient2std from FSL. Furthermore, to guarantee the accurate performance of NeoRS, output files for each processing step are saved in a folder called Output_files. Processing steps are dependent from previous outputs and should be inspected carefully. In case of fail, the user can parameterize the specific function, as specified later on. Various operations are not mandatory, such as slice-timing correction or distortion correction, and can be manually turned-off by setting the function parameter to 0 in the main file. See (Figure 6.3) for an example of inputs configuration.

```
%% INPUTS %%%%%%%%%%%%%%%%%%%%%%%%%%%%%%%%%%%%%%%%%%%%%%%%%%%%%%%%%%%%%%
%%%%%%%%%%%%%%%%%%%%%%%%%%%%%%%%%%%%%%%%%%%%%%%%%%%%%%%%%%%%%%%%%%%%%%%%
% Activate or deactivate functions: 1=On; 0=Off
options.slicetimingcorrection=1; %Slice timing correction
options.fmap = 0; %Functional distortion correction
options.FDaverage = 1;

%Inputs definition
workingDir=('/Desktop/Data');%Data directory
options.TR=3;%Repetition time of the RS sequence in seconds
options.motion=12; %Number of motion parameters-> 6,12 or 24
options.slice_order=5;%1: bottom up, 2: top down, 3: interleaved+bottom up
% 4: interleaved+top down, 5:automatically read json file
options.FWHM=6; %FWMH for functional gaussian smoothing
options.radius=35; %Head radius
options.FD_max=0.25; % Framewise displacement threshold
options.BPF=[0.01,0.1]; %Band-pass filter frequencies in Hz
options.n_core=2; %Number of cores for parallel computing
```

Figure 6.3. Example of NeoRS input parameters.

6.4 Data Processing

6.4.1 Structural

6.4.1.1 T2-weighted Image Registration

NeoRS uses the term age stereotaxic space (Smyser et al., 2010) from Washington University – School of Medicine. The template is available in Talairach space (Talairach, 1988) 1mm and 3mm isotropic resolutions. Image registration in NeoRS is performed using FSL *flirt* and is implemented in a single step with 12 degrees of freedom and *not* applying the resampling blur when down

sampling. These parameters can be modified by the user in the function *anat2std.m*. High resolution T2-weighted images are registered to a 1mm and 3 mm isotropic template.

6.4.1.2 Skull Stripping

Skull stripping plays an important role in image processing, as it is mandatory for different processing functionalities, such as tissue segmentation, and requires special attention to avoid further complications in the process. NeoRS skull stripping step utilizes the FSL (Jenkinson et al., 2012) function *bet2* and has been optimized for term neonatal brains. Skull stripping is performed after image registration to obtain consistent results independent of brain size. Furthermore, visual quality control is available in a file containing the brain with the skull and the overlay of the contour of the intracranial cavity. If the user is not satisfied with the results, modify the fractional intensity threshold, "-f", and vertical gradient in fractional intensity threshold, "-g", to properly adjust skull stripping in the Matlab function *skull_stripping.m*.

6.4.1.3 Segmentation

Extracted T2-weighted intracranial content is then segmented to create different tissue probability maps corresponding to each brain structure. Tissue segmentation is crucial in image processing as the outputs will be used for regression of confounds. For brain segmentation NeoRS applies *Morphologically Adaptive Neonatal Tissue Segmentation: Mantis* (Beare et al., 2016). *Mantis* is an SPM based toolbox and allows T2-weighted image segmentation based on template adaptation via topological filters and morphological segmentation tools, resulting in eight different tissue probability maps. The segmentation process is fully integrated in the NeoRS pipeline and has been tested on three different datasets (BCP, and CHU Sainte-Justine). After segmentation, the eight tissue probability maps are automatically combined, thresholded and binarized to create three different binary masks needed to run downstream processing. The masks correspond to white matter (WM), grey matter (GM) and cerebrospinal fluid (CSF). The masks are resampled to 3-mm isotropic to match functional image space resolution.

6.4.2 Functional

6.4.2.1 Slice Timing Correction

A common acquisition technique for rs-fMRI is the single-shot Gradient-Echo (GRE) Echo-Planar Imaging (EPI). In this acquisition sequence, slices are acquired at varying intervals, which need to be addressed. The NeoRS function for slice timing correction is FSL *slicetimer* and can automatically read the slice order from the .json file, if available. If the .json file is not available, the user can manually define the slice order or use one of the predefined options from fsl (i.e: interleaved ascending) in the configuration file.

6.4.2.2 Functional Cross Realignment

To correct for head movement, it is necessary to obtain a motion estimation based on 6 movement parameters (three rotation and 3 translation parameters). This is done by rigid-body registration (6 degrees of freedom) between the different volumes with respect to a reference, in NeoRS, the reference is the first volume from the rs-fMRI, but can be easily altered by the user if desired. This NeoRS function is performed using FSL *mcflirt* (Jenkinson, Bannister, Brady, & Smith, 2002) and works the same as for adults, however we set the smoothness level to 0, as smoothing occurs later in the pipeline, and used sinc interpolation. Parameters for cross realignment can be customized in the Matlab function *cross_realign2.m*. For quality control purposes, NeoRS creates a .png file where the total rotations, translations and framewise displacement (FD) for each volume can be evaluated. Framewise displacement is calculated as previously described by Power et al.(Power et al., 2012). To take into account head size differences, the calculations were done using a 35 mm radius sphere instead of 50 mm which approximately corresponds to the mean distance from the cerebral cortex to the center of the head in neonates. After motion correction, the motion parameters are saved in a text file that will be further used for denoising purposes.

6.4.2.3 Functional Best Resting-state Section Selection

NeoRS incorporates the possibility to analyze sub sections of long time series (i.e 20 minutes). This tool is deactivated by default but can be activated by setting options.best_volumes = 1 in the configuration file. The sectional analysis tool automatically identifies a section of the time-series (i.e 5 minutes) with the lowest average FD, which is recommended to use on very long acquisitions

that present a higher average FD than the threshold. The length of the section can be modified by the user, but it is recommended the duration remain above five minutes (Sylvester et al., 2018). To note, the average FD threshold has a default of 0.25mm, but can also be tailored as needed by altering options.FDaverage in the configuration file. NeoRS chooses only the best sections of the time-series, which reduces computational times drastically.

6.4.2.4 Functional Distortion Correction

The EPI sequence is considerably sensitive to off-resonance fields due to susceptibility variations of participants. To address these distortions a typical approach is to use two SE-EPI reversed polarity acquisitions (reversed phase encoding direction) to estimate the distortion field. This field is implemented to correct for distortions in the original GRE EPI images. Directly using two reversed polarity GRE EPI to estimate the distortion field instead of two reversed polarity SE EPI is possible, but not recommended because GRE-EPI sequences are hampered by signal dropouts caused by intravoxel dephasing. Providing reversed phase encoding polarity SE EPI images and activating the distortion correction option (options.fmap=1) in NeoRS, allows users to estimate these distortions utilizing FSL *topup (J. L. Andersson, Skare, & Ashburner, 2003; Graham, Drobnjak, Jenkinson, & Zhang, 2017; Smith et al., 2004)*. Such as specified in the *topup* documentation, a text file containing the encoding directions and total readout time needs to be included in the fmap folder to perform distortion corrections. If the .json file is found in the fmap folder, the text file will be automatically created by NeoRS. Distortion estimates are rectified with FSL *applytopup* for each EPI volume by applying the output from *topup*.

6.4.2.5 Functional Image Registration

Functional images are registered to the same stereotaxic space template from the Washington University – School of Medicine as the T2-weighted image registration procedure. Initially, a two-step registration was performed. First, a rigid body registration between the mean rs-fMRI volume and T2-weighted images was calculated, followed by affine transformation between T2-weighted and the template. Finally, the output affine transformation matrices from each process were applied to the rs-fMRI images to align to the 3 mm isotropic template. Additionally, a single step registration approach was investigated, where the rs-fMRI images were aligned directly to the 3 mm isotropic template using 12 degrees of freedom. This registration approach was comparable to the 2-step registration process and was chosen as it was accurate and faster. Down-sampling blur,

by default is set to off in NeoRS, however, if needed, the parameters can be customized in the Matlab function *epi2std2.m.*

6.4.3 Denoising

6.4.3.1 Motion Censoring

Before the regression of the confounding signals, volumes with excessive motion are removed based on the framewise displacement metric described by Power et al (Power et al., 2012). NeoRS performs linear detrending and computes framewise displacement after functional cross realignment based on 6 motion parameters in radians (3 rotation parameters + 3 translation parameters). This step also automatically removes the first five volumes.

$$FD = |rot\_x| + |rot\_y| + |rot\_z| + |trans\_x| + |trans\_y| + |trans\_z|$$

Where rot_x/rot_y/rot_z are rotations converted from radians to mm and trans_x/trans_y/trans_z are translations in mm. Once the FD is computed, a text file containing the information of volumes exceeding the FD threshold plus the first 5 frames, is created and head motion plots are saved and can be reviewed. The FD threshold is automatically set to FD < 0.25 mm (Smyser et al., 2016), so volumes with FD higher than or equal to 0.25 mm are excluded. Excluded volumes are set to zero value and no interpolation is applied to avoid artificial correlations.

6.4.3.2 High Motion Subjects

High motion acquisitions are source of artifacts and may confound neural correlations with non-neural signals. Apart from single frame motion censoring based on FD NeoRS evaluates the average FD for every BOLD run. By default, NeoRS was set to discard acquisitions with an average FD higher than 0.25 mm. The average FD threshold can be altered in the configuration file by defining options.FDaverage.

6.4.3.3 Regression of Confounds

Variables identified as potential confounders of the estimated BOLD signal are merged in a single file. To avoid frequency mismatch in the regression process, the file is used to compute linear regression in a single step with frequency filtering. This process is performed utilizing AFNI *3dTproject.*

6.4.3.4 Motion Parameters

Head motion is considered as a rigid body moving in a 3D space with 6 degrees of freedom. In cartesian coordinates we can describe it with 3 translations x- (left/right), y- (anterior/posterior), and z-axes (inferior/superior), and 3 rotations around the x-axis (pitch), y-axis (yaw), and z-axis (roll). To address the residual motion related signal variance after a suboptimal rigid body registration, NeoRS uses a linear regression strategy based on the 6 aforementioned estimated motion parameters. Those parameters are considered as nuisance effects of the signal and are then removed. NeoRS allows various options including: 6 motion parameters, 12 (including temporal derivatives)(Power et al., 2012) or 24 (including temporal derivatives and their squares) (Friston et al., 1996) which can be defined in the configuration file parameter options.motion.

6.4.3.5 White Matter, Cerebrospinal Fluid and Global Signals

White matter and cerebrospinal fluid signals are highly confounding and need to be removed from the rs-fMRI (Smyser et al., 2016). Signals for regression of confounds are extracted from the WM and CSF masks generated previously in the pipeline from the segmentation. Masks are created in a conservative way by selecting voxels from the tissue probability masks with higher probability than 0.5. The voxels of the white matter are eroded by one voxel to ensure the mask doesn't include any gray matter. Two files containing the average signal of the WM and CSF masks are created. Finally, global signal is approximated by averaging the signal in a gray matter mask (Vos de Wael, Hyder, & Thompson, 2017) and used by default in NeoRS, as it improves data quality by reducing motion artifacts (cardiac, respiration, head motion) (Smyser et al., 2016).

6.4.3.6 Frequency Filter

Temporal frequencies outside the frequency range of [0.01 - 0.1] Hz are removed from the BOLD signal to correct for slow frequency drifts, reduce motion artifacts and other physiological noises while preserving the frequencies of resting-state networks (Power et al., 2014). The use of a low-pass filter could drastically reduce the degrees of freedom of the time series in acquisitions with very short TR. For those cases, it is recommend to set the value of options.BPF=[HPH, LPF], to [0.01, 999] in the configuration file.

6.4.4 Smoothing

6.4.4.1 Functional Smoothing

Functional smoothing is the last processing procedure. After denoising the rs-fMRI signal is convolved with a gaussian kernel. This reduces the effect of misregistration between functional regions and slightly increases the signal to noise ratio. Gaussian smoothing is performed implementing *fslmaths* from FSL. The size of the gaussian kernel is customizable in the NeoRS pipeline by modifying options.fwhm in the configuration file, which is 6 mm by default.

6.5 Data Analysis - Functional Connectivity

Prior to further data analysis, like ROI to ROI (region of interest) correlations, all the processed BOLD runs are merged together into a single 4D-file. NeoRS offers basic single subject data analysis, including seed based and seed to seed correlations, so the user can further assess data has been correctly processed.

6.5.1 Seed-Based Correlations (SBC)

Seed-based functional connectivity identifies correlation between a defined ROI, also called a seed, and the rest of the brain. This metric facilitates the observation of simultaneously activated regions with the pre-defined ROI. The NeoRS pipeline provides 31 template seeds representing some of the most common resting-state networks including: language, default mode, dorsal attention, visual, ventral attention, motor and fronto-parietal networks. An excel file (*Perceptron_ROI_list.xlsx*) can be found in the documentation with all the information related to seed positioning (Smyser et al., 2016).

6.5.1.1 Seed-to-seed measurements

Seed-to-seed data analysis provides measurements of functional connectivity between all the different pairs of seeds demonstrating a more global perspective about networks compared to seed-based functional connectivity. NeoRS performs Pearson correlation between the different ROIs to create a correlation matrix.

6.6 Results

6.6.1 Image Registration

Image registration results of the T2-weighted and BOLD images to the template for a representative subject are demonstrated in Figure 6.4, an example of a user checkpoint. Yellow lines represent the segmented cerebrospinal fluid and is added as an overlay to the T2-weighted images, BOLD and template. After visual inspection, a correct alignment within the template for both registrations were observed for each test participant.

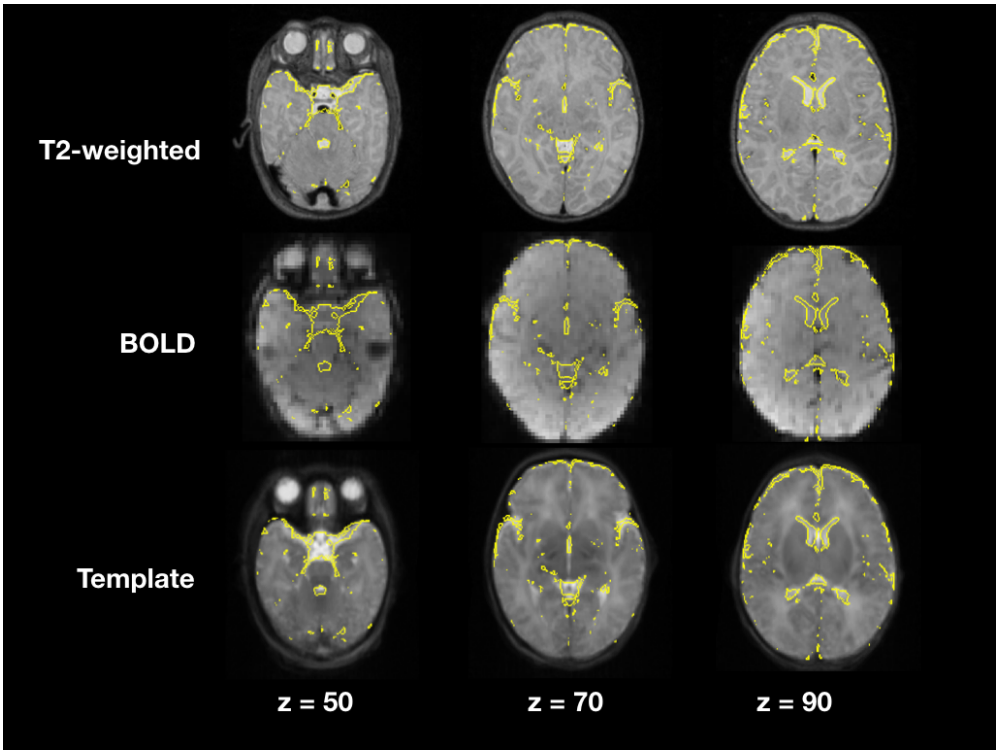

Figure 6.4. T2-weighted and BOLD image registration to stereotaxic space.

When comparing single step registration versus a 2-step registration approach for rs-fMRI there were no discernible differences between both registrations and final functional connectivity results presented the same correlation strengths and topology. The main difference between the two approaches was computational times, which were higher for the 2-step registration method.

6.6.2 Skull stripping

Figure 6.5 illustrates the default skull stripping segmentations versus NeoRS adapted parameters for neonates. With the default settings we observed skull stripping was failing for some of the subjects with different brain sizes, in contrast, when using NeoRS parameters, skull stripping remained robust for all the processed subjects.

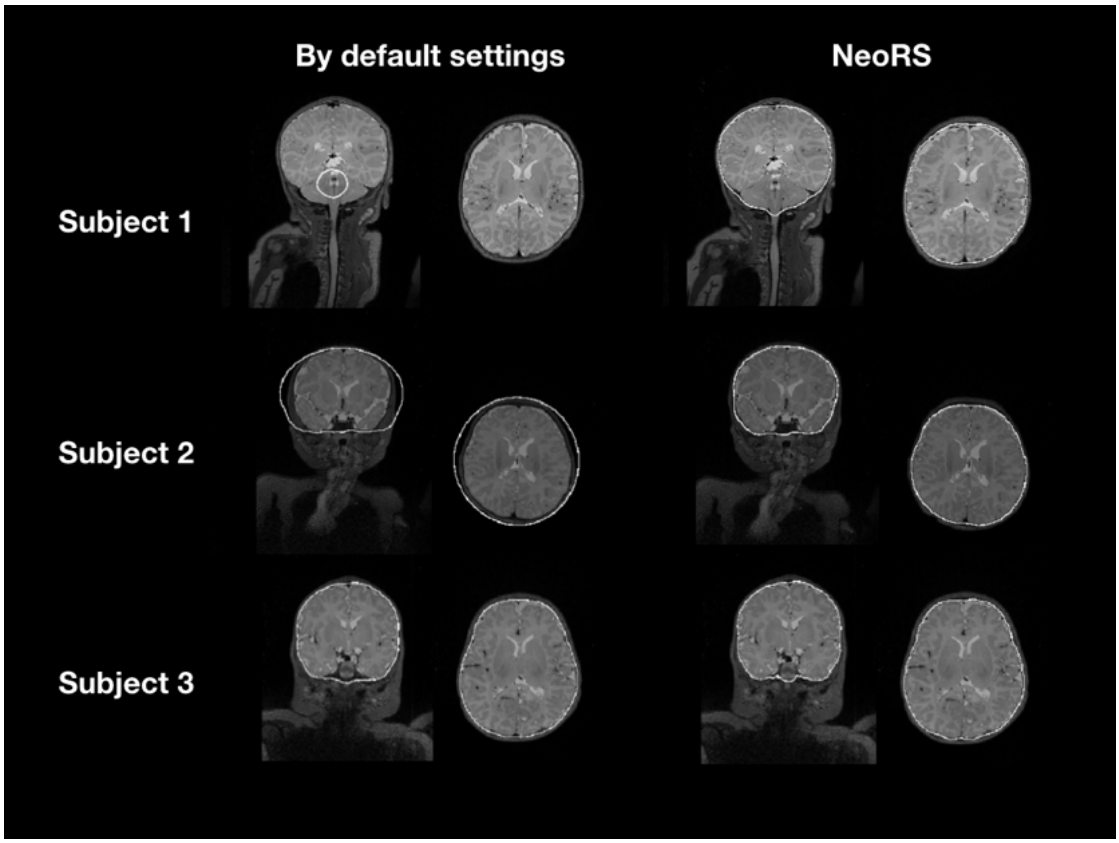

Figure 6.5. Skull stripping parameters comparing default bet2 settings in neonates and NeoRS settings optimized for neonates.

6.6.3 Segmentation and Mask Creation

Figure 6.6 displays the 1 mm isotropic binary masks created by NeoRS from Mantis tissue probability maps. The output contains three different binary files corresponding to white matter,

cerebrospinal fluid and gray matter. Figure 6.7 demonstrates the 3 mm isotropic masks for the regression of confounds process.

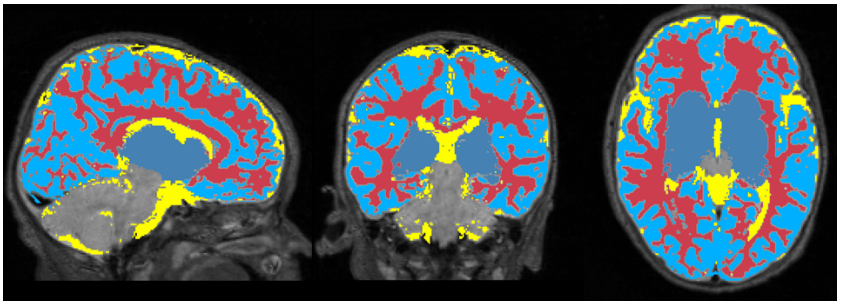

Figure 6.6. One millimeter isotropic masks created from the tissue probability maps obtained with Mantis. White matter (red), CSF (yellow), gray matter (blue).

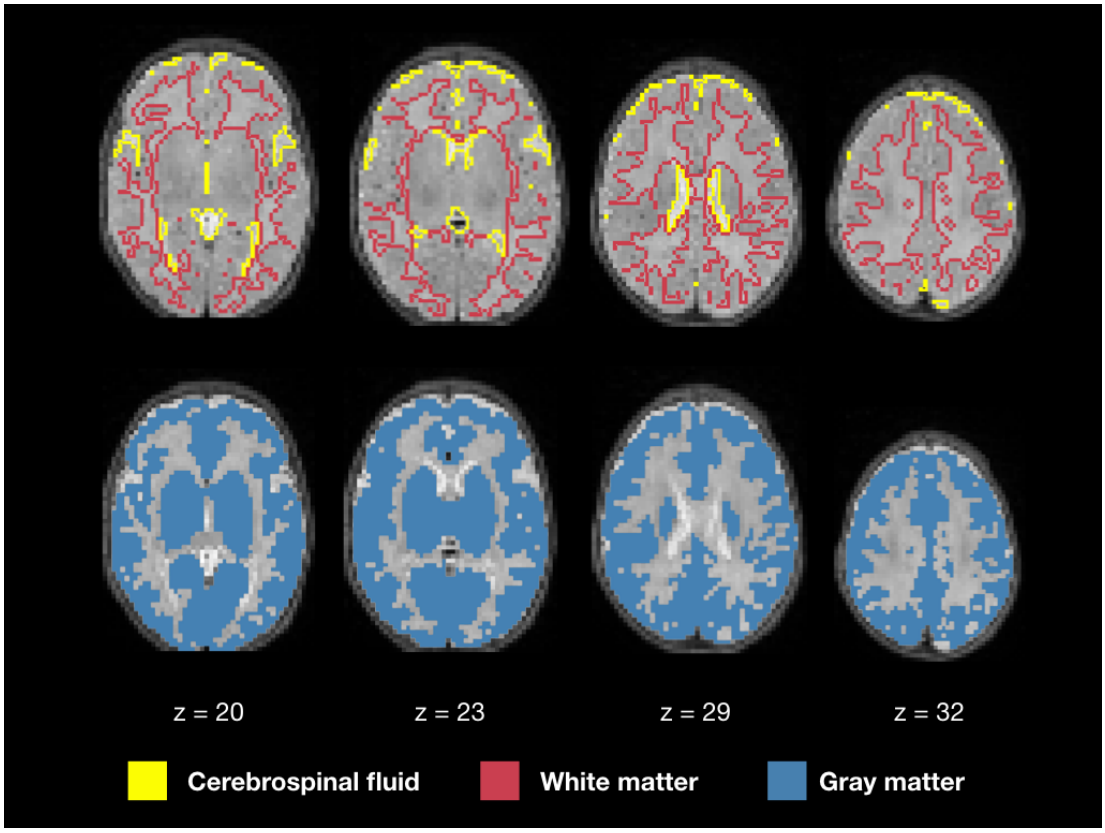

Figure 6.7. White matter, cerebrospinal fluid, and gray matter masks for regression of confounds.

6.6.4 Functional Distortion Correction

Functional susceptibility-induced magnetic field inhomogeneity correction for a representative subject is shown in Figure 6.8. GRE EPI images, independent of brain size are distorted in the phase encoding direction whether they are acquired AP or PA but present those distortions in both areas of the brain. After susceptibility-induced magnetic field inhomogeneity distortion correction, the two acquisitions (AP and PA) present a similar morphology and a more accurate brain shape with respect to the undistorted T2-weighted image.

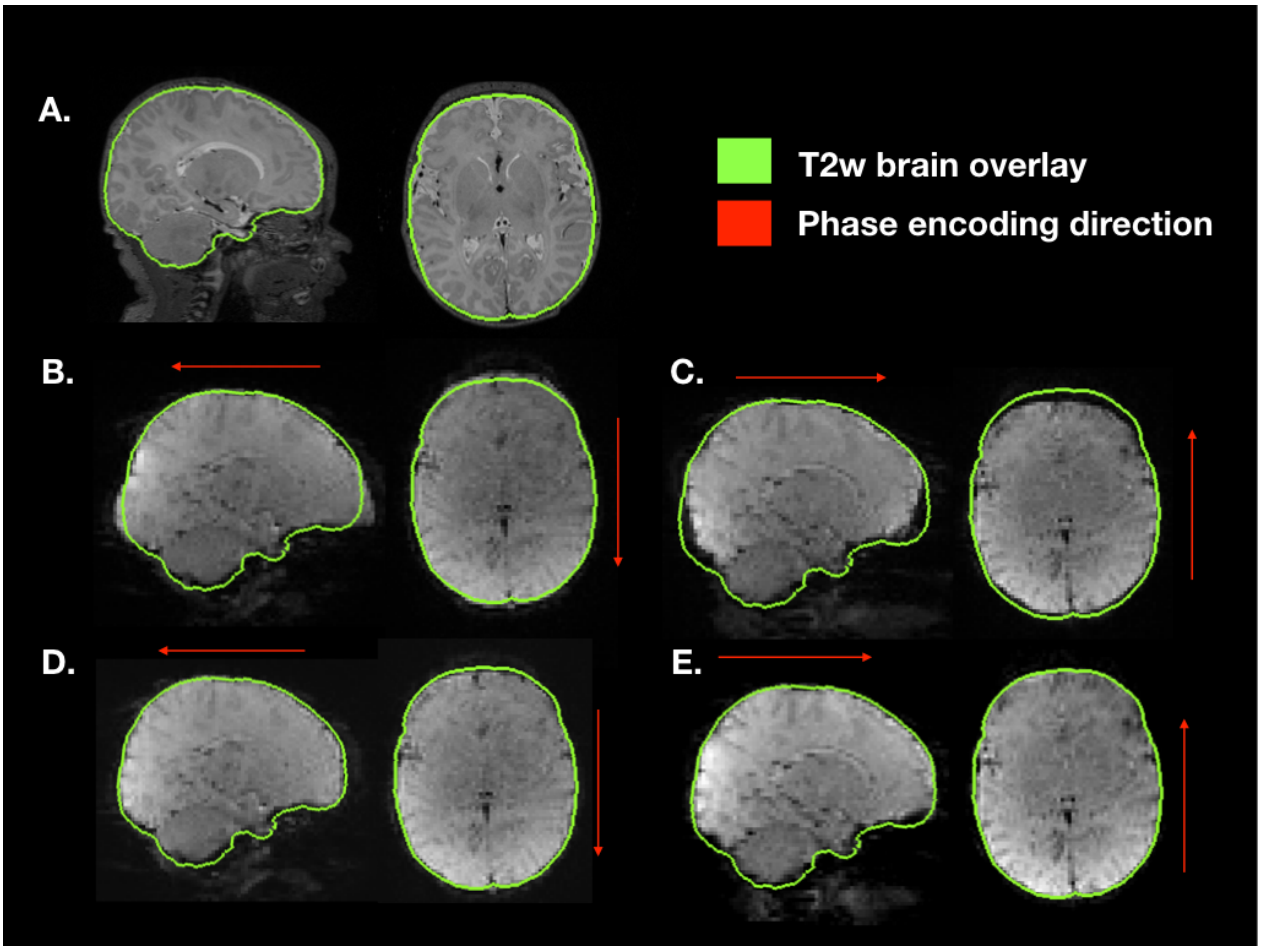

Figure 6.8. Susceptibility-induced magnetic field inhomogeneity causing geometric distortions along the phase encoding direction.

(A) Original T2-weighted image without distortion, shown as reference; (B) original GRE-EPI acquired in anterior-posterior phase encoding direction (AP); (C) original GRE-EPI acquired in

posterior-anterior phase encoding direction (PA); (D) corrected GRE-EPI AP; (E) corrected GRE EPI PA.

6.6.5 Head Motion

After functional cross-realignment, an output graph is provided by NeoRS containing information concerning rotations and translations applied to cross-realign for each volume of the rs-fMRI, as well as the computed framewise displacement (Figure 6.9).

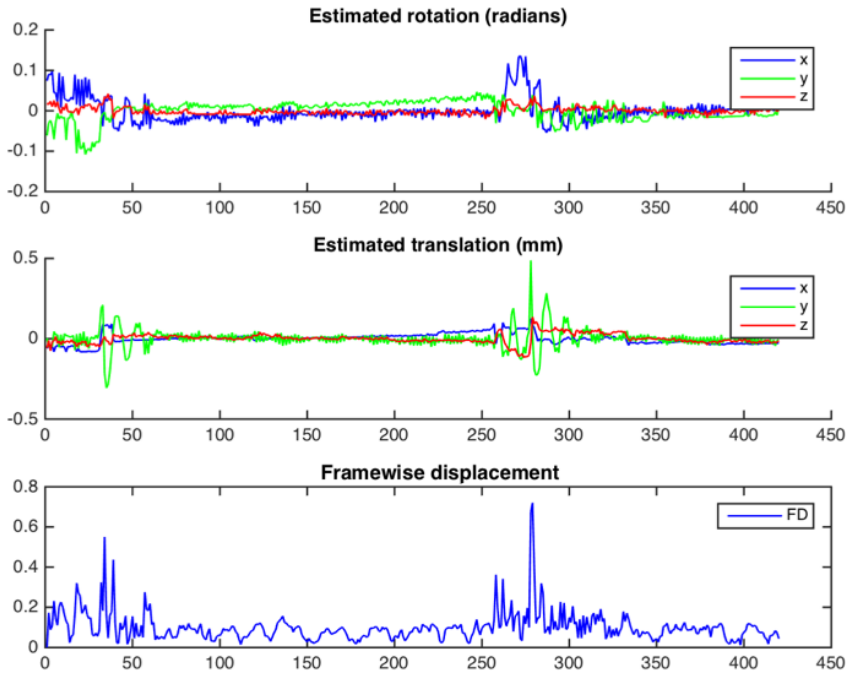

Figure 6.9. Example of head motion plots from a single subject. Plots are generated for each bold run and contain three different graphs per run.

Figure 6.10 is an example of a single subject with 2 different rs-fMRI acquisitions with different amounts of motion. In the seed-based functional connectivity results of the motor network, the correlation differences between an acquisition with an average framewise displacement higher than 0.25 mm (run 1) and an acquisition with an average framewise displacement lower than 0.25 mm

(run 2). High motion acquisition presented increased amounts of noise and the network topology was difficult to identify.

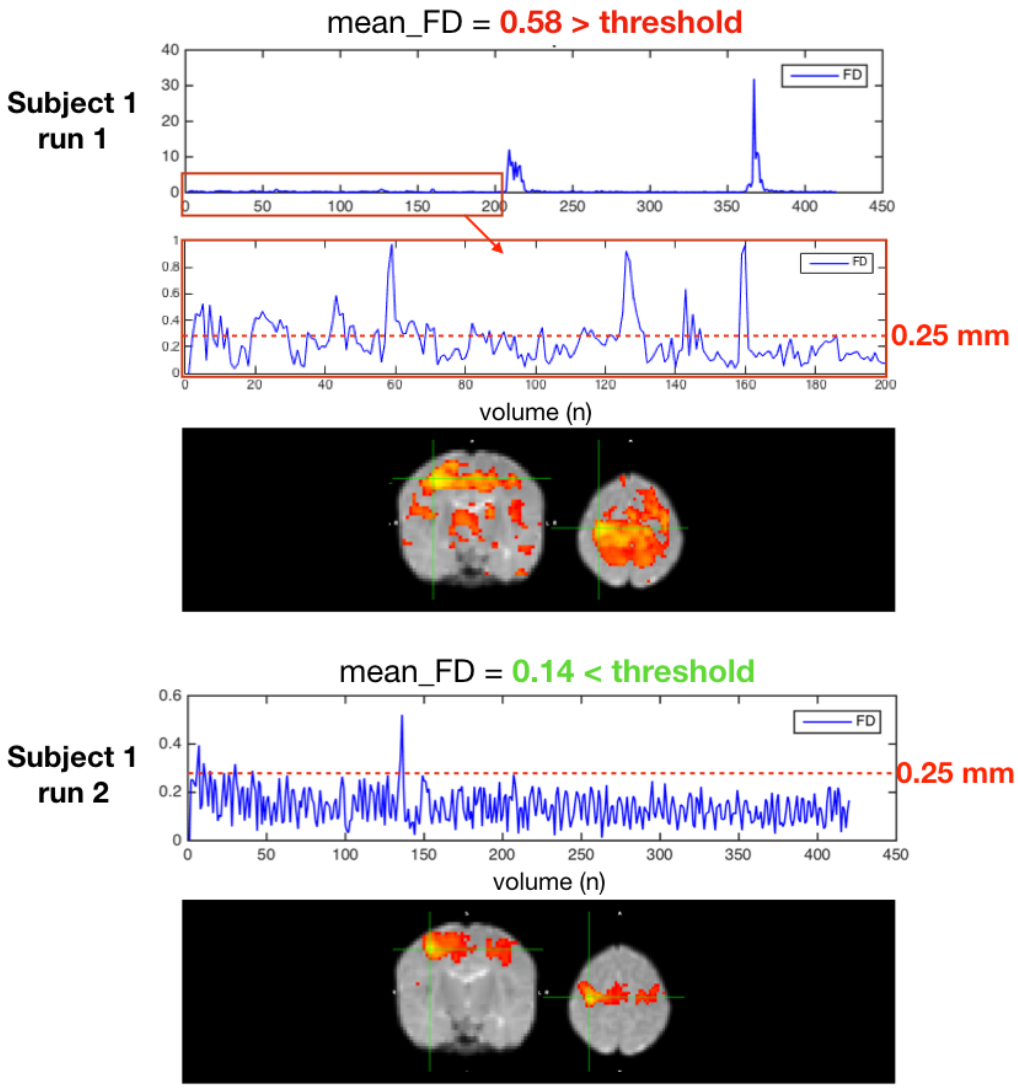

Figure 6.10. Two acquisitions of a high motion subject, run 1 excluded for having an average FD 0.25 mm, run 2 kept with an average FD < 0.25 mm.

6.6.6 Resting-state Networks - Seed-Based Correlations

Figure 6.11 illustrates, seven of the most common resting-state networks after NeoRS processing employing a seed-based correlation approach.

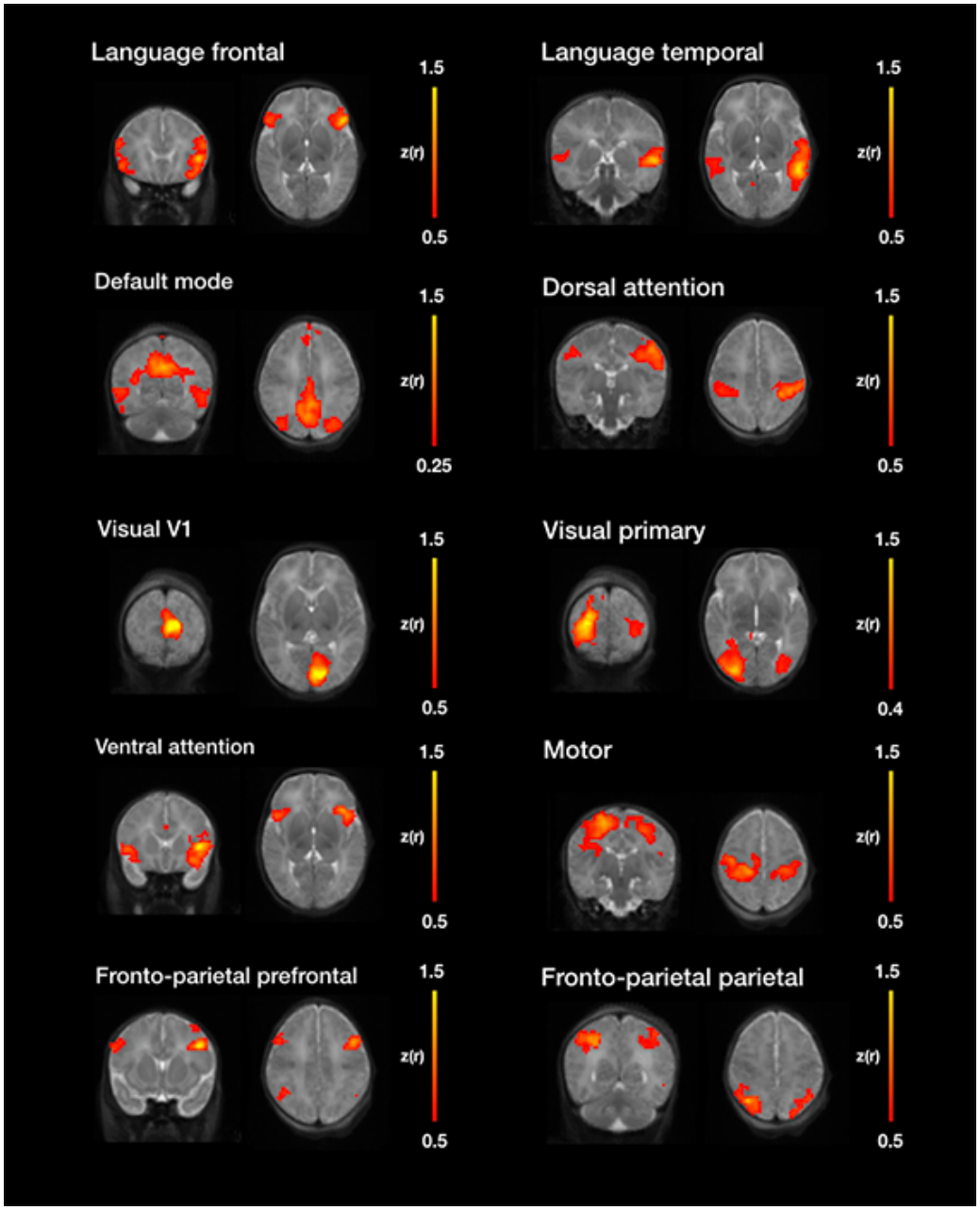

Figure 6.11. Example resting-state networks obtained by seed-based functional connectivity after image processing with NeoRS.

Figure 6.12 is a single subject example of the 31 seeds included in NeoRS.

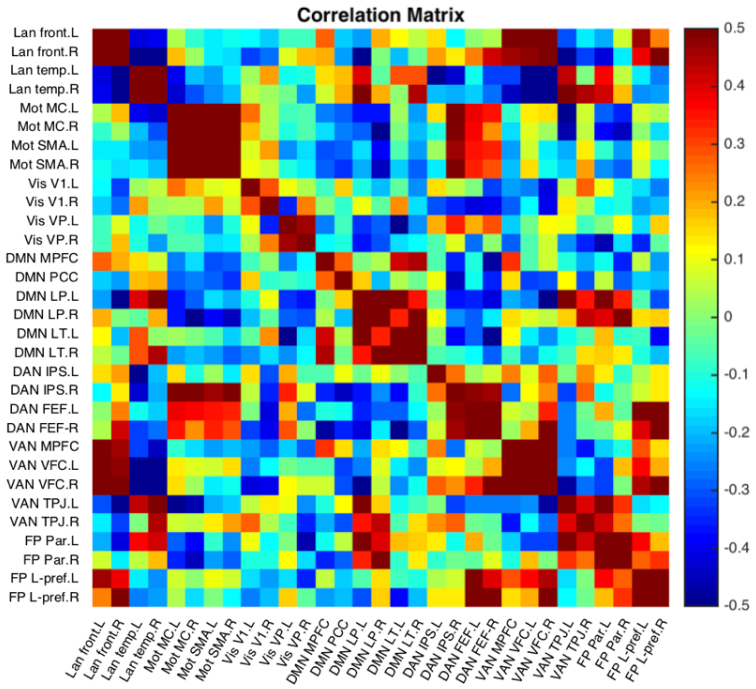

Figure 6.12. Representative subject resting-state network example seed-to-seed functional connectivity correlations.

6.7 Discussion

NeoRS is an open-source image processing pipeline dedicated to neonatal rs-fMRI. It includes seed-based and seed-to-seed 1st level analysis. NeoRS has neonatal brain templates for term in 1mm and 3mm Talairach space, as well as a set of 31 seed regions defining seven common resting-state networks. NeoRS relies on the open-source neuroimaging pipelines: SPM, FSL and AFNI and encompasses robust methods to segment, register and denoise neonatal rs-fMRI data. Each of the various processing steps were evaluated separately. Output was carefully inspected to ensure the best quality products, by optimizing skull stripping, image registration, head motion and denoising related results. Additionally, functional connectivity of the motor, visual, default mode, language, dorsal attention, ventral attention and fronto-parietal networks using seed-based functional connectivity analysis were demonstrated.

Image registration to the atlas was meticulously inspected for every subject and no significant misalignments were observed for T2-weighted or rs-fMRI images for affine registration. We compared single step to two-step registration for accuracy and computational times. The single step registration was chosen, as this process required less computational time and demonstrated no substantial variation when compared to the two-step counterpart.

In contrast with some of the most common adult pipelines, image registration is implemented prior to skull stripping, as alignment quality results were identical. Further, performing image registration preceding skull stripping produced vastly robust skull stripping results across varying brain sizes. This was not the case employing traditional skull stripping before image registration. Skull stripping of the T2-weighted images was found to be a crucial step when working with neonates because poor stripping lead to misclassification of segmented data and ultimately unreliable representation of RSN because of misregistrations. Additionally, image registration prior to skull stripping facilitated brain extraction without any user intervention. Furthermore, if the brain was previously aligned to an atlas, *bet2* was implemented on the subject specific atlas aligned data instead of applying an atlas brain mask to avoid subtle geometric inaccuracies. This procedure is critical and needs to be properly assessed. For this reason, an output for the skull stripping is provided which contains the image of the non-skull stripped mask with an overlay of the contour of the skull stripped brain.

After skull stripping, tissue segmentation is performed using *Mantis*, without the need of any further intervention. Mantis is integrated into the NeoRS pipeline as it provided robust results for disparate brain sizes using only T2-weighted images. Contrary to the adult brain that uses T1-weighted images for brain segmentation, it is fundamental in neonates to provide the pipeline with T2-weighted images as the water/cholesterol ratio is reversed with respect to adults due to lack of myelination. Neonatal T2-weighted images present a better contrast between brain structures (McArdle et al., 1987). While Mantis needs to be installed to use the NeoRS pipeline, no additional setup steps are required as it is fully assimilated in NeoRS. The results showed the binary masks created from *Mantis* tissue probability maps are perfectly aligned with their corresponding structures for various subjects without any manual intervention.

It is well known the GRE-EPI sequence for rs-fMRI is prone to susceptibility-induced magnetic field inhomogeneity (Czervionke et al., 1988). The artifact primarily appears close to the extrema

portions of the brain in the phase encoding direction (J. L. R. Andersson, Graham, Drobnjak, Zhang, & Campbell, 2018) and needs to be properly corrected. While several methods have been successfully used in these settings (Cusack, Brett, & Osswald, 2003; Jezzard & Balaban, 1995), NeoRS operates the standard *topup/applytopup* method. Two reversed phase encoding direction images are involved to correct for the deformations. (Holland, Kuperman, & Dale, 2010) The method is simple to implement in the acquisition protocol, provides high quality results and acquisition sequences require very short duration times.

Slice timing correction remains a controversial step when a very short repetition time (TR) is deployed (Parker & Razlighi, 2019). However, as it has been shown it can significantly improve z-scores (Parker & Razlighi, 2019) and as the aim was to make NeoRS work with the maximum number of datasets, it is included as an option. Slice timing correction can be deactivated for multi-band sequences with very low TR, as in this kind of low TR sequence, all slices in each volume are acquired very closer together (Glasser et al., 2013).

After data preprocessing, confounding signals and motion effects are removed. First, the framewise displacement threshold is defined as 0.25 mm, as performed by Smyser et al. on their neonatal study and shown to provide accurate results (Sylvester et al., 2018). Volumes with FD higher than 0.25 mm were removed from the time-series as described per Power et al.(Power et al., 2012). Motion censoring was performed prior to filtering to prevent spikes from passing through band-pass filtering, as this could introduce artifacts such as Gibb's ringing and or skew correlation coefficients. Furthermore, extremely high motion acquisitions shouldn't be taken into account as they can lead to inflated results. To do so, different metrics can be adopted, such as maximum framewise displacement, minimum number of low motion volumes or average framewise displacement. In NeoRS, acquisitions with average FD higher than 0.25 mm were introducing augmented correlations related to motion and improper denoising. Those acquisitions were completely removed. Therefore, the average framewise displacement was employed as the metric for exclusion.

To correct for nuisance variables NeoRS implements a traditional denoising strategy that performs global signal, white matter and cerebrospinal fluid signal regression, motion parameter regression and a band-pass filter. This simple approach provides robust results (Smyser et al., 2016), and doesn't require manual intervention or large datasets for denoising purposes. In contrast to the

aforementioned independent components denoising techniques, (Alfaro-Almagro et al., 2018; Griffanti et al., 2017) such as the one employed in the dHCP pipeline.

Finally, NeoRS incorporates seed-based functional connectivity analysis tools to assist the user in assessing initial results. Seed-based results across subjects showed patterns very similar to those observed in the literature for all the analyzed resting-state networks (Damaraju et al., 2010; Fransson et al., 2009) (Figure 6.11). Further data analysis can be carried out on the fully processed data, final_BOLD.nii, if desired.

6.7.1 Limitations and Future Directions

NeoRS was fully vetted on the BCP, and CHU (results not shown) cohorts for neonates less than 9 weeks old. Expanding NeoRS to a larger cohort in both size and neonatal age variation, i.e. preterm, would only further demonstrate its novelty and application, but the current number of subjects is a limitation. Obviously, this expansion would also necessitate additional age specific atlases. Additionally, the pipeline requires a usable T2-weighted structural image and would benefit from the adaptability of the option of using a T1-weighted image, especially for younger neonates older than 9 weeks where tissue boundaries may begin to vary. NeoRS has been developed based on a traditional denoising strategy which includes band-pass filtering. This is a limitation on data acquired with very low TR, such as the dHCP data, as the degrees of freedom might be highly reduced. In the Fourier domain, the maximum sample rate corresponds to the frequency of Nyquist, $f_{max} = 1/2TR$, and the frequency spacing $\Delta f = 1/t_{max}$, where t_{max} is the total scan duration. If there are two data sets with the same total acquisition time, but different TR, the one with the lower TR will lose more degrees of freedom when filtering (Bright, Tench, & Murphy, 2017). Another limitation of the pipeline is brains with significant malformations or injury. While a high range of brain sizes is accepted in the pipeline, anomalies such as neonatal hydrocephalus may require special attention, as part of the automated process could fail, such as cortical extraction. To overcome this limitation the user should perform rigorous individual image quality control of those brains and may adjust parameters, such as the head radius. Furthermore, it is known that a fundamental factor for measuring interindividual differences is reliability (Zuo et al., 2014) which is highly related to reproducibility. For this reason, performing a test-retest reliability approach should have been considered (Noble, Scheinost, & Constable, 2019). However, measuring the test-retest reliability is a challenge in this population. As mentioned by Xi-Nian Zuo et al. 2019 (Zuo, Xu, & Milham,

2019), at least 20-30 min of data are needed to perform functional connectivity reliability measurements which can be challenging. Moreover, performing multiple sessions is also a challenge because of the fast brain development. Additionally, neonates also present higher levels of motion, which compromises reliability (Zuo & Xing, 2014). To overcome this issue, we think that we should focus on acquiring high quality data by using real-time head motion monitoring tools such as FIRMM (Dosenbach et al., 2017). Finally, we are currently working on the inclusion of second-level analysis to allow the users to make group-level inference about networks. The possibility to perform Independent Component Analysis will also be available in the next release. Further functionalities such as the characterization of the networks and lifespan developmental trajectories of cortical thickness and surface area, as described by Xu Ting et al. 2015 (Xu et al., 2015) might be of particular interest as it would allow the study of the maturation process of the neonatal brain and the resting-state networks. The characterization of the resting-state networks over time is especially important on newborns as a deeper knowledge on networks development might help detecting possible outliers in a given population, bringing neonatal rs-fMRI one step closer of being a brain integrity biomarker.

6.8 Conclusion

NeoRS [https://github.com/venguix/NeoRS] is an open-source, straightforward to use rs-fMRI data processing pipeline for the neonatal brain which relies on the open-source neuroimaging pipelines FSL, AFNI and SPM. NeoRS works with neuroimaging nifti format, BIDS folder structures and has been developed to work with different MRI vendors and diverse acquisition parameters with minimal user implication. After image processing with NeoRS, we observed resting-state networks were in agreement with previously published studies at term age. Each processing step is easy to inspect to ensure consistent results through quality control checkpoint figures.

An open-source, rudimentary to use pipeline for neonatal resting-state image processing will allow the community to process their data immediately after scanning sessions implementing a simple computational infrastructure. The democratization of rs-fMRI processing will allow a higher number of centers to collaborate and process their datasets and optimistically bring the clinical biomarker application one step closer.

6.9 Acknowledgements

We would like to thank the Washington University – School of Medicine for sharing their templates for this project, and Jed Elison for letting us use the neonatal data from the Baby Connectome Project. We would also like to thank the Québec Bio-Imaging Network for supporting VE with studentship and funding for travels.

6.10 Conflict of interests

The authors declare that the research was conducted in the absence of any commercial or financial relationships that could be construed as a potential conflict of interest.

6.11 Authors contributions

VE developed NeoRS, processed and analyzed the data, and wrote the manuscript. JK provided guidance and helped comparing results with a non open-source pipeline. DL contributed writing and reviewing the first draft and provided guidance, JCA provided guidance and reviewed the manuscript, GA supervised the project, contributed writing and reviewing all drafts and provided guidance. All authors contributed to manuscript revision, read, and approved the submitted version.

6.12 Funding

Funded by the Canada Research Chair in Quantitative Magnetic Resonance Imaging [950-230815], the Canadian Institute of Health Research [CIHR FDN-143263], the Canada Foundation for Innovation [32454, 34824], the Fonds de Recherche du Québec - Santé [28826], the Natural Sciences and Engineering Research Council of Canada [RGPIN-2019-07244], the Canada First Research Excellence Fund (IVADO and TransMedTech), the Courtois NeuroMod project and the Quebec BioImaging Network [5886, 35450], INSPIRED (Spinal Research, UK; Wings for Life, Austria; Craig H. Neilsen Foundation, USA).

6.13 References

Alfaro-Almagro, F., Jenkinson, M., Bangerter, N. K., Andersson, J. L. R., Griffanti, L., Douaud, G., . . . Smith, S. M. (2018). Image processing and Quality Control for the first 10,000 brain imaging datasets from UK Biobank. *Neuroimage, 166*, 400-424. doi:10.1016/j.neuroimage.2017.10.034

Andersson, J. L., Skare, S., & Ashburner, J. (2003). How to correct susceptibility distortions in spin-echo echo-planar images: application to diffusion tensor imaging. *Neuroimage, 20*(2), 870-888. doi:10.1016/S1053-8119(03)00336-7

Andersson, J. L. R., Graham, M. S., Drobnjak, I., Zhang, H., & Campbell, J. (2018). Susceptibility-induced distortion that varies due to motion: Correction in diffusion MR without acquiring additional data. *Neuroimage, 171*, 277-295. doi:10.1016/j.neuroimage.2017.12.040

Beare, R. J., Chen, J., Kelly, C. E., Alexopoulos, D., Smyser, C. D., Rogers, C. E., . . . Thompson, D. K. (2016). Neonatal Brain Tissue Classification with Morphological Adaptation and Unified Segmentation. *Front Neuroinform, 10*, 12. doi:10.3389/fninf.2016.00012

Biswal, B., Yetkin, F. Z., Haughton, V. M., & Hyde, J. S. (1995). Functional connectivity in the motor cortex of resting human brain using echo-planar MRI. *Magn Reson Med, 34*(4), 537-541. doi:10.1002/mrm.1910340409

Bright, M. G., Tench, C. R., & Murphy, K. (2017). Potential pitfalls when denoising resting state fMRI data using nuisance regression. *Neuroimage, 154*, 159-168. doi:10.1016/j.neuroimage.2016.12.027

Cox, R. W. (1996). AFNI: software for analysis and visualization of functional magnetic resonance neuroimages. *Comput Biomed Res, 29*(3), 162-173. doi:10.1006/cbmr.1996.0014

Cusack, R., Brett, M., & Osswald, K. (2003). An evaluation of the use of magnetic field maps to undistort echo-planar images. *Neuroimage, 18*(1), 127-142. doi:10.1006/nimg.2002.1281

Czervionke, L. F., Daniels, D. L., Wehrli, F. W., Mark, L. P., Hendrix, L. E., Strandt, J. A., . . . Haughton, V. M. (1988). Magnetic susceptibility artifacts in gradient-recalled echo MR imaging. *AJNR Am J Neuroradiol, 9*(6), 1149-1155. Retrieved from https://www.ncbi.nlm.nih.gov/pubmed/3143237

Damaraju, E., Phillips, J. R., Lowe, J. R., Ohls, R., Calhoun, V. D., & Caprihan, A. (2010). Resting-state functional connectivity differences in premature children. *Front Syst Neurosci, 4*. doi:10.3389/fnsys.2010.00023

Enguix, V., Ding, Y., & Lodygensky, G. A. (2018). Recent advances in preclinical and clinical multimodal MR in the newborn brain. *J Magn Reson, 292*, 149-154. doi:10.1016/j.jmr.2018.04.017

Esteban, O., Markiewicz, C. J., Blair, R. W., Moodie, C. A., Isik, A. I., Erramuzpe, A., . . . Gorgolewski, K. J. (2019). fMRIPrep: a robust preprocessing pipeline for functional MRI. *Nat Methods, 16*(1), 111-116. doi:10.1038/s41592-018-0235-4

Fitzgibbon, S. P., Harrison, S. J., Jenkinson, M., Baxter, L., Robinson, E. C., Bastiani, M., . . . Andersson, J. (2020). The developing Human Connectome Project (dHCP) automated resting-state functional processing framework for newborn infants. *Neuroimage, 223*, 117303. doi:10.1016/j.neuroimage.2020.117303

Fransson, P., Skiold, B., Engstrom, M., Hallberg, B., Mosskin, M., Aden, U., . . . Blennow, M. (2009). Spontaneous brain activity in the newborn brain during natural sleep--an fMRI study in infants born at full term. *Pediatr Res, 66*(3), 301-305. doi:10.1203/PDR.0b013e3181b1bd84

Fransson, P., Skiold, B., Horsch, S., Nordell, A., Blennow, M., Lagercrantz, H., & Aden, U. (2007). Resting-state networks in the infant brain. *Proc Natl Acad Sci U S A, 104*(39), 15531-15536. doi:10.1073/pnas.0704380104

Friston, K. J., Williams, S., Howard, R., Frackowiak, R. S., & Turner, R. (1996). Movement-related effects in fMRI time-series. *Magn Reson Med, 35*(3), 346-355. doi:10.1002/mrm.1910350312

Gao, W., Lin, W., Grewen, K., & Gilmore, J. H. (2017). Functional Connectivity of the Infant Human Brain: Plastic and Modifiable. *Neuroscientist, 23*(2), 169-184. doi:10.1177/1073858416635986

Gao, W., Zhu, H., Giovanello, K. S., Smith, J. K., Shen, D., Gilmore, J. H., & Lin, W. (2009). Evidence on the emergence of the brain's default network from 2-week-old to 2-year-old healthy pediatric subjects. *Proc Natl Acad Sci U S A, 106*(16), 6790-6795. doi:10.1073/pnas.0811221106

Giove, F., Gili, T., Iacovella, V., Macaluso, E., & Maraviglia, B. (2009). Images-based suppression of unwanted global signals in resting-state functional connectivity studies. *Magn Reson Imaging, 27*(8), 1058-1064. doi:10.1016/j.mri.2009.06.004

Glasser, M. F., Sotiropoulos, S. N., Wilson, J. A., Coalson, T. S., Fischl, B., Andersson, J. L., . . . Consortium, W. U.-M. H. (2013). The minimal preprocessing pipelines for the Human Connectome Project. *Neuroimage, 80*, 105-124. doi:10.1016/j.neuroimage.2013.04.127

Graham, M. S., Drobnjak, I., Jenkinson, M., & Zhang, H. (2017). Quantitative assessment of the susceptibility artefact and its interaction with motion in diffusion MRI. *PLoS One, 12*(10), e0185647. doi:10.1371/journal.pone.0185647

Grayson, D. S., & Fair, D. A. (2017). Development of large-scale functional networks from birth to adulthood: A guide to the neuroimaging literature. *Neuroimage, 160*, 15-31. doi:10.1016/j.neuroimage.2017.01.079

Griffanti, L., Douaud, G., Bijsterbosch, J., Evangelisti, S., Alfaro-Almagro, F., Glasser, M. F., . . . Smith, S. M. (2017). Hand classification of fMRI ICA noise components. *Neuroimage, 154*, 188-205. doi:10.1016/j.neuroimage.2016.12.036

Holland, D., Kuperman, J. M., & Dale, A. M. (2010). Efficient correction of inhomogeneous static magnetic field-induced distortion in Echo Planar Imaging. *Neuroimage, 50*(1), 175-183. doi:10.1016/j.neuroimage.2009.11.044

Howell, B. R., Styner, M. A., Gao, W., Yap, P. T., Wang, L., Baluyot, K., . . . Elison, J. T. (2019). The UNC/UMN Baby Connectome Project (BCP): An overview of the study design and protocol development. *Neuroimage, 185*, 891-905. doi:10.1016/j.neuroimage.2018.03.049

Jenkinson, M., Bannister, P., Brady, M., & Smith, S. (2002). Improved optimization for the robust and accurate linear registration and motion correction of brain images. *Neuroimage, 17*(2), 825-841. doi:10.1016/s1053-8119(02)91132-8

Jenkinson, M., Beckmann, C. F., Behrens, T. E., Woolrich, M. W., & Smith, S. M. (2012). Fsl. *Neuroimage, 62*(2), 782-790. doi:10.1016/j.neuroimage.2011.09.015

Jezzard, P., & Balaban, R. S. (1995). Correction for geometric distortion in echo planar images from B0 field variations. *Magn Reson Med, 34*(1), 65-73. doi:10.1002/mrm.1910340111

Jo, H. J., Gotts, S. J., Reynolds, R. C., Bandettini, P. A., Martin, A., Cox, R. W., & Saad, Z. S. (2013). Effective Preprocessing Procedures Virtually Eliminate Distance-Dependent Motion Artifacts in Resting State FMRI. *J Appl Math, 2013*. doi:10.1155/2013/935154

Keunen, K., Counsell, S. J., & Benders, M. (2017). The emergence of functional architecture during early brain development. *Neuroimage, 160*, 2-14. doi:10.1016/j.neuroimage.2017.01.047

Lee, M. H., Smyser, C. D., & Shimony, J. S. (2013). Resting-state fMRI: a review of methods and clinical applications. *AJNR Am J Neuroradiol, 34*(10), 1866-1872. doi:10.3174/ajnr.A3263

Lund, T. E., Madsen, K. H., Sidaros, K., Luo, W. L., & Nichols, T. E. (2006). Non-white noise in fMRI: does modelling have an impact? *Neuroimage, 29*(1), 54-66. doi:10.1016/j.neuroimage.2005.07.005

Maknojia, S., Churchill, N. W., Schweizer, T. A., & Graham, S. J. (2019). Resting State fMRI: Going Through the Motions. *Front Neurosci, 13*, 825. doi:10.3389/fnins.2019.00825

McArdle, C. B., Richardson, C. J., Nicholas, D. A., Mirfakhraee, M., Hayden, C. K., & Amparo, E. G. (1987). Developmental features of the neonatal brain: MR imaging. Part I. Gray-white matter differentiation and myelination. *Radiology, 162*(1 Pt 1), 223-229. doi:10.1148/radiology.162.1.3786767

Ogawa, S., Lee, T. M., Kay, A. R., & Tank, D. W. (1990). Brain magnetic resonance imaging with contrast dependent on blood oxygenation. *Proc Natl Acad Sci U S A, 87*(24), 9868-9872. doi:10.1073/pnas.87.24.9868

Ogawa, S., Menon, R. S., Tank, D. W., Kim, S. G., Merkle, H., Ellermann, J. M., & Ugurbil, K. (1993). Functional brain mapping by blood oxygenation level-dependent contrast magnetic resonance imaging. A comparison of signal characteristics with a biophysical model. *Biophys J, 64*(3), 803-812. doi:10.1016/S0006-3495(93)81441-3

Parker, D. B., & Razlighi, Q. R. (2019). The Benefit of Slice Timing Correction in Common fMRI Preprocessing Pipelines. *Front Neurosci, 13*, 821. doi:10.3389/fnins.2019.00821

Power, J. D., Barnes, K. A., Snyder, A. Z., Schlaggar, B. L., & Petersen, S. E. (2012). Spurious but systematic correlations in functional connectivity MRI networks arise from subject motion. *Neuroimage, 59*(3), 2142-2154. doi:10.1016/j.neuroimage.2011.10.018

Power, J. D., Fair, D. A., Schlaggar, B. L., & Petersen, S. E. (2010). The development of human functional brain networks. *Neuron, 67*(5), 735-748. doi:10.1016/j.neuron.2010.08.017

Power, J. D., Mitra, A., Laumann, T. O., Snyder, A. Z., Schlaggar, B. L., & Petersen, S. E. (2014). Methods to detect, characterize, and remove motion artifact in resting state fMRI. *Neuroimage, 84*, 320-341. doi:10.1016/j.neuroimage.2013.08.048

Salimi-Khorshidi, G., Douaud, G., Beckmann, C. F., Glasser, M. F., Griffanti, L., & Smith, S. M. (2014). Automatic denoising of functional MRI data: combining independent component analysis and hierarchical fusion of classifiers. *Neuroimage, 90*, 449-468. doi:10.1016/j.neuroimage.2013.11.046

Smith, S. M., Jenkinson, M., Woolrich, M. W., Beckmann, C. F., Behrens, T. E., Johansen-Berg, H., . . . Matthews, P. M. (2004). Advances in functional and structural MR image analysis and implementation as FSL. *Neuroimage, 23 Suppl 1*, S208-219. doi:10.1016/j.neuroimage.2004.07.051

Smyser, C. D., Inder, T. E., Shimony, J. S., Hill, J. E., Degnan, A. J., Snyder, A. Z., & Neil, J. J. (2010). Longitudinal analysis of neural network development in preterm infants. *Cereb Cortex, 20*(12), 2852-2862. doi:10.1093/cercor/bhq035

Smyser, C. D., & Neil, J. J. (2015). Use of resting-state functional MRI to study brain development and injury in neonates. *Semin Perinatol, 39*(2), 130-140. doi:10.1053/j.semperi.2015.01.006

Smyser, C. D., Snyder, A. Z., Shimony, J. S., Blazey, T. M., Inder, T. E., & Neil, J. J. (2013). Effects of white matter injury on resting state fMRI measures in prematurely born infants. *PLoS One, 8*(7), e68098. doi:10.1371/journal.pone.0068098

Smyser, C. D., Snyder, A. Z., Shimony, J. S., Mitra, A., Inder, T. E., & Neil, J. J. (2016). Resting-State Network Complexity and Magnitude Are Reduced in Prematurely Born Infants. *Cereb Cortex, 26*(1), 322-333. doi:10.1093/cercor/bhu251

Sylvester, C. M., Smyser, C. D., Smyser, T., Kenley, J., Ackerman, J. J., Jr., Shimony, J. S., . . . Rogers, C. E. (2018). Cortical Functional Connectivity Evident After Birth and Behavioral Inhibition at Age 2. *Am J Psychiatry, 175*(2), 180-187. doi:10.1176/appi.ajp.2017.17010018

Talairach, J. (1988). Co-planar stereotaxic atlas of the human brain-3-dimensional proportional system. *An approach to cerebral imaging*.

Vos de Wael, R., Hyder, F., & Thompson, G. J. (2017). Effects of Tissue-Specific Functional Magnetic Resonance Imaging Signal Regression on Resting-State Functional Connectivity. *Brain Connect, 7*(8), 482-490. doi:10.1089/brain.2016.0465

Whitfield-Gabrieli, S., & Nieto-Castanon, A. (2012). Conn: a functional connectivity toolbox for correlated and anticorrelated brain networks. *Brain Connect, 2*(3), 125-141. doi:10.1089/brain.2012.0073

Woolrich, M. W., Jbabdi, S., Patenaude, B., Chappell, M., Makni, S., Behrens, T., . . . Smith, S. M. (2009). Bayesian analysis of neuroimaging data in FSL. *Neuroimage, 45*(1 Suppl), S173-186. doi:10.1016/j.neuroimage.2008.10.055

Zhang, H., Shen, D., & Lin, W. (2019). Resting-state functional MRI studies on infant brains: A decade of gap-filling efforts. *Neuroimage, 185*, 664-684. doi:10.1016/j.neuroimage.2018.07.004

CHAPTER 7 GENERAL DISCUSSION

This project aimed to provide the tools to acquire and preprocess neonatal resting-state fMRI data. The first goal of this project was to set up an acquisition and head motion quality control protocol for the 3T clinical MRI of the CHU Sainte-Justine. This project describes all the details about the acquisition and quality control protocols and offers improvements for future works. The second goal was to provide the tools to preprocess neonatal resting-state fMRI data as it presents substantial differences from adults. NeoRS, a neonatal rs-fMRI data preprocessing pipeline, was developed and made open-source. In this chapter, the main results are summarized and discussed with a particular emphasis on the challenges and future directions of the research.

7.1 Resting-state fMRI in young adults born with congenital heart disease

This study was carried out at the beginning of my thesis to master state-of-the-art methods, tools, and challenges in preprocessing adult rs-fMRI data. Furthermore, while it is well known that youth operated from congenital heart disease at birth present altered executive function compared to a control group (Fontes et al., 2019), there was little information about the long-term effects on functional connectivity. Therefore, this study offered the first evidence supporting that this population present disrupted functional connectivity. We found abnormal connectivity in the amygdala, fronto-orbital cortex, dorsal attention, fronto-parietal, and default-mode networks. We proved that functional connectivity alterations persisted over the past years, and that can be observed using rs-fMRI. This suggests that characterization of the resting-state networks over time could provide information about functional connectivity alterations and future neurocognitive disorders. Nevertheless, much work still needs to be done to characterize single-subject resting-state networks, bringing neonatal rs-fMRI one step closer to being a biomarker.

7.2 Neonatal resting-state fMRI acquisition

In Chapter 5 of this thesis, I described the acquisition protocol that was set up for the 3T clinical MRI from the CHU Sainte-Justine (GE Discovery MR750). The protocol contains the necessary

information to successfully perform neonatal rs-fMRI in the aforementioned scanner and includes structural, functional, and distortion correction purpose sequences. We built a protocol that provides high-resolution T2-weighted images while keeping a low SAR, allowing distortion corrections in further image preprocessing steps. The rs-fMRI acquisition parameters are similar to De Asis-Cruz (De Asis-Cruz et al., 2015). However, they employed a relatively lower TR (TR=2000 ms) compared to ours (TR=3000 ms), allowing the whole baby brain acquisition while having a better temporal resolution. We decided to provisionally keep the TR=3000 ms as the first acquisitions of some of the ongoing projects were acquired this way, and results won't be comparable if changed. One of the biggest limitations we found when setting up the acquisition protocol was that the MRI software and hardware didn't allow us to perform multi-band acquisitions. This provides significant advantages with few drawbacks, as explained in Chapter 4.

As previously shown in the literature of Smyser et al., head motion plays an important role when acquiring neonatal resting-state fMRI data. We observed that about half of the scanned newborns couldn't be analyzed due to excessive levels of head motion. This was consistently observed after the scanning session, making a re-scan impossible. For this reason, real-time head motion quality controls seem a promising approach to ensure low levels of motion. Therefore, we used the average framewise displacement to evaluate two different datasets to set up a real-time quality control protocol in the CHU Sainte-Justine that could potentially be employed in other institutions. Moreover, after discussions with the Washington University School of Medicine in Saint Louis, they recently published an article using average framewise displacement to evaluate real-time head motion in infants (Badke D'Andrea et al., 2022). This may confirm its use as a valid metric for assessing head motion when combined with other metrics, such as the total number of good frames, as we did in our study.

We observed that when the average framewise displacement was inferior to 0.25 mm for both datasets, we could observe resting-state networks in agreement with the literature when the scanning time was sufficiently long (B. Chen et al., 2021; Fransson et al., 2007).

Furthermore, we observed that at least 5 minutes of data were required when TR was lower than 1 second and that in most cases when TR was 3 seconds, slightly more than 5 minutes of acquisition were required, probably due to the lower number of time points. For subjects presenting average framewise displacement lower than 0.25mm, the required scan duration was in agreement with the

literature, where around 6 minutes of acquisition were needed to evaluate functional connectivity (Van Dijk et al., 2010). Moreover, Birn et al. showed that between-sessions and test-retest reliability could be improved by increasing the acquisition time to 9-13 minutes or longer (Birn et al., 2013). Real-time head motion monitoring allows immediate re-scan of the baby while still in the MRI room; however, a big limitation of this approach is that once the baby is fully awake, it becomes impossible to continue with the acquisition. Thereby, as resting-state fMRI is very susceptible to head motion, the first easy solution would be to perform the rs-fMRI acquisition at the beginning of the acquisition protocol when the baby is completely sleeping. Finally, more advanced acquisition and denoising strategies, such as multi-echo acquisition, should be considered in future projects to reduce motion signals (Power et al., 2018).

7.3 NeoRS – resting-state fMRI image preprocessing pipeline

Until now, no open-source pipelines were available to preprocess neonatal resting-state fMRI data, and researchers had to develop their in-house codes or adapt adult pipelines, requiring specific atlases, time, and knowledge. NeoRS aims to provide the community with a pipeline that addresses the specificity of neonatal brain imaging and is easy to use and customize. The pipeline preprocessing steps include image registration to an atlas, skull stripping, tissue segmentation, slice timing, head motion and distortion corrections, spatial smoothing, and confounds regression. It also provides an atlas and a set of seed regions for neonates. NeoRS also allows basic seed-based correlation analysis, and we are currently working on implementing independent component analysis for the next release. It includes quality control using visual assessment checkpoints.

Furthermore, it has unique functionalities, such as the possibility of automatically discarding data with a high global head motion. This functionality was implemented based on the previously mentioned study about average framewise displacement. Also, it includes the capability to analyze short time segments in a long time series. For example, it can automatically detect from a whole acquisition (i.e., 10 min) the 3 min segment with the lowest average framewise displacement. It also includes robust skull-stripping for infants from 27 to 44 weeks postmenstrual age. This is achieved by previously aligning data through an atlas. Data is aligned by affine registration, so a simple binary mask couldn’t be applied to simplify the skull stripping process. A non-rigid registration would be needed in this case. However, non-linear registration tools are not robust

enough to be implemented in automatized pipelines. This was also observed by the developers of dHCP (Fitzgibbon et al., 2020).

Nevertheless, despite the advantages and simplicity of NeoRS, some limitations need to be addressed. One of the biggest limitations of NeoRS is that it uses traditional denoising strategies, including band-pass filtering, which may notoriously reduce the degrees of freedom on data with very low TR, as specified in the NeoRS article. Independent components denoising strategies could be employed for denoising purposes; however, it would require manual separation of neural and non-neural components. A machine learning approach could also be used, as done by the Developing Human Connectome Project, to differentiate between noise and neural signals with an adequate sample size (Fitzgibbon et al., 2020). To improve NeoRS, more sophisticated data analysis tools could be added, such as independent component analysis or graph theory.

NeoRS was developed for resting-state fMRI applications. However, I've found out that structural preprocessing could be very useful in other applications. For example, some machine-learning algorithms require skull-stripping, segmentation, or template alignment before training. So, I decided to build a separate module that includes reorientation, registration, skull stripping and segmentation. Finally, I think NeoRS is having a big impact on the community. Since its publication in July 2022, the article already has 2074 views, and I've already been able to assist SickKids hospital in implementing it. Hopefully, this will encourage other institutions to perform neonatal rs-fMRI studies. An area that I look forward to see expand in the future are new metrics to evaluate resting-state networks, especially at the single subject level. Moreover, rs-fMRI studies with straightforward statistical analysis studying the potential to predict motor, cognition and behavior outcomes still need to be performed on large cohorts. Ultimately, this knowledge will be used for individual level evaluations and rs-fMRI could be used as a predictive biomarker.

CHAPTER 8 CONCLUSION

Resting-state networks are a powerful tool for understanding neonatal brain injury in premature babies with a high risk of brain damage. The evaluation of brain functional connectivity provides meaningful information about brain physiology that can't be observed using standard neuroanatomical techniques. Clinically, the impact of brain injury on the different resting-state networks offers advances in terms of prognosis since prematurity-related impairments, although present at birth, are generally expressed at school age. However, its application poses several methodological challenges. For instance, the head motion alters data quality leading to unusable data. Moreover, neonatal resting-state data preprocessing is very complex and presents substantial differences from adults. Hence, the two main goals of this project were to set up an acquisition protocol and head motion quality control to scan neonatal rs-fMRI data successfully and to provide an open-source pipeline to preprocess neonatal rs-fMRI data.

During the first part of this project, the focus was on learning the state-of-the-art methods to preprocess and analyze resting-state fMRI data. This helped me to get a further understanding of the existing tools. To do so, we preprocessed and analyzed rs-fMRI data of young adults born with congenital heart disease. This study also provided insights into the potential long-term effects of congenital heart disease on resting-state networks.

The second part of this project was focused on neonatal rs-fMRI acquisition. A scanning protocol was implemented for the clinical 3T MRI of the CHU Sainte-Justine, and possible improvements were also discussed. We showed that the average framewise displacement could be used as a quality control metric for head motion and provided a real-time head motion assessment strategy.

After establishing the acquisition protocol, a pipeline to preprocess neonatal resting-state fMRI data was developed based on gold-standard open-source neuroimaging toolkits. The developed pipeline was called NeoRS and is open-source and fully available on git-hub. NeoRS uses nifti neuroimaging format, BIDS data structure and works with different MRI constructors. It provides an atlas as well as a set of seed regions. Parameters are easily customizable and allow single- and multi-band data preprocessing with minimal user implications. Furthermore, to ensure consistent results, it provides quality control checkpoint figures. NeoRS aims to allow a higher number of

laboratories and hospitals to collaborate and preprocess their neonatal datasets to hopefully promote the use of rs-fMRI to understand brain development and disruptors.

REFERENCES

Achard, S., & Bullmore, E. (2007). Efficiency and cost of economical brain functional networks. *PLoS Comput Biol, 3*(2), e17. doi:10.1371/journal.pcbi.0030017

Alfaro-Almagro, F., Jenkinson, M., Bangerter, N. K., Andersson, J. L. R., Griffanti, L., Douaud, G., . . . Smith, S. M. (2018). Image processing and Quality Control for the first 10,000 brain imaging datasets from UK Biobank. *Neuroimage, 166*, 400-424. doi:10.1016/j.neuroimage.2017.10.034

Alhourani, A., Wozny, T. A., Krishnaswamy, D., Pathak, S., Walls, S. A., Ghuman, A. S., . . . Niranjan, A. (2016). Magnetoencephalography-based identification of functional connectivity network disruption following mild traumatic brain injury. *J Neurophysiol, 116*(4), 1840-1847. doi:10.1152/jn.00513.2016

Alonazi, B. K., Keller, S. S., Fallon, N., Adams, V., Das, K., Marson, A. G., & Sluming, V. (2019). Resting-state functional brain networks in adults with a new diagnosis of focal epilepsy. *Brain Behav, 9*(1), e01168. doi:10.1002/brb3.1168

Anand, S. S., Singh, H., & Dash, A. K. (2009). Clinical Applications of PET and PET-CT. *Med J Armed Forces India, 65*(4), 353-358. doi:10.1016/S0377-1237(09)80099-3

Anderson, J. S., Ferguson, M. A., Lopez-Larson, M., & Yurgelun-Todd, D. (2011). Reproducibility of single-subject functional connectivity measurements. *AJNR Am J Neuroradiol, 32*(3), 548-555. doi:10.3174/ajnr.A2330

Andersson, J. L., Skare, S., & Ashburner, J. (2003). How to correct susceptibility distortions in spin-echo echo-planar images: application to diffusion tensor imaging. *Neuroimage, 20*(2), 870-888. doi:10.1016/S1053-8119(03)00336-7

Andersson, J. L. R., Graham, M. S., Drobnjak, I., Zhang, H., & Campbell, J. (2018). Susceptibility-induced distortion that varies due to motion: Correction in diffusion MR without acquiring additional data. *Neuroimage, 171*, 277-295. doi:10.1016/j.neuroimage.2017.12.040

Askin Incebacak, N. C., Sui, Y., Gui Levy, L., Merlini, L., Sa de Almeida, J., Courvoisier, S., . . . Lazeyras, F. (2022). Super-resolution reconstruction of T2-weighted thick-slice neonatal brain MRI scans. *J Neuroimaging, 32*(1), 68-79. doi:10.1111/jon.12929

Babaeeghazvini, P., Rueda-Delgado, L. M., Gooijers, J., Swinnen, S. P., & Daffertshofer, A. (2021). Brain Structural and Functional Connectivity: A Review of Combined Works of Diffusion Magnetic Resonance Imaging and Electro-Encephalography. *Front Hum Neurosci, 15*, 721206. doi:10.3389/fnhum.2021.721206

Badke D'Andrea, C., Kenley, J. K., Montez, D. F., Mirro, A. E., Miller, R. L., Earl, E. A., . . . Greene, D. J. (2022). Real-time motion monitoring improves functional MRI data quality in infants. *Dev Cogn Neurosci, 55*, 101116. doi:10.1016/j.dcn.2022.101116

Bagge, C. N., Henderson, V. W., Laursen, H. B., Adelborg, K., Olsen, M., & Madsen, N. L. (2018). Risk of Dementia in Adults With Congenital Heart Disease: Population-Based Cohort Study. *Circulation, 137*(18), 1912-1920. doi:10.1161/CIRCULATIONAHA.117.029686

Bammer, R., Keeling, S. L., Augustin, M., Pruessmann, K. P., Wolf, R., Stollberger, R., . . . Fazekas, F. (2001). Improved diffusion-weighted single-shot echo-planar imaging (EPI) in stroke using sensitivity encoding (SENSE). *Magn Reson Med, 46*(3), 548-554. doi:10.1002/mrm.1226

Banks, S. J., Eddy, K. T., Angstadt, M., Nathan, P. J., & Phan, K. L. (2007). Amygdala-frontal connectivity during emotion regulation. *Soc Cogn Affect Neurosci, 2*(4), 303-312. doi:10.1093/scan/nsm029

Barbey, A. K., Koenigs, M., & Grafman, J. (2011). Orbitofrontal contributions to human working memory. *Cereb Cortex, 21*(4), 789-795. doi:10.1093/cercor/bhq153

Batra, A. S., Alexander, M. E., & Silka, M. J. (2012). Attention-deficit/hyperactivity disorder, stimulant therapy, and the patient with congenital heart disease: evidence and reason. *Pediatr Cardiol, 33*(3), 394-401. doi:10.1007/s00246-012-0162-6

Bauml, J. G., Baumann, N., Avram, M., Mulej Bratec, S., Breeman, L., Berndt, M., . . . Sorg, C. (2019). The Default Mode Network Mediates the Impact of Infant Regulatory Problems on Adult Avoidant Personality Traits. *Biol Psychiatry Cogn Neurosci Neuroimaging, 4*(4), 333-342. doi:10.1016/j.bpsc.2018.11.005

Beare, R. J., Chen, J., Kelly, C. E., Alexopoulos, D., Smyser, C. D., Rogers, C. E., . . . Thompson, D. K. (2016). Neonatal Brain Tissue Classification with Morphological Adaptation and Unified Segmentation. *Front Neuroinform, 10*, 12. doi:10.3389/fninf.2016.00012

Behzadi, Y., Restom, K., Liau, J., & Liu, T. T. (2007). A component based noise correction method (CompCor) for BOLD and perfusion based fMRI. *Neuroimage, 37*(1), 90-101. doi:10.1016/j.neuroimage.2007.04.042

Bernier, P. L., Stefanescu, A., Samoukovic, G., & Tchervenkov, C. I. (2010). The challenge of congenital heart disease worldwide: epidemiologic and demographic facts. *Semin Thorac Cardiovasc Surg Pediatr Card Surg Annu, 13*(1), 26-34. doi:10.1053/j.pcsu.2010.02.005

Biasiucci, A., Franceschiello, B., & Murray, M. M. (2019). Electroencephalography. *Curr Biol, 29*(3), R80-R85. doi:10.1016/j.cub.2018.11.052

Birn, R. M., Molloy, E. K., Patriat, R., Parker, T., Meier, T. B., Kirk, G. R., . . . Prabhakaran, V. (2013). The effect of scan length on the reliability of resting-state fMRI connectivity estimates. *Neuroimage, 83*, 550-558. doi:10.1016/j.neuroimage.2013.05.099

Biswal, B., Yetkin, F. Z., Haughton, V. M., & Hyde, J. S. (1995). Functional connectivity in the motor cortex of resting human brain using echo-planar MRI. *Magn Reson Med, 34*(4), 537-541. doi:10.1002/mrm.1910340409

Blackford, J. U., Clauss, J. A., Avery, S. N., Cowan, R. L., Benningfield, M. M., & VanDerKlok, R. M. (2014). Amygdala-cingulate intrinsic connectivity is associated with degree of social inhibition. *Biol Psychol, 99*, 15-25. doi:10.1016/j.biopsycho.2014.02.003

Boas, D. A., Dale, A. M., & Franceschini, M. A. (2004). Diffuse optical imaging of brain activation: approaches to optimizing image sensitivity, resolution, and accuracy. *Neuroimage, 23 Suppl 1*, S275-288. doi:10.1016/j.neuroimage.2004.07.011

Bolduc, M. E., Lambert, H., Ganeshamoorthy, S., & Brossard-Racine, M. (2018). Structural brain abnormalities in adolescents and young adults with congenital heart defect: a systematic review. *Dev Med Child Neurol, 60*(12), 1209-1224. doi:10.1111/dmcn.13975

Bosl, W., Tierney, A., Tager-Flusberg, H., & Nelson, C. (2011). EEG complexity as a biomarker for autism spectrum disorder risk. *BMC Med, 9*, 18. doi:10.1186/1741-7015-9-18

Bouyagoub, S., Dowell, N. G., Gabel, M., & Cercignani, M. (2021). Comparing multiband and singleband EPI in NODDI at 3 T: what are the implications for reproducibility and study sample sizes? *MAGMA, 34*(4), 499-511. doi:10.1007/s10334-020-00897-7

Bozhilova, N. S., Michelini, G., Kuntsi, J., & Asherson, P. (2018). Mind wandering perspective on attention-deficit/hyperactivity disorder. *Neurosci Biobehav Rev, 92*, 464-476. doi:10.1016/j.neubiorev.2018.07.010

Brewster, R. C., King, T. Z., Burns, T. G., Drossner, D. M., & Mahle, W. T. (2015). White Matter Integrity Dissociates Verbal Memory and Auditory Attention Span in Emerging Adults with Congenital Heart Disease. *J Int Neuropsychol Soc, 21*(1), 22-33. doi:10.1017/S135561771400109X

Bright, M. G., Tench, C. R., & Murphy, K. (2017). Potential pitfalls when denoising resting state fMRI data using nuisance regression. *Neuroimage, 154*, 159-168. doi:10.1016/j.neuroimage.2016.12.027

Brossard-Racine, M., du Plessis, A., Vezina, G., Robertson, R., Donofrio, M., Tworetzky, W., & Limperopoulos, C. (2016). Brain Injury in Neonates with Complex Congenital Heart Disease: What Is the Predictive Value of MRI in the Fetal Period? *AJNR Am J Neuroradiol, 37*(7), 1338-1346. doi:10.3174/ajnr.A4716

Buckner, R. L., Andrews-Hanna, J. R., & Schacter, D. L. (2008). The brain's default network: anatomy, function, and relevance to disease. *Ann N Y Acad Sci, 1124*, 1-38. doi:10.1196/annals.1440.011

Calderon, J., & Bellinger, D. C. (2015). Executive function deficits in congenital heart disease: why is intervention important? *Cardiol Young, 25*(7), 1238-1246. doi:10.1017/S1047951115001134

Cassidy, A. R., White, M. T., DeMaso, D. R., Newburger, J. W., & Bellinger, D. C. (2015). Executive Function in Children and Adolescents with Critical Cyanotic Congenital Heart Disease. *J Int Neuropsychol Soc, 21*(1), 34-49. doi:10.1017/S1355617714001027

Chen, B., Linke, A., Olson, L., Ibarra, C., Kinnear, M., & Fishman, I. (2021). Resting state functional networks in 1-to-3-year-old typically developing children. *Dev Cogn Neurosci, 51*, 100991. doi:10.1016/j.dcn.2021.100991

Chen, J. J., Herman, P., Keilholz, S., & Thompson, G. J. (2020). Editorial: Origins of the Resting-State fMRI Signal. *Front Neurosci, 14*, 594990. doi:10.3389/fnins.2020.594990

Church, J. A., Fair, D. A., Dosenbach, N. U., Cohen, A. L., Miezin, F. M., Petersen, S. E., & Schlaggar, B. L. (2009). Control networks in paediatric Tourette syndrome show immature and anomalous patterns of functional connectivity. *Brain, 132*(Pt 1), 225-238. doi:10.1093/brain/awn223

Ciarrusta, J., Dimitrova, R., Batalle, D., O'Muircheartaigh, J., Cordero-Grande, L., Price, A., . . . McAlonan, G. (2020). Emerging functional connectivity differences in newborn infants vulnerable to autism spectrum disorders. *Transl Psychiatry, 10*(1), 131. doi:10.1038/s41398-020-0805-y

Cole, M. W., & Schneider, W. (2007). The cognitive control network: Integrated cortical regions with dissociable functions. *Neuroimage, 37*(1), 343-360. doi:10.1016/j.neuroimage.2007.03.071

Cox, R. W. (1996). AFNI: software for analysis and visualization of functional magnetic resonance neuroimages. *Comput Biomed Res, 29*(3), 162-173. doi:10.1006/cbmr.1996.0014

Cullen, K. R., Westlund, M. K., Klimes-Dougan, B., Mueller, B. A., Houri, A., Eberly, L. E., & Lim, K. O. (2014). Abnormal amygdala resting-state functional connectivity in adolescent depression. *JAMA Psychiatry, 71*(10), 1138-1147. doi:10.1001/jamapsychiatry.2014.1087

Cusack, R., Brett, M., & Osswald, K. (2003). An evaluation of the use of magnetic field maps to undistort echo-planar images. *Neuroimage, 18*(1), 127-142. doi:10.1006/nimg.2002.1281

Czervionke, L. F., Daniels, D. L., Wehrli, F. W., Mark, L. P., Hendrix, L. E., Strandt, J. A., . . . Haughton, V. M. (1988). Magnetic susceptibility artifacts in gradient-recalled echo MR imaging. *AJNR Am J Neuroradiol, 9*(6), 1149-1155. Retrieved from https://www.ncbi.nlm.nih.gov/pubmed/3143237

Damaraju, E., Phillips, J. R., Lowe, J. R., Ohls, R., Calhoun, V. D., & Caprihan, A. (2010). Resting-state functional connectivity differences in premature children. *Front Syst Neurosci, 4*. doi:10.3389/fnsys.2010.00023

Davey, C. G., Pujol, J., & Harrison, B. J. (2016). Mapping the self in the brain's default mode network. *Neuroimage, 132*, 390-397. doi:10.1016/j.neuroimage.2016.02.022

De Asis-Cruz, J., Bouyssi-Kobar, M., Evangelou, I., Vezina, G., & Limperopoulos, C. (2015). Functional properties of resting state networks in healthy full-term newborns. *Sci Rep, 5*, 17755. doi:10.1038/srep17755

De Asis-Cruz, J., Donofrio, M. T., Vezina, G., & Limperopoulos, C. (2018). Aberrant brain functional connectivity in newborns with congenital heart disease before cardiac surgery. *Neuroimage Clin, 17*, 31-42. doi:10.1016/j.nicl.2017.09.020

DeMaso, D. R., Calderon, J., Taylor, G. A., Holland, J. E., Stopp, C., White, M. T., . . . Newburger, J. W. (2017). Psychiatric Disorders in Adolescents With Single Ventricle Congenital Heart Disease. *Pediatrics, 139*(3). doi:10.1542/peds.2016-2241

Doria, V., Beckmann, C. F., Arichi, T., Merchant, N., Groppo, M., Turkheimer, F. E., . . . Edwards, A. D. (2010). Emergence of resting state networks in the preterm human brain. *Proc Natl Acad Sci U S A, 107*(46), 20015-20020. doi:10.1073/pnas.1007921107

Dosenbach, N. U. F., Koller, J. M., Earl, E. A., Miranda-Dominguez, O., Klein, R. L., Van, A. N., . . . Fair, D. A. (2017). Real-time motion analytics during brain MRI improve data quality and reduce costs. *Neuroimage, 161*, 80-93. doi:10.1016/j.neuroimage.2017.08.025

Drew, P. J. (2019). Vascular and neural basis of the BOLD signal. *Curr Opin Neurobiol, 58*, 61-69. doi:10.1016/j.conb.2019.06.004

Easson, K., Dahan-Oliel, N., Rohlicek, C., Sahakian, S., Brossard-Racine, M., Mazer, B., . . . Majnemer, A. (2019). A Comparison of Developmental Outcomes of Adolescent Neonatal Intensive Care Unit Survivors Born with a Congenital Heart Defect or Born Preterm. *J Pediatr, 207*, 34-41 e32. doi:10.1016/j.jpeds.2018.11.002

Easson, K., Rohlicek, C. V., Houde, J. C., Gilbert, G., Saint-Martin, C., Fontes, K., . . . Brossard-Racine, M. (2020). Quantification of apparent axon density and orientation dispersion in the white matter of youth born with congenital heart disease. *Neuroimage, 205*, 116255. doi:10.1016/j.neuroimage.2019.116255

Edwards, A. D., Rueckert, D., Smith, S. M., Abo Seada, S., Alansary, A., Almalbis, J., . . . Hajnal, J. V. (2022). The Developing Human Connectome Project Neonatal Data Release. *Front Neurosci, 16*, 886772. doi:10.3389/fnins.2022.886772

Ehrler, M., Latal, B., Kretschmar, O., von Rhein, M., & O'Gorman Tuura, R. (2020). Altered frontal white matter microstructure is associated with working memory impairments in adolescents with congenital heart disease: A diffusion tensor imaging study. *Neuroimage Clin, 25*, 102123. doi:10.1016/j.nicl.2019.102123

Enguix, V., Ding, Y., & Lodygensky, G. A. (2018). Recent advances in preclinical and clinical multimodal MR in the newborn brain. *J Magn Reson, 292*, 149-154. doi:10.1016/j.jmr.2018.04.017

Enguix, V., Easson, K., Gilbert, G., Saint-Martin, C., Rohlicek, C., Luck, D., . . . Brossard-Racine, M. (2022). Altered resting state functional connectivity in youth with congenital heart disease operated during infancy. *PLoS One, 17*(4), e0264781. doi:10.1371/journal.pone.0264781

Enguix, V., Kenley, J., Luck, D., Cohen-Adad, J., & Lodygensky, G. A. (2022). NeoRS: A Neonatal Resting State fMRI Data Preprocessing Pipeline. *Front Neuroinform, 16*, 843114. doi:10.3389/fninf.2022.843114

Ernst, R. R., & Anderson, W. A. (1966). Application of Fourier transform spectroscopy to magnetic resonance. *Review of Scientific Instruments, 37*(1), 93-102.

Esteban, O., Markiewicz, C. J., Blair, R. W., Moodie, C. A., Isik, A. I., Erramuzpe, A., . . . Gorgolewski, K. J. (2019). fMRIPrep: a robust preprocessing pipeline for functional MRI. *Nat Methods, 16*(1), 111-116. doi:10.1038/s41592-018-0235-4

Fair, D. A., Posner, J., Nagel, B. J., Bathula, D., Dias, T. G., Mills, K. L., . . . Nigg, J. T. (2010). Atypical default network connectivity in youth with attention-deficit/hyperactivity disorder. *Biol Psychiatry, 68*(12), 1084-1091. doi:10.1016/j.biopsych.2010.07.003

Fang, L., Yao, Z., An, J., Chen, X., Xie, Y., Zhao, H., . . . Ma, X. (2016). Topological Organization of Metabolic Brain Networks in Pre-Chemotherapy Cancer with Depression: A Resting-State PET Study. *PLoS One, 11*(11), e0166049. doi:10.1371/journal.pone.0166049

Figueroa, C. A., Mocking, R. J. T., van Wingen, G., Martens, S., Ruhe, H. G., & Schene, A. H. (2017). Aberrant default-mode network-hippocampus connectivity after sad memory-recall in remitted-depression. *Soc Cogn Affect Neurosci, 12*(11), 1803-1813. doi:10.1093/scan/nsx108

Figueroa-Vargas, A., Carcamo, C., Henriquez-Ch, R., Zamorano, F., Ciampi, E., Uribe-San-Martin, R., . . . Billeke, P. (2020). Frontoparietal connectivity correlates with working memory performance in multiple sclerosis. *Sci Rep, 10*(1), 9310. doi:10.1038/s41598-020-66279-0

Fitzgibbon, S. P., Harrison, S. J., Jenkinson, M., Baxter, L., Robinson, E. C., Bastiani, M., . . . Andersson, J. (2020). The developing Human Connectome Project (dHCP) automated resting-state functional processing framework for newborn infants. *Neuroimage, 223*, 117303. doi:10.1016/j.neuroimage.2020.117303

Fontes, K., Courtin, F., Rohlicek, C. V., Saint-Martin, C., Gilbert, G., Easson, K., . . . Brossard-Racine, M. (2020). Characterizing the Subcortical Structures in Youth with Congenital Heart Disease. *American Journal of Neuroradiology, 41*(8), 1503-1508. doi:10.3174/ajnr.A6667

Fontes, K., Rohlicek, C. V., Saint-Martin, C., Gilbert, G., Easson, K., Majnemer, A., . . . Brossard-Racine, M. (2019). Hippocampal alterations and functional correlates in adolescents and young adults with congenital heart disease. *Hum Brain Mapp, 40*(12), 3548-3560. doi:10.1002/hbm.24615

Frank, D. W., Dewitt, M., Hudgens-Haney, M., Schaeffer, D. J., Ball, B. H., Schwarz, N. F., . . . Sabatinelli, D. (2014). Emotion regulation: quantitative meta-analysis of functional activation and deactivation. *Neurosci Biobehav Rev, 45*, 202-211. doi:10.1016/j.neubiorev.2014.06.010

Fransson, P., Skiold, B., Engstrom, M., Hallberg, B., Mosskin, M., Aden, U., . . . Blennow, M. (2009). Spontaneous brain activity in the newborn brain during natural sleep--an fMRI study in infants born at full term. *Pediatr Res, 66*(3), 301-305. doi:10.1203/PDR.0b013e3181b1bd84

Fransson, P., Skiold, B., Horsch, S., Nordell, A., Blennow, M., Lagercrantz, H., & Aden, U. (2007). Resting-state networks in the infant brain. *Proc Natl Acad Sci U S A, 104*(39), 15531-15536. doi:10.1073/pnas.0704380104

Franz, A. P., Bolat, G. U., Bolat, H., Matijasevich, A., Santos, I. S., Silveira, R. C., . . . Moreira-Maia, C. R. (2018). Attention-Deficit/Hyperactivity Disorder and Very Preterm/Very Low Birth Weight: A Meta-analysis. *Pediatrics, 141*(1). doi:10.1542/peds.2017-1645

Friston, K. J., Williams, S., Howard, R., Frackowiak, R. S., & Turner, R. (1996). Movement-related effects in fMRI time-series. *Magn Reson Med, 35*(3), 346-355. doi:10.1002/mrm.1910350312

Gao, W., Alcauter, S., Elton, A., Hernandez-Castillo, C. R., Smith, J. K., Ramirez, J., & Lin, W. (2015). Functional Network Development During the First Year: Relative Sequence and Socioeconomic Correlations. *Cereb Cortex, 25*(9), 2919-2928. doi:10.1093/cercor/bhu088

Gao, W., Lin, W., Grewen, K., & Gilmore, J. H. (2017). Functional Connectivity of the Infant Human Brain: Plastic and Modifiable. *Neuroscientist, 23*(2), 169-184. doi:10.1177/1073858416635986

Gao, W., Zhu, H., Giovanello, K. S., Smith, J. K., Shen, D., Gilmore, J. H., & Lin, W. (2009). Evidence on the emergence of the brain's default network from 2-week-old to 2-year-old

healthy pediatric subjects. *Proc Natl Acad Sci U S A, 106*(16), 6790-6795. doi:10.1073/pnas.0811221106

Gao, Z., Liu, X., Zhang, D., Liu, M., & Hao, N. (2020). The indispensable role of the cerebellum in visual divergent thinking. *Sci Rep, 10*(1), 16552. doi:10.1038/s41598-020-73679-9

Gardini, S., Venneri, A., Sambataro, F., Cuetos, F., Fasano, F., Marchi, M., . . . Caffarra, P. (2015). Increased functional connectivity in the default mode network in mild cognitive impairment: a maladaptive compensatory mechanism associated with poor semantic memory performance. *J Alzheimers Dis, 45*(2), 457-470. doi:10.3233/JAD-142547

Giove, F., Gili, T., Iacovella, V., Macaluso, E., & Maraviglia, B. (2009). Images-based suppression of unwanted global signals in resting-state functional connectivity studies. *Magn Reson Imaging, 27*(8), 1058-1064. doi:10.1016/j.mri.2009.06.004

Glasser, M. F., Sotiropoulos, S. N., Wilson, J. A., Coalson, T. S., Fischl, B., Andersson, J. L., . . . Consortium, W. U.-M. H. (2013). The minimal preprocessing pipelines for the Human Connectome Project. *Neuroimage, 80*, 105-124. doi:10.1016/j.neuroimage.2013.04.127

Gonzalez-Castillo, J., Roopchansingh, V., Bandettini, P. A., & Bodurka, J. (2011). Physiological noise effects on the flip angle selection in BOLD fMRI. *Neuroimage, 54*(4), 2764-2778. doi:10.1016/j.neuroimage.2010.11.020

Graham, M. S., Drobnjak, I., Jenkinson, M., & Zhang, H. (2017). Quantitative assessment of the susceptibility artefact and its interaction with motion in diffusion MRI. *PLoS One, 12*(10), e0185647. doi:10.1371/journal.pone.0185647

Grayson, D. S., & Fair, D. A. (2017). Development of large-scale functional networks from birth to adulthood: A guide to the neuroimaging literature. *Neuroimage, 160*, 15-31. doi:10.1016/j.neuroimage.2017.01.079

Griffanti, L., Douaud, G., Bijsterbosch, J., Evangelisti, S., Alfaro-Almagro, F., Glasser, M. F., . . . Smith, S. M. (2017). Hand classification of fMRI ICA noise components. *Neuroimage, 154*, 188-205. doi:10.1016/j.neuroimage.2016.12.036

Griswold, M. A., Jakob, P. M., Chen, Q., Goldfarb, J. W., Manning, W. J., Edelman, R. R., & Sodickson, D. K. (1999). Resolution enhancement in single-shot imaging using simultaneous acquisition of spatial harmonics (SMASH). *Magn Reson Med, 41*(6), 1236-1245. doi:10.1002/(sici)1522-2594(199906)41:6<1236::aid-mrm21>3.0.co;2-t

Hausman, H. K., O'Shea, A., Kraft, J. N., Boutzoukas, E. M., Evangelista, N. D., Van Etten, E. J., . . . Woods, A. J. (2020). The Role of Resting-State Network Functional Connectivity in Cognitive Aging. *Front Aging Neurosci, 12*, 177. doi:10.3389/fnagi.2020.00177

He, Y., Wang, J., Wang, L., Chen, Z. J., Yan, C., Yang, H., . . . Evans, A. C. (2009). Uncovering intrinsic modular organization of spontaneous brain activity in humans. *PLoS One, 4*(4), e5226. doi:10.1371/journal.pone.0005226

Heine, L., Soddu, A., Gomez, F., Vanhaudenhuyse, A., Tshibanda, L., Thonnard, M., . . . Demertzi, A. (2012). Resting state networks and consciousness: alterations of multiple resting state network connectivity in physiological, pharmacological, and pathological consciousness States. *Front Psychol, 3*, 295. doi:10.3389/fpsyg.2012.00295

Hojjati, S. H., Ebrahimzadeh, A., & Babajani-Feremi, A. (2019). Identification of the Early Stage of Alzheimer's Disease Using Structural MRI and Resting-State fMRI. *Front Neurol, 10*, 904. doi:10.3389/fneur.2019.00904

Holland, D., Kuperman, J. M., & Dale, A. M. (2010). Efficient correction of inhomogeneous static magnetic field-induced distortion in Echo Planar Imaging. *Neuroimage, 50*(1), 175-183. doi:10.1016/j.neuroimage.2009.11.044

Hollingshead, A. B. (1975). *Four factor index of social status*. New Haven, Conn.: Yale University, Dept. of Sociology.

Holst, L. M., Kronborg, J. B., Jepsen, J. R. M., Christensen, J. O., Vejlstrup, N. G., Juul, K., . . . Ravn, H. B. (2020). Attention-deficit/hyperactivity disorder symptoms in children with surgically corrected Ventricular Septal Defect, Transposition of the Great Arteries, and Tetralogy of Fallot. *Cardiol Young, 30*(2), 180-187. doi:10.1017/S1047951119003184

Homae, F., Watanabe, H., Otobe, T., Nakano, T., Go, T., Konishi, Y., & Taga, G. (2010). Development of global cortical networks in early infancy. *J Neurosci, 30*(14), 4877-4882. doi:10.1523/JNEUROSCI.5618-09.2010

Howell, B. R., Styner, M. A., Gao, W., Yap, P. T., Wang, L., Baluyot, K., . . . Elison, J. T. (2019). The UNC/UMN Baby Connectome Project (BCP): An overview of the study design and protocol development. *Neuroimage, 185*, 891-905. doi:10.1016/j.neuroimage.2018.03.049

Imai, M., Watanabe, H., Yasui, K., Kimura, Y., Shitara, Y., Tsuchida, S., . . . Taga, G. (2014). Functional connectivity of the cortex of term and preterm infants and infants with Down's syndrome. *Neuroimage, 85 Pt 1*, 272-278. doi:10.1016/j.neuroimage.2013.04.080

Irvine, B., Luo, W., & Leon, J. A. (2015). Congenital anomalies in Canada 2013: a perinatal health surveillance report by the Public Health Agency of Canada's Canadian Perinatal Surveillance System. *Health Promot Chronic Dis Prev Can, 35*(1), 21-22. doi:10.24095/hpcdp.35.1.04

Jamadar, S. D., Ward, P. G. D., Close, T. G., Fornito, A., Premaratne, M., O'Brien, K., . . . Egan, G. F. (2020). Simultaneous BOLD-fMRI and constant infusion FDG-PET data of the resting human brain. *Sci Data, 7*(1), 363. doi:10.1038/s41597-020-00699-5

Jenkinson, M., Bannister, P., Brady, M., & Smith, S. (2002). Improved optimization for the robust and accurate linear registration and motion correction of brain images. *Neuroimage, 17*(2), 825-841. doi:10.1016/s1053-8119(02)91132-8

Jenkinson, M., Beckmann, C. F., Behrens, T. E., Woolrich, M. W., & Smith, S. M. (2012). Fsl. *Neuroimage, 62*(2), 782-790. doi:10.1016/j.neuroimage.2011.09.015

Jezzard, P., & Balaban, R. S. (1995). Correction for geometric distortion in echo planar images from B0 field variations. *Magn Reson Med, 34*(1), 65-73. doi:10.1002/mrm.1910340111

Jo, H. J., Gotts, S. J., Reynolds, R. C., Bandettini, P. A., Martin, A., Cox, R. W., & Saad, Z. S. (2013). Effective Preprocessing Procedures Virtually Eliminate Distance-Dependent Motion Artifacts in Resting State FMRI. *J Appl Math, 2013*. doi:10.1155/2013/935154

Jones, D. K., Knosche, T. R., & Turner, R. (2013). White matter integrity, fiber count, and other fallacies: the do's and don'ts of diffusion MRI. *Neuroimage, 73*, 239-254. doi:10.1016/j.neuroimage.2012.06.081

Jones, T. B., Bandettini, P. A., Kenworthy, L., Case, L. K., Milleville, S. C., Martin, A., & Birn, R. M. (2010). Sources of group differences in functional connectivity: an investigation applied to autism spectrum disorder. *Neuroimage, 49*(1), 401-414. doi:10.1016/j.neuroimage.2009.07.051

Keir, M., Ebert, P., Kovacs, A. H., Smith, J. M. C., Kwan, E., Field, T. S., . . . Marelli, A. (2019). Neurocognition in Adult Congenital Heart Disease: How to Monitor and Prevent Progressive Decline. *Canadian Journal of Cardiology, 35*(12), 1675-1685. doi:10.1016/j.cjca.2019.06.020

Kelly, C. J., Makropoulos, A., Cordero-Grande, L., Hutter, J., Price, A., Hughes, E., . . . Counsell, S. J. (2017). Impaired development of the cerebral cortex in infants with congenital heart disease is correlated to reduced cerebral oxygen delivery. *Sci Rep, 7*(1), 15088. doi:10.1038/s41598-017-14939-z

Keunen, K., Counsell, S. J., & Benders, M. (2017). The emergence of functional architecture during early brain development. *Neuroimage, 160*, 2-14. doi:10.1016/j.neuroimage.2017.01.047

Kumar, A., & Chugani, H. T. (2013). Functional imaging: PET. *Handb Clin Neurol, 111*, 767-776. doi:10.1016/B978-0-444-52891-9.00079-8

Kumar, V. A., Heiba, I. M., Prabhu, S. S., Chen, M. M., Colen, R. R., Young, A. L., . . . Liu, H. L. (2020). The role of resting-state functional MRI for clinical preoperative language mapping. *Cancer Imaging, 20*(1), 47. doi:10.1186/s40644-020-00327-w

Kundu, P., Voon, V., Balchandani, P., Lombardo, M. V., Poser, B. A., & Bandettini, P. A. (2017). Multi-echo fMRI: A review of applications in fMRI denoising and analysis of BOLD signals. *Neuroimage, 154*, 59-80. doi:10.1016/j.neuroimage.2017.03.033

Ladd, M. E., Bachert, P., Meyerspeer, M., Moser, E., Nagel, A. M., Norris, D. G., . . . Zaiss, M. (2018). Pros and cons of ultra-high-field MRI/MRS for human application. *Prog Nucl Magn Reson Spectrosc, 109*, 1-50. doi:10.1016/j.pnmrs.2018.06.001

Laird, A. R., Fox, P. M., Eickhoff, S. B., Turner, J. A., Ray, K. L., McKay, D. R., . . . Fox, P. T. (2011). Behavioral interpretations of intrinsic connectivity networks. *J Cogn Neurosci, 23*(12), 4022-4037. doi:10.1162/jocn_a_00077

Latal, B., Patel, P., Liamlahi, R., Knirsch, W., O'Gorman Tuura, R., & von Rhein, M. (2016). Hippocampal volume reduction is associated with intellectual functions in adolescents with congenital heart disease. *Pediatr Res, 80*(4), 531-537. doi:10.1038/pr.2016.122

LeDoux, J. (2007). The amygdala. *Curr Biol, 17*(20), R868-874. doi:10.1016/j.cub.2007.08.005

Lee, M. H., Smyser, C. D., & Shimony, J. S. (2013). Resting-state fMRI: a review of methods and clinical applications. *AJNR Am J Neuroradiol, 34*(10), 1866-1872. doi:10.3174/ajnr.A3263

Li, S., Jamadar, S. D., Ward, P. G. D., Premaratne, M., Egan, G. F., & Chen, Z. (2020). Analysis of continuous infusion functional PET (fPET) in the human brain. *Neuroimage, 213*, 116720. doi:10.1016/j.neuroimage.2020.116720

Limperopoulos, C., Bassan, H., Sullivan, N. R., Soul, J. S., Robertson, R. L., Jr., Moore, M., . . . du Plessis, A. J. (2008). Positive screening for autism in ex-preterm infants: prevalence and risk factors. *Pediatrics, 121*(4), 758-765. doi:10.1542/peds.2007-2158

Lindquist, M. A., & Wager, T. D. (2008). Spatial smoothing in fMRI using prolate spheroidal wave functions. *Hum Brain Mapp, 29*(11), 1276-1287. doi:10.1002/hbm.20475

Liu, W., Hu, X., An, D., Zhou, D., & Gong, Q. (2019). Resting-state functional connectivity alterations in periventricular nodular heterotopia related epilepsy. *Sci Rep, 9*(1), 18473. doi:10.1038/s41598-019-55002-3

Liu, Z., Zhang, M., Xu, G., Huo, C., Tan, Q., Li, Z., & Yuan, Q. (2017). Effective Connectivity Analysis of the Brain Network in Drivers during Actual Driving Using Near-Infrared Spectroscopy. *Front Behav Neurosci, 11*, 211. doi:10.3389/fnbeh.2017.00211

Lund, T. E., Madsen, K. H., Sidaros, K., Luo, W. L., & Nichols, T. E. (2006). Non-white noise in fMRI: does modelling have an impact? *Neuroimage, 29*(1), 54-66. doi:10.1016/j.neuroimage.2005.07.005

Lv, H., Wang, Z., Tong, E., Williams, L. M., Zaharchuk, G., Zeineh, M., . . . Wintermark, M. (2018). Resting-State Functional MRI: Everything That Nonexperts Have Always Wanted to Know. *AJNR Am J Neuroradiol, 39*(8), 1390-1399. doi:10.3174/ajnr.A5527

Maknojia, S., Churchill, N. W., Schweizer, T. A., & Graham, S. J. (2019). Resting State fMRI: Going Through the Motions. *Front Neurosci, 13*, 825. doi:10.3389/fnins.2019.00825

Marelli, A., Miller, S. P., Marino, B. S., Jefferson, A. L., & Newburger, J. W. (2016). Brain in Congenital Heart Disease Across the Lifespan: The Cumulative Burden of Injury. *Circulation, 133*(20), 1951-1962. doi:10.1161/CIRCULATIONAHA.115.019881

McArdle, C. B., Richardson, C. J., Nicholas, D. A., Mirfakhraee, M., Hayden, C. K., & Amparo, E. G. (1987). Developmental features of the neonatal brain: MR imaging. Part I. Gray-white matter differentiation and myelination. *Radiology, 162*(1 Pt 1), 223-229. doi:10.1148/radiology.162.1.3786767

McKeown, M. J., Makeig, S., Brown, G. G., Jung, T. P., Kindermann, S. S., Bell, A. J., & Sejnowski, T. J. (1998). Analysis of fMRI data by blind separation into independent spatial components. *Hum Brain Mapp, 6*(3), 160-188. Retrieved from https://www.ncbi.nlm.nih.gov/pubmed/9673671

Meunier, D., Achard, S., Morcom, A., & Bullmore, E. (2009). Age-related changes in modular organization of human brain functional networks. *Neuroimage, 44*(3), 715-723. doi:10.1016/j.neuroimage.2008.09.062

Mohammadi-Nejad, A. R., Mahmoudzadeh, M., Hassanpour, M. S., Wallois, F., Muzik, O., Papadelis, C., . . . Nasiriavanaki, M. (2018). Neonatal brain resting-state functional connectivity imaging modalities. *Photoacoustics, 10*, 1-19. doi:10.1016/j.pacs.2018.01.003

Motoyama, Y., Oshiro, Y., Takao, Y., Sato, H., Obata, N., Izuta, S., . . . Kan, S. (2019). Resting-state brain functional connectivity in patients with chronic pain who responded to subanesthetic-dose ketamine. *Sci Rep, 9*(1), 12912. doi:10.1038/s41598-019-49360-1

Murphy, K., Birn, R. M., Handwerker, D. A., Jones, T. B., & Bandettini, P. A. (2009). The impact of global signal regression on resting state correlations: are anti-correlated networks introduced? *Neuroimage, 44*(3), 893-905. doi:10.1016/j.neuroimage.2008.09.036

Muschelli, J., Nebel, M. B., Caffo, B. S., Barber, A. D., Pekar, J. J., & Mostofsky, S. H. (2014). Reduction of motion-related artifacts in resting state fMRI using aCompCor. *Neuroimage, 96*, 22-35. doi:10.1016/j.neuroimage.2014.03.028

Newburger, J. W., & Bellinger, D. C. (2006). Brain injury in congenital heart disease. In (Vol. 113, pp. 183-185): Am Heart Assoc.

Newton, H. B. (2016). *Handbook of neuro-oncology neuroimaging*: Academic Press.

Nguyen, A. L. A., Ding, Y., Suffren, S., Londono, I., Luck, D., & Lodygensky, G. A. (2019). The brain's kryptonite: Overview of punctate white matter lesions in neonates. *Int J Dev Neurosci, 77*, 77-88. doi:10.1016/j.ijdevneu.2019.04.006

Noble, S., Scheinost, D., & Constable, R. T. (2019). A decade of test-retest reliability of functional connectivity: A systematic review and meta-analysis. *Neuroimage, 203*, 116157. doi:10.1016/j.neuroimage.2019.116157

Ogawa, S., Lee, T. M., Kay, A. R., & Tank, D. W. (1990). Brain magnetic resonance imaging with contrast dependent on blood oxygenation. *Proc Natl Acad Sci U S A, 87*(24), 9868-9872. doi:10.1073/pnas.87.24.9868

Ogawa, S., Menon, R. S., Tank, D. W., Kim, S. G., Merkle, H., Ellermann, J. M., & Ugurbil, K. (1993). Functional brain mapping by blood oxygenation level-dependent contrast magnetic resonance imaging. A comparison of signal characteristics with a biophysical model. *Biophys J, 64*(3), 803-812. doi:10.1016/S0006-3495(93)81441-3

Parker, D. B., & Razlighi, Q. R. (2019). The Benefit of Slice Timing Correction in Common fMRI Preprocessing Pipelines. *Front Neurosci, 13*, 821. doi:10.3389/fnins.2019.00821

Peng, C., & Hou, X. (2021). Applications of functional near-infrared spectroscopy (fNIRS) in neonates. *Neurosci Res, 170*, 18-23. doi:10.1016/j.neures.2020.11.003

Pierick, A. R., Lynn, M., McCracken, C. M., Oster, M. E., & Iannucci, G. J. (2021). Treatment of attention deficit/hyperactivity disorder in children with CHD. *Cardiol Young*, 1-4. doi:10.1017/S1047951120004965

Pike, N. A., Roy, B., Gupta, R., Singh, S., Woo, M. A., Halnon, N. J., . . . Kumar, R. (2018). Brain abnormalities in cognition, anxiety, and depression regulatory regions in adolescents with single ventricle heart disease. *J Neurosci Res, 96*(6), 1104-1118. doi:10.1002/jnr.24215

Power, J. D., Barnes, K. A., Snyder, A. Z., Schlaggar, B. L., & Petersen, S. E. (2012). Spurious but systematic correlations in functional connectivity MRI networks arise from subject motion. *Neuroimage, 59*(3), 2142-2154. doi:10.1016/j.neuroimage.2011.10.018

Power, J. D., Fair, D. A., Schlaggar, B. L., & Petersen, S. E. (2010). The development of human functional brain networks. *Neuron, 67*(5), 735-748. doi:10.1016/j.neuron.2010.08.017

Power, J. D., Mitra, A., Laumann, T. O., Snyder, A. Z., Schlaggar, B. L., & Petersen, S. E. (2014). Methods to detect, characterize, and remove motion artifact in resting state fMRI. *Neuroimage, 84*, 320-341. doi:10.1016/j.neuroimage.2013.08.048

Power, J. D., Plitt, M., Gotts, S. J., Kundu, P., Voon, V., Bandettini, P. A., & Martin, A. (2018). Ridding fMRI data of motion-related influences: Removal of signals with distinct spatial and physical bases in multiecho data. *Proc Natl Acad Sci U S A, 115*(9), E2105-E2114. doi:10.1073/pnas.1720985115

Rajasilta, O., Tuulari, J. J., Bjornsdotter, M., Scheinin, N. M., Lehtola, S. J., Saunavaara, J., . . . Karlsson, H. (2020). Resting-state networks of the neonate brain identified using independent component analysis. *Dev Neurobiol, 80*(3-4), 111-125. doi:10.1002/dneu.22742

Rangaprakash, D., Tadayonnejad, R., Deshpande, G., O'Neill, J., & Feusner, J. D. (2021). FMRI hemodynamic response function (HRF) as a novel marker of brain function: applications for understanding obsessive-compulsive disorder pathology and treatment response. *Brain Imaging Behav, 15*(3), 1622-1640. doi:10.1007/s11682-020-00358-8

Reid, G. J., Webb, G. D., Barzel, M., McCrindle, B. W., Irvine, M. J., & Siu, S. C. (2006). Estimates of life expectancy by adolescents and young adults with congenital heart disease. *J Am Coll Cardiol, 48*(2), 349-355. doi:10.1016/j.jacc.2006.03.041

Risk, B. B., Murden, R. J., Wu, J., Nebel, M. B., Venkataraman, A., Zhang, Z., & Qiu, D. (2021). Which multiband factor should you choose for your resting-state fMRI study? *Neuroimage, 234*, 117965. doi:10.1016/j.neuroimage.2021.117965

Rivkin, M. J., Watson, C. G., Scoppettuolo, L. A., Wypij, D., Vajapeyam, S., Bellinger, D. C., . . . Newburger, J. W. (2013). Adolescents with D-transposition of the great arteries repaired in early infancy demonstrate reduced white matter microstructure associated with clinical risk factors. *J Thorac Cardiovasc Surg, 146*(3), 543-549 e541. doi:10.1016/j.jtcvs.2012.12.006

Roberts, K. L., & Hall, D. A. (2008). Examining a supramodal network for conflict processing: a systematic review and novel functional magnetic resonance imaging data for related visual and auditory stroop tasks. *J Cogn Neurosci, 20*(6), 1063-1078. doi:10.1162/jocn.2008.20074

Roberts, T. P., Paulson, D. N., Hirschkoff, E., Pratt, K., Mascarenas, A., Miller, P., . . . Edgar, J. C. (2014). Artemis 123: development of a whole-head infant and young child MEG system. *Front Hum Neurosci, 8*, 99. doi:10.3389/fnhum.2014.00099

Robson, P. M., Grant, A. K., Madhuranthakam, A. J., Lattanzi, R., Sodickson, D. K., & McKenzie, C. A. (2008). Comprehensive quantification of signal-to-noise ratio and g-factor for image-based and k-space-based parallel imaging reconstructions. *Magn Reson Med, 60*(4), 895-907. doi:10.1002/mrm.21728

Rogers, C. E., Sylvester, C. M., Mintz, C., Kenley, J. K., Shimony, J. S., Barch, D. M., & Smyser, C. D. (2017). Neonatal Amygdala Functional Connectivity at Rest in Healthy and Preterm Infants and Early Internalizing Symptoms. *J Am Acad Child Adolesc Psychiatry, 56*(2), 157-166. doi:10.1016/j.jaac.2016.11.005

Rohr, C. S., Vinette, S. A., Parsons, K. A. L., Cho, I. Y. K., Dimond, D., Benischek, A., . . . Bray, S. (2017). Functional Connectivity of the Dorsal Attention Network Predicts Selective Attention in 4-7 year-old Girls. *Cereb Cortex, 27*(9), 4350-4360. doi:10.1093/cercor/bhw236

Ross, R. S., LoPresti, M. L., Schon, K., & Stern, C. E. (2013). Role of the hippocampus and orbitofrontal cortex during the disambiguation of social cues in working memory. *Cogn Affect Behav Neurosci, 13*(4), 900-915. doi:10.3758/s13415-013-0170-x

Rouel, M., Raman, J., Hay, P., & Smith, E. (2016). Validation of the Behaviour Rating Inventory of Executive Function - Adult Version (BRIEF-A) in the obese with and without binge eating disorder. *Eat Behav, 23*, 58-65. doi:10.1016/j.eatbeh.2016.07.010

Rubinov, M., & Sporns, O. (2010). Complex network measures of brain connectivity: uses and interpretations. *Neuroimage, 52*(3), 1059-1069. doi:10.1016/j.neuroimage.2009.10.003

Ryan, M., Lacaze-Masmonteil, T., & Mohammad, K. (2019). Neuroprotection from acute brain injury in preterm infants. *Paediatr Child Health, 24*(4), 276-290. doi:10.1093/pch/pxz056

Salimi-Khorshidi, G., Douaud, G., Beckmann, C. F., Glasser, M. F., Griffanti, L., & Smith, S. M. (2014). Automatic denoising of functional MRI data: combining independent component analysis and hierarchical fusion of classifiers. *Neuroimage, 90*, 449-468. doi:10.1016/j.neuroimage.2013.11.046

Savio, A., Funger, S., Tahmasian, M., Rachakonda, S., Manoliu, A., Sorg, C., . . . Yakushev, I. (2017). Resting-State Networks as Simultaneously Measured with Functional MRI and PET. *J Nucl Med, 58*(8), 1314-1317. doi:10.2967/jnumed.116.185835

Schaart, D. R. (2021). Physics and technology of time-of-flight PET detectors. *Phys Med Biol, 66*(9). doi:10.1088/1361-6560/abee56

Seitzman, B. A., Snyder, A. Z., Leuthardt, E. C., & Shimony, J. S. (2019). The State of Resting State Networks. *Top Magn Reson Imaging, 28*(4), 189-196. doi:10.1097/RMR.0000000000000214

Sheline, Y. I., Barch, D. M., Price, J. L., Rundle, M. M., Vaishnavi, S. N., Snyder, A. Z., . . . Raichle, M. E. (2009). The default mode network and self-referential processes in depression. *Proc Natl Acad Sci U S A, 106*(6), 1942-1947. doi:10.1073/pnas.0812686106

Silver, N. C., & Dunlap, W. P. (1987). Averaging correlation coefficients: should Fisher's z transformation be used? *Journal of applied psychology, 72*(1), 146.

Singh, S. P. (2014). Magnetoencephalography: Basic principles. *Ann Indian Acad Neurol, 17*(Suppl 1), S107-112. doi:10.4103/0972-2327.128676

Skoczek, A., Prochownik, P., Gancarczyk, U., Libiszewska, N., Podolec, P., & Komar, M. (2019). Personality traits of patients suffering from congenital heart defects. *Wiad Lek, 72*(11 cz 1), 2135-2144. Retrieved from https://www.ncbi.nlm.nih.gov/pubmed/31860861

Smirnov, A. S., Melnikova-Pitskhelauri, T. V., Sharaev, M. G., Zhukov, V. Y., Pogosbekyan, E. L., Afandiev, R. M., . . . Pronin, I. N. (2020). [Resting-state fMRI in preoperative non-invasive mapping in patients with left hemisphere glioma]. *Zh Vopr Neirokhir Im N N Burdenko, 84*(4), 17-25. doi:10.17116/neiro20208404117

Smith, S. M., Fox, P. T., Miller, K. L., Glahn, D. C., Fox, P. M., Mackay, C. E., . . . Beckmann, C. F. (2009). Correspondence of the brain's functional architecture during activation and rest. *Proc Natl Acad Sci U S A, 106*(31), 13040-13045. doi:10.1073/pnas.0905267106

Smith, S. M., Jenkinson, M., Woolrich, M. W., Beckmann, C. F., Behrens, T. E., Johansen-Berg, H., . . . Matthews, P. M. (2004). Advances in functional and structural MR image analysis and implementation as FSL. *Neuroimage, 23 Suppl 1*, S208-219. doi:10.1016/j.neuroimage.2004.07.051

Smitha, K. A., Akhil Raja, K., Arun, K. M., Rajesh, P. G., Thomas, B., Kapilamoorthy, T. R., & Kesavadas, C. (2017). Resting state fMRI: A review on methods in resting state connectivity analysis and resting state networks. *Neuroradiol J, 30*(4), 305-317. doi:10.1177/1971400917697342

Smitha, K. A., Arun, K. M., Rajesh, P. G., Joel, S. E., Venkatesan, R., Thomas, B., & Kesavadas, C. (2018). Multiband fMRI as a plausible, time-saving technique for resting-state data acquisition: Study on functional connectivity mapping using graph theoretical measures. *Magn Reson Imaging, 53*, 1-6. doi:10.1016/j.mri.2018.06.013

Smyser, C. D., Inder, T. E., Shimony, J. S., Hill, J. E., Degnan, A. J., Snyder, A. Z., & Neil, J. J. (2010). Longitudinal analysis of neural network development in preterm infants. *Cereb Cortex, 20*(12), 2852-2862. doi:10.1093/cercor/bhq035

Smyser, C. D., & Neil, J. J. (2015). Use of resting-state functional MRI to study brain development and injury in neonates. *Semin Perinatol, 39*(2), 130-140. doi:10.1053/j.semperi.2015.01.006

Smyser, C. D., Snyder, A. Z., Shimony, J. S., Blazey, T. M., Inder, T. E., & Neil, J. J. (2013). Effects of white matter injury on resting state fMRI measures in prematurely born infants. *PLoS One, 8*(7), e68098. doi:10.1371/journal.pone.0068098

Smyser, C. D., Snyder, A. Z., Shimony, J. S., Mitra, A., Inder, T. E., & Neil, J. J. (2016). Resting-State Network Complexity and Magnitude Are Reduced in Prematurely Born Infants. *Cereb Cortex, 26*(1), 322-333. doi:10.1093/cercor/bhu251

Smyser, C. D., Wheelock, M. D., Limbrick, D. D., Jr., & Neil, J. J. (2019). Neonatal brain injury and aberrant connectivity. *Neuroimage, 185*, 609-623. doi:10.1016/j.neuroimage.2018.07.057

Stephan, K. E., & Friston, K. J. (2010). Analyzing effective connectivity with functional magnetic resonance imaging. *Wiley Interdiscip Rev Cogn Sci, 1*(3), 446-459. doi:10.1002/wcs.58

Sylvester, C. M., Smyser, C. D., Smyser, T., Kenley, J., Ackerman, J. J., Jr., Shimony, J. S., . . . Rogers, C. E. (2018). Cortical Functional Connectivity Evident After Birth and Behavioral Inhibition at Age 2. *Am J Psychiatry, 175*(2), 180-187. doi:10.1176/appi.ajp.2017.17010018

Talairach, J. (1988). Co-planar stereotaxic atlas of the human brain-3-dimensional proportional system. *An approach to cerebral imaging*.

Tamilia, E., Madsen, J. R., Grant, P. E., Pearl, P. L., & Papadelis, C. (2017). Current and Emerging Potential of Magnetoencephalography in the Detection and Localization of High-Frequency Oscillations in Epilepsy. *Front Neurol, 8*, 14. doi:10.3389/fneur.2017.00014

Tang, S., Lu, L., Zhang, L., Hu, X., Bu, X., Li, H., . . . Huang, X. (2018). Abnormal amygdala resting-state functional connectivity in adults and adolescents with major depressive disorder: A comparative meta-analysis. *EBioMedicine, 36*, 436-445. doi:10.1016/j.ebiom.2018.09.010

Thorngren-Jerneck, K., Ohlsson, T., Sandell, A., Erlandsson, K., Strand, S. E., Ryding, E., & Svenningsen, N. W. (2001). Cerebral glucose metabolism measured by positron emission

tomography in term newborn infants with hypoxic ischemic encephalopathy. *Pediatr Res, 49*(4), 495-501. doi:10.1203/00006450-200104000-00010

Tierney, A. L., Gabard-Durnam, L., Vogel-Farley, V., Tager-Flusberg, H., & Nelson, C. A. (2012). Developmental trajectories of resting EEG power: an endophenotype of autism spectrum disorder. *PLoS One, 7*(6), e39127. doi:10.1371/journal.pone.0039127

Tomiyama, H., Nakao, T., Murayama, K., Nemoto, K., Ikari, K., Yamada, S., . . . Kanba, S. (2019). Dysfunction between dorsal caudate and salience network associated with impaired cognitive flexibility in obsessive-compulsive disorder: A resting-state fMRI study. *Neuroimage Clin, 24*, 102004. doi:10.1016/j.nicl.2019.102004

Toussaint, P. J., Perlbarg, V., Bellec, P., Desarnaud, S., Lacomblez, L., Doyon, J., . . . Benali, f. t. A. s. D. N. I. (2012). Resting state FDG-PET functional connectivity as an early biomarker of Alzheimer's disease using conjoint univariate and independent component analyses. *Neuroimage, 63*(2), 936-946. doi:10.1016/j.neuroimage.2012.03.091

Tyagi, M., Fteropoulli, T., Hurt, C. S., Hirani, S. P., Rixon, L., Davies, A., . . . Newman, S. P. (2017). Cognitive dysfunction in adult CHD with different structural complexity. *Cardiol Young, 27*(5), 851-859. doi:10.1017/S1047951116001396

van den Heuvel, M. I., & Thomason, M. E. (2016). Functional Connectivity of the Human Brain in Utero. *Trends Cogn Sci, 20*(12), 931-939. doi:10.1016/j.tics.2016.10.001

Van Dijk, K. R., Hedden, T., Venkataraman, A., Evans, K. C., Lazar, S. W., & Buckner, R. L. (2010). Intrinsic functional connectivity as a tool for human connectomics: theory, properties, and optimization. *J Neurophysiol, 103*(1), 297-321. doi:10.1152/jn.00783.2009

Vincent, K., Moore, J., Kennedy, S., & Tracey, I. (2009). Blood oxygenation level dependent functional magnetic resonance imaging: current and potential uses in obstetrics and gynaecology. *BJOG, 116*(2), 240-246. doi:10.1111/j.1471-0528.2008.01993.x

Volpe, J. J. (2009). Brain injury in premature infants: a complex amalgam of destructive and developmental disturbances. *Lancet Neurol, 8*(1), 110-124. doi:10.1016/S1474-4422(08)70294-1

von Rhein, M., Buchmann, A., Hagmann, C., Huber, R., Klaver, P., Knirsch, W., & Latal, B. (2014). Brain volumes predict neurodevelopment in adolescents after surgery for congenital heart disease. *Brain, 137*(Pt 1), 268-276. doi:10.1093/brain/awt322

Vos de Wael, R., Hyder, F., & Thompson, G. J. (2017). Effects of Tissue-Specific Functional Magnetic Resonance Imaging Signal Regression on Resting-State Functional Connectivity. *Brain Connect, 7*(8), 482-490. doi:10.1089/brain.2016.0465

Wang, Y., Lu, W., Xie, Y., Zhou, J., Yan, T., Han, W., & Qiu, J. (2020). Functional Alterations in Resting-State Visual Networks in High-Tension Glaucoma: An Independent Component Analysis. *Front Hum Neurosci, 14*, 330. doi:10.3389/fnhum.2020.00330

Wang, Y., Qin, Y., Li, H., Yao, D., Sun, B., Li, Z., . . . Luo, C. (2019). Abnormal Functional Connectivity in Cognitive Control Network, Default Mode Network, and Visual Attention Network in Internet Addiction: A Resting-State fMRI Study. *Front Neurol, 10*, 1006. doi:10.3389/fneur.2019.01006

Watson, C. G., Asaro, L. A., Wypij, D., Robertson, R. L., Jr., Newburger, J. W., & Rivkin, M. J. (2016). Altered Gray Matter in Adolescents with d-Transposition of the Great Arteries. *J Pediatr, 169*, 36-43 e31. doi:10.1016/j.jpeds.2015.09.084

Watson, C. G., Stopp, C., Wypij, D., Bellinger, D. C., Newburger, J. W., & Rivkin, M. J. (2018). Altered White Matter Microstructure Correlates with IQ and Processing Speed in Children and Adolescents Post-Fontan. *J Pediatr, 200*, 140-149 e144. doi:10.1016/j.jpeds.2018.04.022

Wehrle, F. M., Michels, L., Guggenberger, R., Huber, R., Latal, B., O'Gorman, R. L., & Hagmann, C. F. (2018). Altered resting-state functional connectivity in children and adolescents born very preterm short title. *Neuroimage Clin, 20*, 1148-1156. doi:10.1016/j.nicl.2018.10.002

Westphal, R., Simmons, C., Mesquita, M. B., Wood, T. C., Williams, S. C., Vernon, A. C., & Cash, D. (2017). Characterization of the resting-state brain network topology in the 6-hydroxydopamine rat model of Parkinson's disease. *PLoS One, 12*(3), e0172394. doi:10.1371/journal.pone.0172394

White, B. R., Liao, S. M., Ferradal, S. L., Inder, T. E., & Culver, J. P. (2012). Bedside optical imaging of occipital resting-state functional connectivity in neonates. *Neuroimage, 59*(3), 2529-2538. doi:10.1016/j.neuroimage.2011.08.094

Whitfield-Gabrieli, S., Moran, J. M., Nieto-Castanon, A., Triantafyllou, C., Saxe, R., & Gabrieli, J. D. (2011). Associations and dissociations between default and self-reference networks in the human brain. *Neuroimage, 55*(1), 225-232. doi:10.1016/j.neuroimage.2010.11.048

Whitfield-Gabrieli, S., & Nieto-Castanon, A. (2012). Conn: a functional connectivity toolbox for correlated and anticorrelated brain networks. *Brain Connect, 2*(3), 125-141. doi:10.1089/brain.2012.0073

Woodward, N. D., & Cascio, C. J. (2015). Resting-State Functional Connectivity in Psychiatric Disorders. *JAMA Psychiatry, 72*(8), 743-744. doi:10.1001/jamapsychiatry.2015.0484

Woolrich, M. W., Jbabdi, S., Patenaude, B., Chappell, M., Makni, S., Behrens, T., . . . Smith, S. M. (2009). Bayesian analysis of neuroimaging data in FSL. *Neuroimage, 45*(1 Suppl), S173-186. doi:10.1016/j.neuroimage.2008.10.055

Xu, T., Yang, Z., Jiang, L., Xing, X.-X., & Zuo, X.-N. (2015). A connectome computation system for discovery science of brain. *Science Bulletin, 60*(1), 86-95.

Xue, H., Wang, Z., Tan, Y., Yang, H., Fu, W., Xue, L., & Zhao, J. (2020). Resting-state EEG reveals global network deficiency in dyslexic children. *Neuropsychologia, 138*, 107343. doi:10.1016/j.neuropsychologia.2020.107343

Zhang, D., Johnston, J. M., Fox, M. D., Leuthardt, E. C., Grubb, R. L., Chicoine, M. R., . . . Shimony, J. S. (2009). Preoperative sensorimotor mapping in brain tumor patients using spontaneous fluctuations in neuronal activity imaged with functional magnetic resonance imaging: initial experience. *Neurosurgery, 65*(6 Suppl), 226-236. doi:10.1227/01.NEU.0000350868.95634.CA

Zhang, H., Shen, D., & Lin, W. (2019). Resting-state functional MRI studies on infant brains: A decade of gap-filling efforts. *Neuroimage, 185*, 664-684. doi:10.1016/j.neuroimage.2018.07.004

Zhang, L., Zuo, X. N., Ng, K. K., Chong, J. S. X., Shim, H. Y., Ong, M. Q. W., . . . Zhou, J. H. (2020). Distinct BOLD variability changes in the default mode and salience networks in Alzheimer's disease spectrum and associations with cognitive decline. *Sci Rep, 10*(1), 6457. doi:10.1038/s41598-020-63540-4

Zuo, X. N., Anderson, J. S., Bellec, P., Birn, R. M., Biswal, B. B., Blautzik, J., . . . Milham, M. P. (2014). An open science resource for establishing reliability and reproducibility in functional connectomics. *Sci Data, 1*, 140049. doi:10.1038/sdata.2014.49

Zuo, X. N., Kelly, C., Adelstein, J. S., Klein, D. F., Castellanos, F. X., & Milham, M. P. (2010). Reliable intrinsic connectivity networks: test-retest evaluation using ICA and dual regression approach. *Neuroimage, 49*(3), 2163-2177. doi:10.1016/j.neuroimage.2009.10.080

Zuo, X. N., & Xing, X. X. (2014). Test-retest reliabilities of resting-state FMRI measurements in human brain functional connectomics: a systems neuroscience perspective. *Neurosci Biobehav Rev, 45*, 100-118. doi:10.1016/j.neubiorev.2014.05.009

Zuo, X. N., Xu, T., & Milham, M. P. (2019). Harnessing reliability for neuroscience research. *Nat Hum Behav, 3*(8), 768-771. doi:10.1038/s41562-019-0655-x

APPENDIX A SUPPLEMENTARY MATERIALS ARTICLE 1

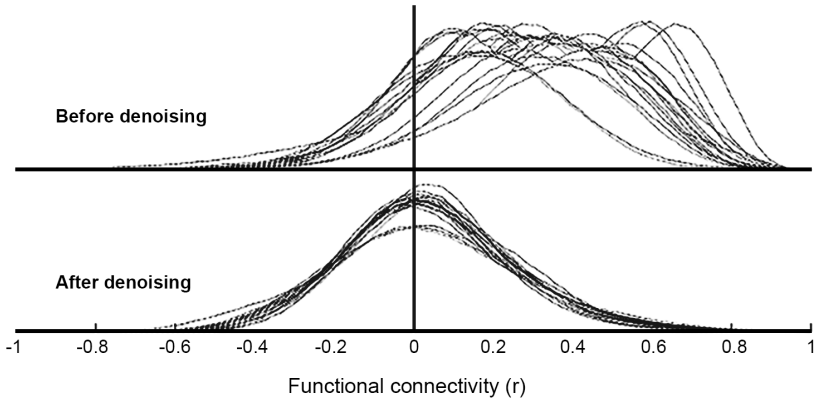

Figure A. 1. Example of connectivity distribution histogram plot.

Table A. 1. Results BRIEF-A > 65.

Number (and percentage) of participants with a score >65 (abnormal) on the BRIEF-A scales for CHD and controls (CTL). Chi-squared test for proportions comparison. ** p< 0.01; ***p<0.001.

N (%)	**CHD (n=35)**	**CTL (n=44)**	**p-value**
Inhibit***	10 (28.6)	0.0 (0.0)	< 0.001
Shift	6 (17.1)	4 (9.1)	0.29
Emotional control	6 (17.1)	4 (9.1)	0.29
Self-monitor	7 (20.0)	3 (6.8)	0.08
Initiate	6 (17.1)	5 (11.4)	0.47
Working memory**	14 (40.0)	6 (13.6)	0.008

Plan/ Organize	2 (5.7)	2 (4.5)	0.81
Task monitor	9 (25.7)	6 (13.6)	0.18
Organization of materials***	10 (28.6)	1 (2.3)	< 0.001

Overall a greater percentage of youths with CHD performed below clinical cutoff (i.e., >65) than control (5.7 – 40.0% in CHD vs. 0 – 13.6% in controls) reaching statistical difference for the inhibit (X^2=14.23; p< 0.001), working memory (X^2=7.1; p=0.008) and organization of material (X^2=11.09; p< 0.001) scales (Table 3).